Title
Quantum Simulation with Superconducting Circuits

Author
Ramasesh, Vinay Venkatesh

Publication Date
2019

Peer reviewed|Thesis/dissertation

Quantum Simulation with Superconducting Circuits

by

Vinay Ramasesh

A dissertation submitted in partial satisfaction of the

requirements for the degree of

Doctor of Philosophy

in

Physics

in the

Graduate Division

of the

University of California, Berkeley

Committee in charge:

Professor Irfan Siddiqi, Chair
Professor Birgitta Whaley
Professor Norman Yao

Summer 2019

Quantum Simulation with Superconducting Circuits

Abstract

Quantum Simulation with Superconducting Circuits

by

Vinay Ramasesh

Doctor of Philosophy in Physics

University of California, Berkeley

Professor Irfan Siddiqi, Chair

Nonlinear superconducting circuits are a leading candidate to implement quantum information tasks beyond the reach of classical processors. One such task, quantum simulation, involves using a controllable quantum system to study the dynamics of another. In this thesis, we present a series of experiments using small systems of superconducting circuits to perform various quantum tasks relevant to quantum simulation.

In the first experiment, we design and build a circuit comprising three transmon qubits whose dynamics mirror those of interacting bosonic particles on a lattice, described by the Bose-Hubbard Hamiltonian. We verify the predictions of the Bose-Hubbard model for this system spectroscopically and then use time-domain measurements to study the decoherence processes affecting the qubits. Using a Raman process, we engineer artificial decay dynamics in the system which allow us to prepare and stabilize otherwise inaccessible states of the transmon array.

The second experimental demonstration concerns topological quantum matter. Certain quantum systems are characterized by quantities known as topological invariants, which are robust to local perturbations. These topological invariants are challenging to measure in naturally-occurring systems. We engineer an artificial system, comprising a transmon qubit coupled to a high-Q cavity, capable of undergoing a protocol known as the quantum walk, which also exhibits topological invariants. By using particular non-classical state of the cavity, we modify the quantum walk protocol to make the topological invariant directly accessible.

Finally, we implement a hybrid quantum-classical algorithm—known as the variational quantum eigensolver—in a two-transmon quantum processor. As a proof of principle demonstration, we compute the ground-state and low-lying excited state energies of the hydrogen molecule as a function of nuclear separation. We show that an extension of the basic algorithm, known as the quantum subspace expansion, allows for the mitigation of errors caused by decoherence processes affecting the quantum processor.

To my parents, Nalini and Ranga Ramasesh, and my grandmother, Lakshmi Ramachandran, for their constant support and encouragement.

Contents

List of Figures

List of Tables

Acknowledgments

I am extremely grateful to have spent the last six years at Berkeley working in the Quantum Nanoelectronics Lab. It is a pleasure to thank the many people who contributed to making my time here an enjoyable and productive learning experience.

Thanks first to my advisor, Dr. Irfan Siddiqi, for welcoming me into his lab and maintaining such a great environment for nurturing scientific curiosity. Irfan constantly pushes his students to perform at the best of their ability while giving them the freedom to explore their individual interests, for which I am truly grateful. My ability to think independently as a scientist and generate interesting research directions on my own has come about through his guidance, and I am very fortunate to have had such an inspiring mentor.

One of our closest collaborators during my time here at Berkeley was Dr. Norman Yao, who was a postdoc when I started grad school and is now a professor. Norman was a fantastic collaborator; his knowledge of quantum physics is unparalleled and helped us to get the quantum walk experiment working. I had a great time working with him, and also discussing physics and life over tennis matches, Chengdu dinners, Marvel movie nights, and many many paper draft revisions.

I have also been fortunate to work with five incredibly talented postdocs, who have shaped my skills and thinking a great deal. Dr. Shay Hacohen-Gourgy was a pleasure to work with as a new graduate student in QNL; he taught me the basics of working with dilution fridges, patiently led me through fabricating my first samples, and showed me what it means to be an experimental physicist. Dr. Emmanuel Flurin mentored me through the quantum walk project; his incredibly deep knowledge of circuit QED was a huge asset to that project, and I hope to have picked up some of his knowledge along the way. Dr. Kevin O'Brien showed me the value of carefully attacking a complex problem systematically and scientifically to produce almost magical-seeming results. I enjoyed all of our discussions through many hours of fabrication and testing, and especially appreciated his ability to hone in and focus on the most important parts of any given problem. From Dr. James Colless I learned the importance of precisely and quantitatively understanding as much of the experimental apparatus as possible. I was also constantly impressed by how hard he worked. Dr. Machiel Blok was my partner in the qutrit black hole experiment. I greatly enjoyed working with him, and learned a lot from his style of doing physics, specifically his approach to data analysis and his resilience in the face of inevitable setbacks. I wish we had still another year to pursue all the ideas we discussed over the last couple years.

The entirety of QNL, past and present, deserves many thanks for making the lab a great place to work. These include graduate students, undergrads, visitors, and postdocs. I enjoyed our house of curries lunches, Tahoe trips, foosball matches, Bring Sally Up competition, and last but certainly not least, the invention of Cracketball. I am privileged to have worked with all of you: Eli Levenson-Falk, Chris Macklin, Mollie Schwartz, Andrew Eddins, Steven Weber, David Toyli, Nick Frattini, Aditya Venkatramani, Eunsong Kim, Allison Dove, Leigh Martin, John Mark Kreikebaum, Will Livingston, Brad Mitchell, Marie

Lu, Trevor Christolini, Akel Hashim, Ravi Naik, Archan Banerjee, Dar Dahlen, Jack Qiu, and Noah Stevenson.

I am very thankful for the many friends in the area who made daily life in Berkeley such a joy. Berkeley is a very tough place to leave thanks to all of you.

Finally, I would like to thank my family, without whom none of this would have been possible. Their love, support, and encouragement throughout the entirety of graduate school and long before are the things for which I am most thankful; without them, I would never have had the will to make it this far. I love you very much, and dedicate this thesis to you.

Chapter 1

Introduction

Though quantum theory is nearly a century old, the technology to precisely control and measure complex quantum systems is still in its infancy. Only in the past few decades has it become possible to isolate individual quantum systems for experimental manipulation, and even with the heroic efforts of many theoretical and experimental physicists, current state-of-the-art quantum technology is only capable of performing a modest tens of gates on systems comprising fewer than one hundred quantum bits.

There could be a great payoff if we were to realize more powerful quantum technology. For example, certain problems of technological significance rely on the ability to understand, or at least precisely simulate, strongly-interacting quantum systems. High-temperature superconductors, for instance, could lead to many new technologies, but currently the search for materials that can conduct electricity without dissipation at increasingly high temperatures is hampered by the fact that we do not possess an understanding of how superconductivity in these materials works. As another example, the ability to precisely predict chemical reaction dynamics relies on the knowledge of molecular spectra, which—especially for large molecules—are difficult to calculate using classical hardware. With precisely-controllable quantum devices, it might be possible to simulate such complex quantum systems and gain some insights into their behavior, as a complement to purely theoretical approaches.

In addition to simulation, controllable quantum devices could also be used to carry out computations faster or more cheaply than their classical counterparts. The full power of these quantum computers is still an open theoretical question—including, for example, which problems would be better solved on a quantum computer than a classical one. However, there is reason for cautious optimism here, given the existence of Shor's algorithm, a quantum algorithm capable of factoring large integers exponentially faster than the best-known classical algorithm for doing so. Though it is almost certain that devices capable of executing Shor's algorithm on a large integer would require a massive overhead in qubit number to perform error-correction, there is even some hope that quantum devices without error correction may be able to solve useful problems. These devices have been named NISQ computers by John Preskill, to emphasize that they are **N**oisy, and only of **I**ntermediate **S**cale—the Q, of course, stands for quantum. Molecular energy calculations and high-dimensional optimization are

examples of problems which NISQ devices might solve.

There are currently a number of different experimental systems which are being investigated as possible substrates for quantum hardware. These include atoms or ions trapped by lasers and magnetic fields, defects in diamond lattices (so-called nitrogen-vacancy centers or color centers), optical photons in silicon chips, and quantum dots in semiconductors. Each system has unique advantages and disadvantages—for example, some systems can be operated at room-temperature while others need to be cooled in a cryostat or dilution refrigerator; or, some systems can store information for long periods but are slow to control while others lose information quickly but can also be controlled quickly. Since the field is so primitive, relatively speaking, it is quite uncertain whether one of these technologies will become dominant in the future, or if ultimately hybrid approaches will be necessary.

In this thesis, we report experiments performed on quantum systems built out of superconducting electrical circuits—at the time of writing, one of the leading candidates for realizing a useful quantum device. Compared to the systems mentioned previously, superconducting qubits are macroscopic, on the order of hundreds of microns. The idea of observing quantum behavior in a macroscopic superconducting circuit is due to Leggett, who proposed in the 1980s that these systems might be good tests of the validity of quantum mechanics (and in particular, the superposition principle) at larger length scales than had been accessed previously. Leggett's prediction that a superconducting circuit might be the first to show quantum behavior of a single macroscopic degree of freedom was borne out experimentally in 1986 at UC Berkeley by John Martinis, Michel Devoret, and John Clarke, who showed quantum behavior of the superconducting phase difference across a circuit element known as a Josephson junction, which consists of an insulating barrier separating two superconductors. The first demonstration of a quantum bit based on this macroscopic manifestation of quantum behavior came twelve years later, when researchers at NEC in Japan demonstrated coherent oscillations between two states of a superconducting circuit known as a Cooper pair box—named because the states involved in the oscillation were states of definite Cooper pair number (charge) on a small superconducting island. Remarkably, the experiments in this thesis, conducted nearly twenty years after this initial demonstration, use a circuit design very similar to the Cooper pair box, known as the transmon. However, remarkable engineering innovations in the intervening years have brought the coherence times of these systems up from the nanosecond scale to nearly one hundred microseconds.

The improvement in coherence times of superconducting qubits has allowed for many impressive experimental demonstrations. For example, using fast non-demolition measurement of the qubit state in conjunction with feedback, Rabi oscillations in a qubit were made to persist indefinitely. In another experiment, a decades-old quantum optics prediction—that the decay of atomic coherence could be suppressed by exposing it to squeezed vacuum—was verified with superconducting qubits. And these are only two of many. Yet, despite all this great work, the toolbox of experimental quantum processing is still somewhat limited. We cannot, for example, yet perform entangling operations on pairs of superconducting qubits with nearly the precision required to perform true quantum computation. And given a large quantum system comprising several qubits, we do not have general tools for preparing an

arbitrary system state. The work reported in this thesis adds a few more tools to the toolbox associated with experimental quantum information processing with superconducting circuits.

1.1 Structure of Thesis

The rest of this thesis is structured as follows.

Chapter 2 discusses the theoretical background necessary to understand the experiments reported in the subsequent chapters. At the time of writing, the field of circuit quantum electrodynamics is already mature enough that this material has been presented in several prior theses and even some textbooks. For that reason, the intent of chapter 2 is not to serve as a pedagogical introduction for the student with no familiarity with superconducting quantum circuits, but instead to give just the background necessary to understand this thesis, and also to correct common misconceptions in the field. A graduate student in the field halfway through his or her career will hopefully benefit from reading this chapter.

Chapters 3 through 6 present the original experimental and theoretical work.

In chapter 3, we discuss an experimental demonstration of Bose-Hubbard dyanmics in a system of three coupled transmon qubits. That chapter begins by introducing the Bose-Hubbard Hamiltonian and showing how it can be realized with superconducting circuits. We then describe our three-transmon experimental system, and show the initial spectroscopic measurements to confirm the validity of the Bose-Hubbard description. We then characterize the natural decay dynamics of the system as a prelude to the final result: applying bath engineering to alter the natural decay rates and achieve state stabilization.

Chapters 4 and 5 together present a unified theoretical and experimental study of topological quantum walks in superconducting qubit systems. These chapters build up to the key result, namely the use of a coupled superconducting circuit-cavity system to perform a topological quantum walk and directly measure the associated topological invariant. Chapter 4 primarily discusses the theoretical aspect of the study: we motivate the quantum walk algorithm, describe how its dynamics show topological features, and then discuss our novel protocol for modifying the quantum walk such that the topological invariant gets imprinted as a phase on the state of the system. We end the chapter with a proposal showing how a circuit quantum electrodynamics system can realize this measurement. Chapter 5 picks up the thread, showing how we successfully realized this proposal experimentally. We discuss in detail the experimental protocol, and novel features of our system which enabled the performance of a quantum walk.

In chapter 6, we switch gears from quantum simulation to quantum algorithms: specifically, we describe the execution of an algorithm known as the variational quantum eigensolver, or VQE, on a system comprising two transmon qubits. In this chapter we motivate the variational quantum eigensolver as a potential application of pre-error-corrected quantum processors, and describe our application of it to calculate the energy spectrum of the hydrogen molecule. A novel feature of our execution is the use of additional measurements to correct for incoherent errors and extract excited-state energies; the bulk of the chapter

is thus devoted to discussing how these additional measurements, known as the *quantum subspace expansion*, work.

1.2 Summary of Key Results

The work reported in this thesis builds upon pioneering work over the last few decades which developed superconducting quantum circuits into highly coherent, individually controllable quantum systems. Specifically, the experiments herein focus largely on the transmon circuit, aiming to develop tools which will be useful for controlling and measuring systems comprising multiple interacting quantum devices. There are three main experimental results reported in this thesis: realization of a Bose-Hubbard sysstem with transmons, direct measurement of a topological invariant in a quantum walk, and hybrid quantum-classical calculation of the hydrogen electronic spectrum. If there is a unifying thread among these, it is that they are all aimed towards using transmon circuits to perform quantum simulation, both in the analog and digital flavors.

In the realization of a Bose-Hubbard system with transmons, we show theoretically and experimentally that a chain of nearest-neighbor coupled transmon circuits is described by a Hamiltonian known in condensed-matter physics as the Bose-Hubbard Hamiltonian, a paradigmatic model of interacting quantum matter. Using transmons, we demonstrate for the first time an experimental simulation of Bose-Hubbard decay dynamics in the regime of *attractive* interactions, which had previously not been accessible to experiments. Further, we show that one can use so-called *bath engineering* techniques, which had been developed previously in QNL for a single cavity-coupled transmon, to modify the decay dynamics of this system. This represents the first instance of engineering dissipation for a quantum many-body system. Combining the bath engineering techniques with coherent drives, we finally show how one can stabilize certain states of this many-body system against loss.

The second major result of this thesis—the direct measurement of a topological invariant in a quantum walk—is also an analog quantum simulation, but in this case of a single-particle (non-interacting) *topological* quantum system rather than a many-body system like the Bose-Hubbard. The main novelty of this experiment was to show, for the first time in an experiment, the topological character of the quantum walk algorithm. In addition, this experiment demonstrated the first realization of a quantum walk in superconducting circuits, and showed how techniques from the field of circuit quantum electrodynamics could be used to measure the entire wavefunction of the system undergoing the quantum walk.

The final result reported here is the execution of a quantum algorithm, known as the variational quantum eigensolver, on a quantum processor comprising two transmon qubits. The variational quantum eigensolver, a hybrid quantum-classical algorithm used to calculate ground-state energies of quantums systems, had been demonstrated before in superconducting circuits by the Martinis group [], but in a limited form. Here we perform the full algorithm, and moreover show an extension of this algorithm which allows both for the more accurate calculation of the ground-state energy and also an extraction of low-lying excited

states as well. This extension, known as the quantum subspace expansion, was demonstrated experimentally for the first time in this work.

Chapter 2

Superconducting Circuits: Background

Superconducting electrical circuits form the building blocks for the quantum systems used in the experiments described herein. As of 2019, many different types of superconducting quantum circuits exist; the most common of these, known as the transmon, is used for the experiments in this thesis. The transmon circuit is essentially a quantum electromagnetic oscillator with a weak nonlinearity; it is this nonlinearity which allows the lowest two energy levels of the transmon to be used as an qubit. Typically, the transmon qubit is coupled to a linear resonator to allow for its state to be measured and to entangle it with other transmons; this architecture is known as circuit quantum electrodynamics, or cQED.

In this background chapter, we describe the both the transmon qubit and the circuit QED architecture. As the field of superconducting quantum information is now reasonably mature, there are many good introductions to this material, both in textbooks and other theses. The intent of this chapter is not to serve as yet another pedagogical introduction, but rather to succinctly present enough background for the reader unfamiliar with circuit QED to understand the results presented here. At the end of this chapter, we provide a list of references for those who desire a deeper understanding.

2.1 Quantum behavior in superconducting circuits

While it may seem natural for microscopic systems such as trapped ions, Rydberg atoms, or photons to display quantum behavior, it is perhaps harder to understand how such behavior can emerge in something like a circuit, which is typically macroscopic. Yet, circuits made from superconductors can in fact harbor quantum behavior, supporting superpositions of classically-allowed states and even allowing for entanglement between spatially separated circuits.

One way of understanding how this behavior can be described, at least in circuits like the transmon which classically behave as oscillators, is to consider the simplest oscillating

circuit: the LC circuit, consisting of an inductor and capacitor in parallel. Classically, the state of this circuit is specified by two variables: the charge on the capacitor plates and the magnetic flux threading the inductor. To model the behavior of this circuit, one can solve Kirchhoff's laws for these variables (or the current and voltage), which will show that the state variables describing the system oscillate at an angular frequency $\omega = 1/\sqrt{LC}$. The standard description of how to quantize this circuit is to find a Lagrangian which gives the same dynamics as Kirchhoff's laws, convert that to a Hamiltonian via a Legendre transform, and then promote the variables q and ϕ to canonically conjugate operators. This view can be found in many theses and textbooks. However, a perhaps more intuitive view is to realize that the description of this system as a circuit is just an approximation to the true behavior of the system, which is governed classically by Maxwell's equations. That is, when we say that the circuit is an oscillator, we really mean that there exists a mode of the electromagnetic field whose frequency is approximately $1/\sqrt{LC}$. When we ask how the circuit will behave quantum mechanically, we find that it behaves as any other electromagnetic mode: namely, the eigenstates of the system are Fock states or photon-number states which have energy $\hbar\omega n$, where n is the number of photons in the mode.

If one does a proper analysis using the Lagrangian/Hamiltonian approach, the results bear out this intuition. Specifically, the quantities q (charge across the capacitor) and ϕ (flux across the inductor), turn into operators which do not commute. Their commutation relation is in fact identical to that between $\hat{x}$ and $\hat{p}$ in one-dimensional quantum systems

$$[\hat{Q}, \hat{\Phi}] = i\hbar. \tag{2.1}$$

In terms of these operators, the Hamiltonian of the Harmonic oscillator is given by

$$H = \frac{1}{2C}\hat{Q}^2 + \frac{1}{2L}\hat{\Phi}^2. \tag{2.2}$$

In analogy with the quantization of the simple harmonic oscillator with $\hat{x}$ and $\hat{p}$, we define a ladder operator:

$$\hat{a} = \frac{1}{\sqrt{2\hbar Z}}(\hat{\Phi} + iZ\hat{Q}), \tag{2.3}$$

where Z is defined as the resonator impedance $\sqrt{L/C}$. Then the Hamiltonian transforms into

$$H = \hbar\omega(a^\dagger a + \frac{1}{2}), \tag{2.4}$$

the familiar quantum harmonic oscillator Hamiltonian. As for the classical LC circuit, the angular frequency ω is $1/\sqrt{LC}$.

In a mechanical quantum harmonic oscillator, applying a driving force $F(t)$ to the oscillator can be modeled by adding a term to the Hamiltonian given by $F(t)\hat{x}$, which (absorbing some pre-factors into the term $\epsilon(t)$ can be written

$$H_{\text{drive}} = \epsilon(t)\left(a + a^\dagger\right). \tag{2.5}$$

The same is true for the quantum LC circuit, driven by applying a voltage $V(t)$ through a coupling capacitor, since classically, the work required to move a charge Q through a voltage V is given by QV. By driving the oscillator near its resonance frequency, the oscillator can be populated with photons.

Though the quantization of the LC oscillator was presented simply to introduce the idea of quantum behavior in electrical circuits, and to show how to describe such behavior, it turns out that the qubit used in this thesis—the transmon—is very similar to this LC oscillator. Before discussing that, let us understand why we cannot use the LC oscillator as a qubit. After all, the Hamiltonian in eqn. 2.4 supports discrete states, and it is tempting to think that a couple of these could be used to form qubit states. Unfortunately, the linearity of the oscillator prevents this from being done in a straightforward manner. To see this, consider using the two lowest-lying states (the $|0\rangle$ and $|1\rangle$-photon states). Using these as a qubit requires the ability to perform operations within the $|0\rangle/|1\rangle$ subspace, while not leaking out into any of the higher-lying photon number states. However, because the transition frequency between the states $|0\rangle$ and $|1\rangle$ is the same as the transition frequency between states $|n\rangle$ and $|n+1\rangle$ for any n, and the drive operator $a + a^\dagger$ couples all pairs of states $|n\rangle \leftrightarrow |n+1\rangle$, it is impossible to selectively drive transitions in the desired qubit manifold for this linear oscillator.

The above discussion suggests that if a modification can be made to the LC circuit which makes the spacing between levels differ as one climbs higher up the energy ladder, then we would have a suitable qubit. Thinking classically, a solution is to introduce some nonlinearity into the system: unlike purely linear oscillators, nonlinear oscillators generally have oscillation frequencies which depend on the amplitude of the oscillation. This classical fact corresponds to a quantum system whose transition frequencies depend on the number of quanta of oscillation present in the system, which is exactly what we need. One way to add nonlinearity is to replace the linear inductor with an element known as a Josephson junction, essentially an inductor whose inductance varies with the amount of current passing through it.

Physically, the Josephson junction is comprised of two superconductors sandwiched around an insulating material (in this thesis, the superconductor is aluminum and the insulator is aluminum oxide). The Josephson junction is characterized by a quantity known as the the critical current I_0, and its dynamics are described by the equations

$$V = \phi_0 \frac{d\delta}{dt}, \tag{2.6}$$

$$I = I_0 \sin\delta, \tag{2.7}$$

where $\phi_0 = \hbar/2e$ is the reduced flux quantum and δ is the phase difference between the electronic order parameter characterizing the supercurrent on either side of the insulator. To see this as a nonlinear inductor, rewrite the equations as

$$V = \frac{\varphi_0}{I_0 \cos\delta} \dot{I}, \tag{2.8}$$

and compare the standard $V = LdI/dt$.

In the quantum description of a Josephson junction, the phase difference δ gets promoted to an operator. Much like $\hat{\Phi}$ characterized the inductor, $\hat{\delta}$ characterizes the Josephson junction. Keep in mind that while $\hat{\Phi}$ had units of magnetic flux, $\hat{\delta}$ is dimensionless. Other than that, the two are basically the same. One usually writes the commutation relation involving $\hat{\delta}$ as

$$[\hat{n}, \hat{\delta}] = i, \tag{2.9}$$

where $\hat{n}$ is the number of Cooper pairs on one island of the capacitor. One can view this as the dimensionless version of the commutation relation between $\hat{\Phi}$ and $\hat{Q}$.

As described elsewhere (see, for example, the original paper [33] or the textbook [26] for a more pedagogical source), the Hamiltonian describing the transmon can be written in terms of the above operators as

$$\hat{H} = 4E_C \left(\hat{n} - n_g\right)^2 - E_J \cos\hat{\delta}. \tag{2.10}$$

Here E_C is the charging energy of the capacitor, defined by $e^2/2C$; n_g is the charge offset (imposed by the environment); and E_J, given by $\Phi_0 I_0/2\pi$ (where Φ_0 is the magnetic flux quantum), characterizes the Josephson junction. The transmon typically operates in the regime $E_J/E_C \gg 1$. In this limit, the transmon approximately becomes a slightly anharmonic oscillator, described by the Hamiltonian

$$H = \sqrt{8E_C E_J}\left(\hat{b}^\dagger \hat{b} + 1/2\right) - \frac{E_C}{12}\left(\hat{b} + \hat{b}^\dagger\right)^4, \tag{2.11}$$

where $\hat{b}$ is a standard ladder operator. Calculating the leading-order (in E_C/E_J) corrections to the j^{th} energy level (from the pure harmonic oscillator energy levels), we get

$$E_j^{(1)} = -E_C \frac{j(j+1)}{2}. \tag{2.12}$$

Writing the correction in this way suggests a nice interpretation of the transmon spectrum: note that

$$\frac{j(j+1)}{2} = \binom{j}{2}, \tag{2.13}$$

which is simply the number of pairs that can be formed from j particles. So the interpretation of the anharmonic term is that for every pair of excitations the transmon harbors, we have to pay an energy cost E_C. For a transmon, the anharmonicity is negative, meaning that the energy of a given state is lower than it would be for a purely harmonic oscillator. Typical values of E_J and E_C used in transmons yield frequences of roughly 5 GHz with typical anharmonicities ranging from 100-300 MHz.

The anharmonicity of the transmon sets an approximate speed limit for driving transitions which do not leak out of the $|0\rangle \leftrightarrow |1\rangle$, or qubit, manifold. This can be seen on Fourier grounds: for a pulse whose carrier frequency is on resonance with the $|0\rangle \leftrightarrow |1\rangle$ transition, shortening the duration of the pulse will increase the power in the frequency range near that

of the $|1\rangle \leftrightarrow |2\rangle$ transition (as long as we scale the amplitude of the pulse to compensate for the shorter duration). Since the width of the pulse in frequency space scales inversely with its duration, we might expect that at durations roughly corresponding to the inverse of the anharmonicity (and shorter), there will be significant leakage out of the qubit manifold. This turns out to be true. However, we caution the reader that the Fourier argument is only a heuristic, and is not rigorous. In particular, it is tempting to extend this argument and conclude that a monochromatic drive (i.e., a pulse of infinite duration) at the $|0\rangle \rightarrow |1\rangle$ resonance frequency will *only* drive Rabi oscillations between the two qubit states. This seems to be a common misconception, but is absolutely incorrect. If the drive is applied for infinite time, the anharmonic oscillator will be driven out of its qubit subspace. The reason is that the drive also excites transitions between $|1\rangle$ and $|2\rangle$, albeit suppressed since the drive is off-resonant with this transition. This is something which would not be predicted by the Fourier argument, since the spectral weight of an infinite-duration pulse is zero everywhere but at a single frequency. So one must be careful when using Fourier arguments, even though these arguments are often a useful way to get an approximate understanding of the transmon dynamics. For example, the Fourier intuition correctly predicts that using a pulse with a Gaussian envelope is much better, from a leakage perspective, than using a square pulse of equivalent total area. However, to go beyond this intuition and quantitatively derive a pulse shape which can cancel leakage more fully, one must fully solve the dynamics of the transmon (as is done in [42]) under a coherent drive[1].

2.2 Coupling a Transmon to a Linear Cavity: the Jaynes-Cummings Hamiltonian

It is now standard practice in our field to capacitively couple a superconducting transmon qubit to a linear resonator, in an architecture known as circuit quantum electrodynamics, or circuit QED. A representative circuit model is shown in figure 2.2. Though this thesis focuses on coupling between linear resonators and *transmons* specifically, the architecture is more general than that: Cooper Pair Boxes [63], fluxonium qubits [37], capacitively-shunted [66] and standard flux qubits [58, 46] have all been coupled to resonators in the circuit-QED fashion.

There are two main reasons for coupling a transmon to a resonator, both of which feature in the experiments in this thesis: first, such coupling allows one to measure the state of the transmon (in the computational basis); second, it allows for multiple transmons (coupled to the same resonator) to interact and enables entangling gates to be performed between these qudits. These and other essential features of the resonator-qudit interaction are captured by the Jaynes-Cummings Hamiltonian, which we now discuss.

[1]It is a bit unfortunate that the word *leakage* was chosen to describe this effect, as it might give the idea that the process is somehow mysterious or incoherent. In fact, the effect is coherent, and entirely predicted by the Schrödinger equation for an anharmonic oscillator under drive.

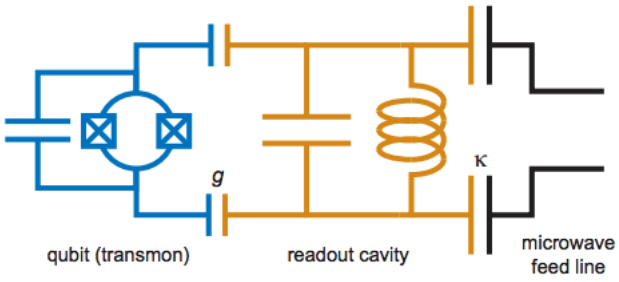

Figure 2.1: Circuit quantum electrodynamics architecture for a transmon qubit coupled to a linear resonator. The transmon qubit is shown in blue, the readout cavity is shown in orange, and the microwave drive line is in black. Figure taken from Dan Slichter's thesis [57].

The Jaynes-Cummings Hamiltonian is a special case of the Rabi Hamiltonian, which reads

$$H_{Rabi}/\hbar = \omega_r \hat{a}^\dagger \hat{a} + \omega_q \hat{b}^\dagger \hat{b} + \frac{\alpha}{2}\hat{b}^\dagger \hat{b}^\dagger \hat{b}\hat{b} + g(\hat{a} + \hat{a}^\dagger) \otimes (\hat{b} + \hat{b}^\dagger). \tag{2.14}$$

Here ω_r and ω_q are the angular resonance frequencies of the linear **r**esonator and transmon **q**udit, respectively[2]; α is the anharmonicity of the transmon, and g is constant (with units of frequency) which parameterizes the strength of the coupling between the two systems. Though it is possible to derive this Hamiltonian from the circuit model [26] shown in figure 2.2, in my experience such a derivation has not proven particularly instructive. Instead, one can simply note that the coupling term has the form expected for two linear resonators coupled by an element which allows them to exchange energy[3]. For example, consider two pendulums coupled by a spring. The interaction potential, given by

$$\hat{V}_{\text{int}}(\hat{x}_1, \hat{x}_2) = \frac{1}{2}k(\hat{x}_1 - \hat{x}_2)^2, \tag{2.15}$$

leads to a coupling term $k\hat{x}_1\hat{x}_2$, which, in terms of the dimensionless ladder operators for each resonator, becomes $k(\hat{a}_1 + \hat{a}_1^\dagger)(\hat{a}_2 + \hat{a}_2^\dagger)$, as in the Rabi model above.

To arrive at the Jaynes-Cummings Hamiltonian, one makes the so-called *Rotating-Wave Approximation*. Note that upon expanding the interaction term in the Rabi Hamiltonian, one is left with four terms:

$$g\hat{a}^\dagger\hat{b}^\dagger, \quad g\hat{a}\hat{b}, \quad g\hat{a}^\dagger\hat{b}, \quad g\hat{a}\hat{b}^\dagger. \tag{2.16}$$

Of these terms, the latter two represent amplitudes for processes in which the resonator gives one quanta of excitation to the transmon, and the reverse. However, the former two represent amplitudes for both the resonator and transmon to jointly gain or discard an excitation. The rotating-wave approximation consists of neglecting these terms. This approximation is

[2]In the case of the transmon, ω_q is strictly the transition frequency between the $|1\rangle$ and $|0\rangle$ Fock states
[3]This type of coupling is known as *transverse*, as opposed to *longitudinal*, coupling

valid when the coupling constant, g, is much lower than the bare resonator and transmon frequencies—in this regime, the energy difference between the states coupled by the $\hat{a}^\dagger\hat{b}^\dagger$ and $\hat{a}\hat{b}$ terms are much greater than the term which couples them, so transitions between these states are suppressed by a factor of $g/(\omega_r + \omega_q)$. This suppression is usually large enough as to be safely neglected: in typical transmon-resonator devices, g is roughly tens of megahertz while ω_r and ω_q are in the gigahertz range.

A justification commonly given for the rotating-wave approximation [57] is that the discarded terms "do not conserve energy." This justification is not precise, and can cause confusion for new students[4] . In particular, the Rabi Hamiltonian, like any Hamiltonian, *defines* the energy of the system it describes. Because it is a Hermitian operator, it is a perfectly valid energy operator for the system, and saying that an individual term does not conserve energy is nonsensical. What people really mean when they say this is the following: treat the uncoupled transmon-resonator system as the *bare* system, and the coupling as a perturbation. In a perturbative calculation, the effects of the non-RWA terms are accompanied by prefactors of $g/(\omega_r+\omega_q)$ (and higher orders), which are small enough to be negligible. Thus, these terms to not conserve the energy of the *bare* system, and are thus neglected. Note, however, that the terms $\hat{a}^\dagger\hat{b}$ and $\hat{b}^\dagger\hat{a}$, strictly speaking, also do not conserve the bare system energy; but, their effects are suppressed by the much larger prefactors $g/|\omega_r - \omega_q|$ and are large enough to contribute to the dynamics of the joint system. Thus, it is safe to discard terms like $\hat{a}\hat{b}$ and $\hat{a}^\dagger\hat{b}^\dagger$ but not $\hat{a}^\dagger\hat{b}$ or $\hat{b}^\dagger\hat{a}$.

Having made the RWA, we are left with the celebrated Jaynes-Cummings Hamiltonian:

$$H_{JC}/\hbar = \omega_r\hat{a}^\dagger\hat{a} + \omega_q\hat{b}^\dagger\hat{b} + \frac{\alpha}{2}\hat{b}^\dagger\hat{b}^\dagger\hat{b}\hat{b} + g(\hat{a}^\dagger\hat{b} + \hat{b}^\dagger\hat{a}). \tag{2.17}$$

As previously described, the interaction term in this Hamiltonian has the intuitive form which describes exchange of a single excitation quanta between the transmon and the resonator.

All of the experiments described in this thesis are performed in the so-called *dispersive* regime of the JC Hamiltonian, in which g is small compared to the difference between ω_r and ω_q. To gain a feel for the physics of this system, in the next section we will temporarily work with a version of the Jaynes-Cummings Hamiltonian in which we replace the transmon with a true qubit or two-level system.[5] This will allow us to understand the origin of the *dispersive shift*, which forms the basis for qubit state measurement. Following this detour, we will put back the transmon as an anharmonic oscillator and describe the resulting changes to the system's dynamics.

[4] An even worse justification is that the discarded terms do not conserve excitation number. Why this should impact the question of whether or not these terms contribute to the dynamics of the joint system is never explained, likely because a satisfying explanation does not exist.

[5] One can think of this as taking the limit in which the anharmonicity, α, goes to minus infinity, but this is probably not very fruitful. It is, however, important to realize that the two-level system and harmonic oscillators are paradigmatic systems which lie on opposite ends of the "anharmonicity spectrum": the harmonic oscillator has no anharmonicity, while the two-level system is as anharmonic as can be.

Dispersive Jaynes-Cummings Hamiltonian with a Qubit

We replace the transmon with a genuine qubit to get the Hamiltonian H_{JC}^{Q}, given by

$$H_{\mathrm{JC}}^{Q}/\hbar = \omega_q \frac{\hat{\sigma}_z}{2} + \omega_r \hat{a}^\dagger \hat{a} + g(\hat{a}^\dagger \hat{\sigma}_- + \hat{a}\hat{\sigma}_+) \tag{2.18}$$

The dispersive regime of this Hamiltonian occurs when the qubit and resonator are far detuned compared with the coupling strength: that is, $\Delta \equiv |\omega_r - \omega_q| \gg g$. In what follows, we will denote the qubit ground and excited states by $|g\rangle$ and $|e\rangle$, respectively. We will call the term $g(\hat{a}^\dagger \hat{\sigma}_- + \hat{a}\hat{\sigma}_+)$ the "coupling" or "perturbation" term.

The essential feature of the dispersive regime is the following: in this regime, the qubit and resonator are essentially non-interacting, *except that* the frequency of the resonator depends on the state of the qubit, and correspondingly the frequency of the qubit depends on the number of photons in the resonator. Precisely, the interaction can be described by the Hamiltonian H_{JC}^{disp}, where

$$H_{JC}^{\mathrm{disp}}/\hbar = \omega_q \frac{\hat{\sigma}'_z}{2} + \omega_r \hat{a'}^\dagger \hat{a'} + \chi \hat{a'}^\dagger \hat{a'} \sigma'_z \tag{2.19}$$

Here χ is known as the dispersive shift, and is equal to half the difference in resonator frequencies corresponding to the two qubit states. A couple comments are in order before discussing how this Hamiltonian is derived:

- First, as indicated by the primes, the qubit and cavity operators in eq. 2.19 are not exactly equal to those in eq. 2.18. Instead, the qubit operators picks up a small cavity component, and vice versa. That is, qubit excitations in the dispersive Hamiltonian, eq. 2.19, consist of superpositions of qubit and cavity excitations in the bare Hamiltonian, eq. 2.18. One consequence of this hybridization is that the decay rate of the qubit is affected by the decay rate of the cavity, in a phenomenon known as the *Purcell effect*. More on that later. Another consequence is that one can drive qubit state transitions simply by driving the resonator, a fact exploited in 3D circuit QED architectures.

- Second, this Hamiltonian is not valid for all photon number states of the resonator, but only those below a certain critical photon number, n_{crit}. The reason for this, as will become clear below, is that the dispersive Hamiltonian is a perturbative approximation to the true Jaynes-Cummings Hamiltonian in eq. 2.18. Because the perturbation contains the ladder operators $\hat{a}$ and $\hat{a}^\dagger$, the matrix elements of the perturbation operator scale as $\sqrt{n}$, where n is the resonator photon number. At a certain photon number, the condition for perturbation theory to be valid, namely that the perturbation matrix elements are well below the bare Hamiltonian matrix elements (which scale as Δ), is no longer fulfilled. From these arguments, it is easy to see that this critical photon number scales as Δ^2/g^2.

With these caveats in mind, let us turn to the derivation of the dispersive Hamiltonian. There are at least a few ways to perform the derivation. For example, one can note that

this Hamiltonian is block-diagonal, only coupling states $|g\rangle \otimes |n\rangle$ with $|e\rangle \otimes |n-1\rangle$. This allows for exact diagonalization, after which one can then take the dispersive limit $g \ll \Delta$. Alternatively, one can perform a change of frame via the unitary operator

$$U = \exp\left[\frac{g}{\Delta}\left(a\sigma^+ - a^\dagger\sigma^-\right)\right] \tag{2.20}$$

and only keep terms to second-order in g.

We will take a simpler approach here, which hopefully sheds more light on how a swap-type interaction ($a^\dagger\sigma_-$) becomes a dispersive interaction ($a^\dagger a\sigma_z$) in the dispersive limit. This approach is just perturbation theory: we treat the coupling term as a perturbation and calculate its effects to second order. In fact, the only formula we need from perturbation theory is the one for second-order energy shifts: the shift is given by the coupling matrix element squared, divided by the energy difference between the coupled states.[6] Looking at figure 2.2, the bare state $|g, n\rangle$ (that is, the state in which n photons reside in the resonator while the qubit lives in its ground state) couples to the state $|e, n-1\rangle$ with a strength $g\sqrt{n}$, while the bare energy difference between these states is simply Δ. Thus, the energy of the $|g, n\rangle$ state gets shifted by an amount ng^2/Δ (and the "partner" state $|e, n-1\rangle$ shifts the same amount in the opposite direction). This is simply the level repulsion phenomenon familiar from perturbation theory. The crucial thing, however, is that the magnitude of the energy shift is proportional to n. So, the energy of the state $|g, n\rangle$, which without perturbation is $\hbar\omega_r n$, is now $\hbar\omega_r n + \hbar n g^2/\Delta$, or $\hbar\left(\omega_r + g^2/\Delta\right)n$. Similarly, the energy of the state $|e, n\rangle$ shifts from $\hbar\omega_r n + \hbar\omega_q$ to $\hbar\left(\omega_r - g^2/\Delta\right)n + \hbar\omega_q$. Thus, the effective frequencies of the ground-state and excited-state manifolds differ by $2g^2/\Delta$, or 2χ.

To complete the derivation, one must calculate the perturbation-induced changes to the states themselves (not only the energies, as we did above). This corresponds to calculating the operators $\hat{a}'$, etc., in terms of the bare operators. We leave this as an exercise for the reader.

The dispersive shift allows for the state of the qubit to be measured by probing the resonator. To perform such a measurement, the resonator is coupled to a transmission line (in either a transmission or reflection geometry), along which is sent a microwave signal near ω_r. Depending on the frequency of the resonator, and thus the state of the qubit, the transmitted/reflected characteristics (i.e. either the phase, amplitude, or both) of the microwave signal will vary. In circuit QED experiments, this signal is digitized, demodulated, and time-averaged, realizing a measurement of the qubit in the σ_z basis.

A useful feature of this measurement scheme is that it is non-destructive. Unlike, say, the measurement of a photon by absorbing it in a photodetector, the dispersive measurement leaves the qubit state in its measured eigenstate. If the qubit state was measured to be $|g\rangle$, the qubit remains in $|g\rangle$ at the end of the measurement. Such a measurement is known as a QND, or quantum non-demolition, measurement. The experiments described here commonly

[6] In a more complicated system, we would have to sum all of these contributions for every state which couples to the state of interest. However, the Jaynes-Cummings system is so simple that the perturbation couples each state only to one other! Namely, the state $|g, n\rangle$ couples only to $|e, n-1\rangle$ and vice versa.

exploit the QND aspect of the dispersive measurement to ensure that the qubit begins each experimental run in its ground state: an initial measurement is performed before each run of the experiment, and the data is postselected for only those runs in which the qubit was measured in $|g\rangle$. This procedure is known as *heralding* [27].

Dispersive Jaynes-Cummings Hamiltonian with higher transmon levels

The physics of the dispersive Jaynes-Cummings regime does not change too much when we add in the higher transmon levels back to the description of the system. Whereas in the qubit case, the dispersive regime featured two "ladders" of states, each one corresponding to a different qubit state and exhibiting a slightly different frequency, in the multi-level transmon case, we have a multitude of harmonic ladders:

$$H_{JC}^{\text{disp,ml}}/\hbar = \omega_r \hat{a}^\dagger \hat{a} + \omega_q \hat{b}^\dagger \hat{b} + \frac{\alpha}{2}\hat{b}^\dagger \hat{b}^\dagger \hat{b}\hat{b} + \hat{a}^\dagger \hat{a}(\chi_e |e\rangle\langle e| + \chi_f |f\rangle\langle f| + \chi_h |h\rangle\langle h| + ...) \quad (2.21)$$

Here we have used the standard nomenclature for the lowest four levels of a transmon, $\{|g\rangle, |e\rangle, |f\rangle, |h\rangle\}$. For qubit state readout, we are typically interested in the difference between the resonator frequencies corresponding to the qubit in $|g\rangle$ vs. the qubit in $|e\rangle$, denoted by χ_{eg}. Whereas in the case of the two-level system, this difference is simply given by $2g^2/\Delta$, in the transmon case the expression for χ_{eg} is slightly more involved:

$$\chi_{eg} = 2\frac{g^2}{\Delta}\frac{\alpha}{\Delta + \alpha} \quad (2.22)$$

Thus, from the expression for χ_{eg} for a qubit, the value of χ_{eg} for a transmon is modified by the factor $\alpha/(\Delta + \alpha)$. For all of the experiments in this thesis, α is lower than Δ by a factor of five or so. This makes χ_{eg} lower in magnitude for transmons than for a true two-level system.

How do we derive this expression? It turns out to also come easily from perturbation theory. And as long as we care only about the χ_{eg}, that is, only the difference between the ground- and excited-state resonator frequencies, we only have to consider the lowest three levels of the transmon in the derivation. The relevant states of the system are shown in figure 2.2. In the previous section, we discussed how the state $|g, n\rangle$ had its energy shifted by coupling to the state $|e, n-1\rangle$; this was responsible for shifting the frequency of the ground-state ladder from ω_r to $\omega_r + g^2/\Delta$. That part of the derivation is unchanged. The excited state ladder, however, is changed from the two-level case; here, the level $|e, n\rangle$ couples *both* to $|g, n+1\rangle$ and $|f, n-1\rangle$. Unless the cavity frequency is in between the frequency of the $|g\rangle \leftrightarrow |e\rangle$ and $|e\rangle \leftrightarrow |f\rangle$ transitions,[7] the shift from the $|f, n-1\rangle$ level opposes that from the $|g, n+1\rangle$ level. Due to the coupling via the transmon ladder operators, the coupling

[7] This is known as the *straddling regime* of operation

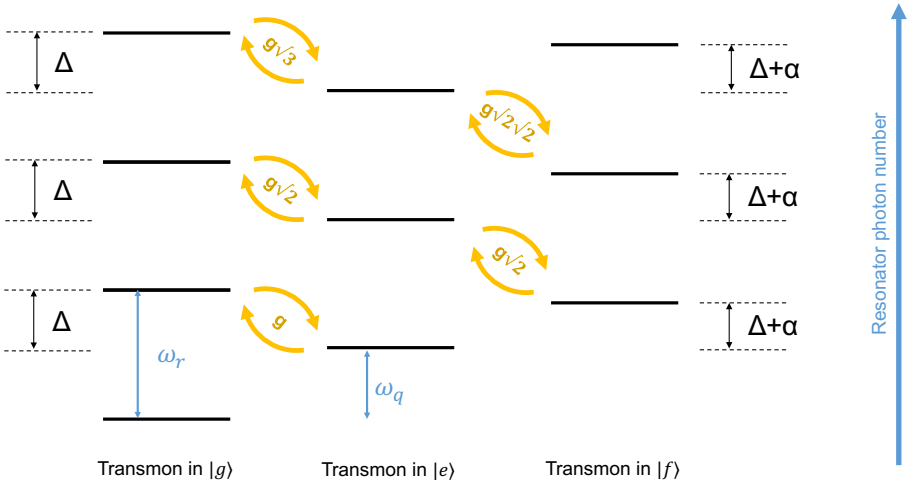

Figure 2.2: Jaynes-Cummings ladder showing how the level repulsion leads to a dispersive shift in the multi-level transmon case. The modification to the resonator frequency when the transmon is in its ground state is unchanged from the two-level system case, but the excited-state ladder is modified due to the presence of the $|f\rangle$ level.

between the $|f, n-1\rangle$ and $|e, n\rangle$ levels is stronger than that between the $|g, n+1\rangle$ and $|e, n\rangle$ levels by a factor of $\sqrt{2}$. So the dispersive shift is reduced by

$$(\sqrt{2}g)^2/(\Delta + \alpha), \tag{2.23}$$

and thus becomes

$$\chi_{eg} = \frac{2g^2}{\Delta} - \frac{2g^2}{\Delta + \alpha} = 2\frac{g^2}{\Delta}\frac{\alpha}{\Delta + \alpha}, \tag{2.24}$$

which we had given above. Again, the upshot is simply that for a given value of g, the transmon dispersive shift is smaller than it would be if the higher levels were absent, unless the system is in the straddling regime.

Coupling first: an alternative description

In the above description of the coupled transmon-cavity system, we treated the coupling between the transmon and cavity as a perturbation on top of the bare transmon + cavity system. There is an alternative viewpoint, developed by groups at Yale [43] and Sherbrooke/IBM [10], which gives a slightly different picture of the system. This alternative picture, which we will call the black-box quantization picture (after Yale's 'black-box quantization' paper) is useful both for conceptual intuition, and because it makes the calculation

of some quantities (such as the induced nonlinearity of the 'bare' resonator[8]) more straightforward.

In the black-box quantization picture, instead of treating the coupling between the transmon mode and the cavity mode as a perturbation, we include it from the beginning and instead treat the nonlinearity induced by the Josephson junction as a perturbation. That is, we take as the bare Hamiltonian

$$H_0^{BBQ} = \omega_c a^\dagger a + \omega_q b^\dagger b, \tag{2.25}$$

where ω_c is the 'bare' cavity frequency and ω_q is the 'bare' qubit frequency. Now to describe the nonlinearity, we include the term H_{nl}^{BBQ} corresponding to the junction. Since the energy of a junction of Josephson energy E_J is given by $-E_J \cos\phi$, where ϕ is the flux across the junction, we might think that H_{nl}^{BBQ} should be equal to $-E_J \cos\phi$, but this is not exactly right. The reason is that if we were to Taylor-expand the cosine term around $\phi = 0$, we would find a term proportional to ϕ^2, which is the Hamiltonian term corresponding to a linear inductance. This linear term is already accounted for in the bare Hamiltonian H_0^{BBQ}, so we don't need it in the nonlinear part. Thus the nonlinear term should be

$$H_{nl}^{BBQ} = -(E_J/\hbar)(\cos\phi + \phi^2/2 - 1) = (E_J/\hbar)(\frac{\phi^4}{24} - \frac{\phi^6}{720} + O(\phi^8)) \tag{2.26}$$

Treating this Hamiltonian as a perturbation, we will keep only the ϕ^4 term above. We now need a relation between the ϕ operator (the phase across the junction) and the ladder operators a and b. From the discussion above about the transmon, we know that the ladder operators resemble those for a one-dimensional position/momentum harmonic oscillator, except with position and momentum replaced by phase and charge, respectively. So, for a junction coupled to a single linear mode, the ϕ operator would be $a + a^\dagger$; since we have two modes which both couple to the junction, the ϕ operator is a linear combination of both modes:

$$\phi = c_1(a + a^\dagger) + c_2(b + b^\dagger), \tag{2.27}$$

where c_1 and c_2 are functions of the geometry of the circuit. While precise expressions for these can be found in the original paper [43], note that for most circuits we consider, c_1 will be much smaller than c_2, since the transmon (described by b) will couple much more strongly to the junction than the cavity (described by a).

Now expanding the ϕ^4 term and keeping only those terms which respect the rotating-wave approximation, we arrive at a description of the circuit which looks like this:

$$H_{disp}^{BBQ} = \omega_c a^\dagger a + \omega_q b^\dagger b - \frac{1}{2}\chi_{qq} b^{\dagger 2} b^2 - \chi_{cq} a^\dagger a b^\dagger b - \frac{1}{2}\chi_{cc} a^{\dagger 2} a^2, \tag{2.28}$$

where χ_{qq} and χ_{cc} are known as the 'self-Kerr' coefficients of the qubit and cavity modes, respectively, while χ_{cq} is known as the cross-Kerr coupling between the qubit and cavity

[8]In this thesis, the only time this quantity is relevant is in the quantum walk experiment, in which the transmon coupled to the quantum walk cavity induces a nonlinearity on the cavity

modes. Looking carefully at this Hamiltonian, we see that the effect of the junction has been to endow both the qubit and cavity modes with nonlinearity, in two forms. The first form (self-Kerr) of nonlinearity, given by the terms $\frac{1}{2}\chi_{qq}b^{\dagger 2}b^2$ and $\frac{1}{2}\chi_{cc}a^{\dagger 2}a^2$, manifests as a shift in the resonance frequency of each mode as it is populated with photons. The second form (cross-Kerr), described by the $\chi_{cq}a^\dagger a b^\dagger b$ term, shows that the frequency of either mode shifts when photons are added to the *other* mode. That is, populating the cavity with photons shifts the frequency of the transmon (by an amount χ_{cq} for each photon), and likewise populating the transmon with photons shifts the frequency of the cavity (by an amount χ_{cq} for each photon).

We have met two of these terms before (in the Jaynes-Cummings description): χ_{qq}, the self-Kerr coefficient of the qubit, is none other than the qubit anharmonicity; and χ_{cq}, the cross-Kerr coefficient, is what we called the dispersive shift χ before. But out of this analysis has popped out a new term, the self-Kerr coefficient describing the nonlinearity of the a mode, which—go back and look at the dispersive Jaynes-Cummings Hamiltonians—seemed to be entirely linear. There's a good reason we hadn't seen this term before: in the description where we treat the coupling as a perturbation, it only appears when we go out to fourth order in perturbation theory (try it![9]), and we ended our calculation at second-order. As might be expected from this fact, the self-Kerr term of the cavity is much smaller than that of the transmon: a good rule of thumb ([43]) for the relation between the three nonlinear coefficients is that:

$$\chi_{cc} = \frac{\chi_{cq}^2}{4\chi_{qq}} \tag{2.29}$$

Taking typical values for the dispersive shift to be around a megahertz, and the transmon anharmonicity to be about two-hundred megahertz, gives that the self-Kerr coefficient of the cavity is on the order of a kilohertz. This means that for typical photon numbers with which we populate the cavity (during, for example, state measurement), the frequency shift is conservatively in the range of tens of kilohertz, and usually does not contribute much to the dynamics of the system.

Apart from allowing us to calculate the value of the self-Kerr coefficient of the 'linear' cavity, this coupling-first description suggests an appealing mental picture of the transmon-cavity system, where both the transmon and cavity are on an equal footing as non-linear oscillator modes, which are coupled by a longitudinal (cross-Kerr) interaction. The distinction is that the anharmonicity of the transmon mode (or, more precisely, the ratio of the anharmonicity and the linear frequency) is much greater than that of the cavity mode; i.e., the cavity is 'more linear' than the transmon.

[9] Don't try it.

Chapter 3

Cooling in a Bose-Hubbard Chain

In this chapter, we describe an experiment which uses a chain of three transmon qubits to emulate a many-body Hamiltonian known as the Bose-Hubbard model. This Hamiltonian describes the physics of spinless bosons on a lattice interacting via a contact potential. Traditionally, experiments on the Bose-Hubbard Hamiltonian have been limited to cold atomic systems, in beautiful realizations of this model with ultracold bosonic atoms in optical lattices [22]. A prime example of this is the *quantum gas microscope*, which allows for the measurement of individual lattice site populations [7]! Using the quantum gas microscope, a phase transition from a superfluid phase to a (Mott-)insulating phase has been observed with single-site resolution.

Superconducting circuits offer a potentially complementary approach to simulating interacting Hamiltonians. While cold atomic gases contain up to millions of atoms, individual control over these systems is not yet available. Further, these gases must be cooled from an initially hot ensemble; precise preparation of an initial state requires evacuating a great deal of entropy from the gas. By contrast, with superconducting qubits we can build up complex systems from the ground up, with individual control built into the chip.

A few years prior to the experiment discussed in this chapter, a technique known as *bath engineering* was implemented in a system consisting of a single superconducting qubit. In bath engineering, one uses dissipative rather than coherent control to prepare or stabilize certain desired states. That is, rather than engineering a coherent Hamiltonian or unitary operation to effect dynamics, with bath engineering one engineers a dissipative interaction to effect the desired change in the system state. Though dissipation is usually seen as an obstacle to performing precise manipulations of quantum systems, a simple example can show why dissipation can be a valuable resource: consider the task of initializing a set of qubits in the joint ground state, $|0\rangle^{\otimes N}$. Without knowing the initial state of the qubits, this initialization would be impossible using only coherent dynamics. However, if one is able to engineer a fast T_1-like decay of the qubits, this initialization becomes easy.

The key result reported in this chapter is the use of bath engineering to prepare complex, many-body states of our three-transmon Bose-Hubbard simulator. In essence, this shows that bath engineering can be a valuable tool in the near future as analog quantum simulators build

up to more complex systems. Three aspects of this result are worth highlighting: first, the bath-engineering protocol we develop allows us to drive dissipative state-transitions which preserve particle number, something which (due to frequency constraints) would be tough with coherent control; second, our protocol allows for the efficient preparation of so-called 'dark states', which, due to symmetry, cannot be prepared via coherent drive on the system; and finally, we are able to combine coherent driving with dissipative bath-engineering to realize 'autonomous feedback,' indefinitely stabilizing particular states of the Bose-Hubbard array.

This chapter first introduces the Bose-Hubbard Hamiltonian and shows how it can be realized with superconducting circuits. We then describe our three-transmon experimental system, and show the initial spectroscopic measurements to confirm the validity of the Bose-Hubbard description. We then characterize the natural decay dynamics of the system as a prelude to the final result: applying bath engineering to alter the natural decay rates and achieve state stabilization. A quick note on terminology: bath engineering, dissipation engineering, and cooling are all used interchangeably throughout this chapter; the term autonomous feedback is reserved for the combination of dissipative and coherent driving to stabilize a state.

3.1 Realizing the Bose-Hubbard Hamiltonian with Transmon Qubits

The Bose-Hubbard Hamiltonian reads

$$H = -\sum_{\langle i,j \rangle} t_{ij} \hat{b}_i^\dagger \hat{b}_j + \frac{U}{2} \sum_i \hat{n}_i \left(\hat{n}_i - 1\right) - \sum_i \mu_i \hat{n}_i. \tag{3.1}$$

Here $\hat{b}_i$ ($\hat{b}_i^\dagger$) is a creation (annihilation) operator for a boson on lattice site i, and $\hat{n}_i \equiv \hat{b}_i^\dagger \hat{b}_i$ is the boson number operator which counts the number or particles on site i. Since the particles are bosons, the operators $\hat{b}_i$ satisfy the canonical commutation relations

$$\left[\hat{b}_i, \hat{b}_j\right] = \left[\hat{b}_i^\dagger, \hat{b}_j^\dagger\right] = 0 \tag{3.2}$$

$$\left[\hat{b}_i, \hat{b}_j^\dagger\right] = \delta_{ij} \tag{3.3}$$

Examining each term in eq. 3.1 individually, we see that the first (with the notation $\langle i, j \rangle$ indicating that the sum is to be taken over pairs of *neighboring* lattice sites) represents tunneling of particles between neighboring sites, with amplitude $-t$. The second term represents the interaction cost of placing more than one particle on a given lattice site. In the Bose-Hubbard Hamiltonian, the interaction between particles is taken to be a *contact interaction*, in that particles do not feel any repulsion unless they reside on precisely the same lattice site. Each pair of particles must pay an interaction energy U (which is positive if the interaction is repulsive and negative if the interaction is attractive); since a set of n

particles hosts $n(n-1)/2$ pairs, the interaction term has the form given in eq. 3.1. Finally, the third term in the Hamiltonian, the offset energy, represents the energy of each particle due to being placed on a lattice site; each site can have a different energy μ_i if the lattice is inhomogeneous. Here we assume only one orbital per lattice site. Since all the particles are bosons, they can simply bunch up in this single orbital.

It might be straightforward to understand how this Hamiltonian describes interacting bosonic atoms in an optical lattice potential, but how does one realize this Hamiltonian in a system of transmons? Imagine an array of transmons, each capacitvely coupled to some neighbors, and think of each excitation of the transmon as the bosonic particle. As we have described in the previous chapter, the coupling term between neighboring transmons i and j takes the form

$$H_{\text{cpl}} = \hbar J(b_i^\dagger b_j + b_j^\dagger b_i), \tag{3.4}$$

exactly analogous to the tunneling term in the Bose-Hubbard Hamiltonian. Similarly, the linear term in the individual Hamiltonian of transmon i is simply

$$H_{\text{i}} = \hbar\omega_i b_i^\dagger b_i, \tag{3.5}$$

mirroring the offset energy of each lattice site. So all that is left to show is that the transmon harbors an effective on-site interaction term with the same form as that in eq. 3.1. This term comes from the anharmonicity. We discussed previously that in the limit of high E_J/E_C, the anharmonic (or non-linear) correction to the transmon spectrum takes the form

$$H_{\text{NL,i}} = \hbar\frac{\alpha}{2} b_i^\dagger b_i^\dagger b_i b_i, \tag{3.6}$$

where α (a negative number for the transmon) is the difference between the transition frequencies of the $|G\rangle \leftrightarrow |E\rangle$ and the $|E\rangle \leftrightarrow |F\rangle$ transitions. At first glance, this does not look like the same spectrum as in the Bose-Hubbard model, but a bit of rearranging using the commutation relation $\left[\hat{b}_i, \hat{b}_i^\dagger\right] = 1$ yields the equivalent form

$$H_{\text{NL,i}} = \hbar\frac{\alpha}{2} n_i(n_i - 1), \tag{3.7}$$

which is identical to the Bose-Hubbard contact interaction term. In fact, this suggests a productive way to view the anharmonicity of the transmon: every additional excitation placed on the transmon incurs an energy cost of α for every excitation already present. One must keep in mind, however, that this approximation is only valid for the low-lying energy levels of the transmon; further, while the true Bose-Hubbard Hilbert space consists of states with all possible excitation numbers, in a transmon, as we described previously, there are only of order ten bound states. Whenever in doubt, it is always possible to go back to the exact solution of the Mathieu equation to check the validity of the approximation.

Putting aside these thoughts on the approximate nature of the description, we have seen that an array of coupled transmons is described by the Bose-Hubbard Hamiltonian. One

feature which emerges immediately is that, due to the negative anharmonicity of the transmon, the interaction term in the transmon Bose-Hubbard chain is always attractive: given two excitations to distribute among two identical transmons, it is energetically favorable to dump both of them on the same transmon rather than split them apart. Interestingly, in cold atomic systems, experimentally realizing regimes with attractive interactions is quite challenging; it turns out that by a process called three-body losses, trapped atoms can bind into molecules which are no longer trapped by the optical and/or magnetic confining forces. This process occurs in general cold-atom setups but is particularly exacerbated by attractive interactions. Luckily, for excitations on transmons, no corresponding decay process occurs. This is one sense in which the superconducting simulation platform we discuss here is complementary to cold atomic setups.

3.2 Chip design

We turn now to discussing our experimental realization of the Bose-Hubbard model with transmons, beginning with the design of the chip. Our chain features three transmon qubits, each capacitively coupled to its nearest neighbor(s). We expect that this capacitive coupling is the dominant coupling mechanism in the chain; however, indirect coupling of the qubits via interaction with the cavity in which they reside may also contribute to the measured coupling terms.

A drawing of the chip is shown in figure 3.1(a), alongside a schematic representation of the surrounding 3D cavity and low-temperature measurement/control hardware. The chip itself is silicon, and the transmon qubits are made of aluminum, fabricated using a single-step shadow-evaporation procedure. For (static) frequency control, the qubits on the outsides of the array use SQUID loops for their Josephson inductance, while the qubit in the center is a fixed-frequency qubit with a single Josephson junction. The chip is mounted in the center of the cavity. To tune the frequency of each qubit, we used two coils of (superconducting, NbTi) wire[1]: one wrapped around the cavity, producing a field of roughly equal strength at the location of each SQUID, and a smaller coil offset from the center of the cavity to produce a field with different strength at each SQUID. In theory, this arrangement should have allowed arbitrary frequency control of the qubits, but in practice, we did not need to use this capability. As will be discussed later, we simply wanted to be able to tune the qubits sufficiently to measure their coupling strengths via avoided crossings, and to place them in a regime where they were nearly degenerate for the bath engineering study.

Here we give more details about our chip, postponing a more in-depth discussion of how these values were measured/calibrated for the next section. Our device consists of three transmon qubits [33] on a single silicon chip. Each qubit is formed by two aluminum pad-

[1]One of my favorite memories working on this project was when Shay, an excellent experimentalist and otherwise way more knowledgeable than me, mistakenly thought that the wire was made out of a copper-scandium mixture because the website uses the abbreviation 'CuSc' to denote the composition ratio of the copper matrix to the superconducting (NbTi) wire.

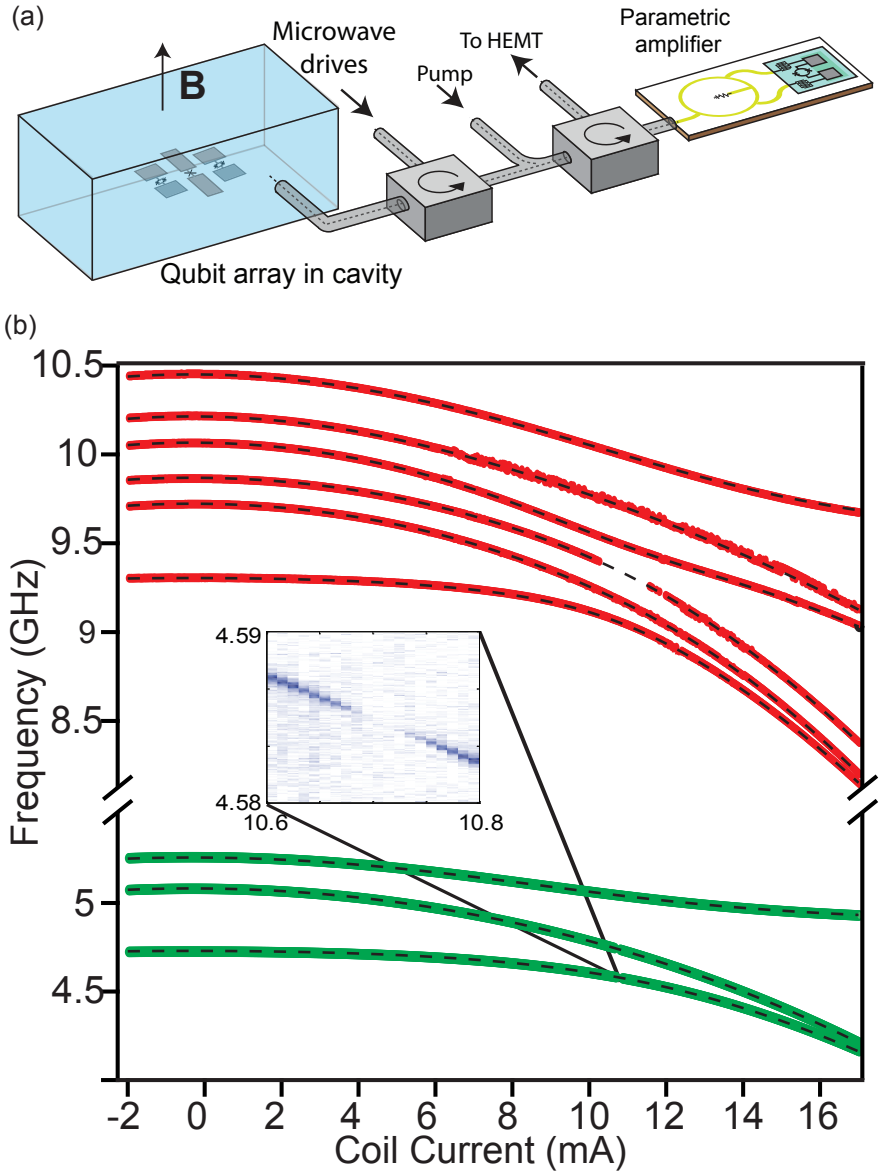

Figure 3.1: (a) A schematic (not to scale) of the experimental setup described in the text. (b) Spectroscopically measured eigenfrequencies of the one- and two-particle states of the array as a function of current through the external bias coil. For a given current, the flux through the two SQUIDs in the array differs by 2.5%; 17 mA roughly corresponds to a quarter of a flux quantum. Solid lines denote measured frequencies with fits to the 1D Bose-Hubbard Hamiltonian shown as overlaid dashed lines. Red lines correspond to two-particle states; green lines are one-particle states. The inset shows raw data near the $|E_1\rangle$ frequency, from which the darkness of the $|G\rangle \rightarrow |E_1\rangle$ transition discussed in the text becomes apparent.

dles, connected by either a single double-angle-evaporated Al/AlO_x/Al Josephson junction (middle qubit) or a superconducting quantum interference device (SQUID) consisting of two junctions (outer qubits). The qubit array is located in the center of a copper waveguide cavity with dressed frequency $\omega_c/2\pi = 7.116$ GHz and $\kappa/2\pi = 10$ MHz. Each qubit couples to the cavity via a Jaynes-Cummings $\hat{\sigma}_x(\hat{a} + \hat{a}^\dagger)$ interaction with strength g_i. Because the middle qubit is located in the center of the cavity where the $\vec{E}$-field strength is greatest and its paddles are longer, it couples to the cavity more strongly than the outer qubits, with strengths $g_{mid}/2\pi = 264 \pm 7$ MHz and $g_{out}/2\pi = 155/149 \pm 7$. The outer qubits are characterized by a charging energy $E_c/h = 214$ MHz, which also gives us the absolute value of the anharmonicity for a transmon ($\alpha = -E_c/h$), and have a Josephson energy which gives, at zero flux, $\omega_{q1}/2\pi = 5.074$ GHz for the left qubit and $\omega_{q3}/2\pi = 5.165$ GHz for the right. For the middle qubit, $E_c/h = 240$ MHz and the qubit frequency is $\omega_{q2}/2\pi = 4.892$ GHz. The qubits are spaced by 1 mm, giving a nearest-neighbor coupling strength of $J/h = 177$ MHz and a next-nearest-neighbor coupling stength of $J_{13}/h = 26$ MHz, with uncertainties of a couple of MHz mainly due to the uncertainty in the calibrated g_i values.

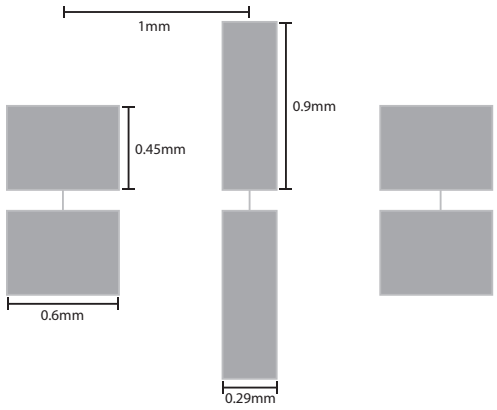

Figure 3.2: To scale layout and dimensions of the chip with the three transmons. Josephson juctions are not illustrated.

The dimensions and layout of the chip placed in the cavity are shown in Fig. 3.2. As can be seen, the transmons have slightly different dimensions, so that they interact with the cavity with different strengths (since the field of the fundamental cavity mode is roughly uniform over the dimensions of the small chip, the difference in interaction strengths comes primarily from the different antennae configurations). In our chip the interaction between the cavity and the transmon in the middle is nearly twice as strong as that between the cavity and the transmons on the end of the array. Numerical simulations indicated that this mismatch in coupling strengths would improve achievable cooling rates.

Coupling between the transmons themselves comes from two sources: cavity-mediated interactions and direct capacitve (or dipole-dipole) coupling. Cavity-mediated interactions arise when both qubits couple to the cavity mode, as described in ref. [36]. This coupling

strength is $J_{ij\ \text{cavity}} = \frac{1}{2} g_i g_j (\frac{1}{\Delta_i} + \frac{1}{\Delta_j})$, about 20 MHz for adjacent qubits and 10 MHz for edge-edge coupling, at the working point of the experiment. Direct dipole-dipole coupling, discussed in refs. [60, 1], arises from the capacitance between transmon paddles. In our case, this coupling is on the order of 150 MHz for adjacent qubits, and 10 MHz for the qubits on the edge.

3.3 Initial spectroscopic calibrations

With the chip, coils and cavity put together, the entire assembly was mounted at the base stage of one of our lab dilution refrigerators, known as *Sisyphus*. A single microwave line coupled the cavity to the measurement setup. Referring to figure 3.1(a), the line labeled 'Microwave drives' is used to send all of the tones used in the experiment (coherent control, microwave readout, and bath-engineering drives) to the cavity-qubit system; the line labeled 'Pump' is used to apply a microwave bias tone to the parametric amplifier for readout; and the line labeled 'To HEMT' is connected to the HEMT amplifier (at 4 Kelvin) to further amplify the readout tone, after which it exits the fridge for demodulation and digitization.

Initial calibrations are performed using standard methods. There are two types of parameters to calibrate: parameters describing the qubit-cavity Hamiltonian, which impact the coherent dynamics of the system; and parameters describing the non-unitary evolution (decoherence and decay) arising from coupling to other systems. Specifically, the total Hamiltonian of the system is given by $H = H_{\text{cav}} + H_{\text{array}} + H_{\text{int}}$, where

$$H_{\text{cav}} = \hbar\omega_c \left(a^\dagger a + 1/2\right) \tag{3.8}$$

describes the mode of the cavity which couples to the qubits;

$$H_{\text{array}} = \hbar \sum_{j=1}^{3} \left(\omega_j b_j^\dagger b_j + \frac{\alpha_j}{2} b_j^\dagger b_j^\dagger b_j b_j\right) + \hbar J \sum_{j=1}^{2} \left(b_{j+1}^\dagger b_j + b_j^\dagger b_{j+1}\right) + \hbar J_{13} \left(b_1^\dagger b_3 + b_3^\dagger b_1\right) \tag{3.9}$$

describes the array of three transmons; and

$$H_{\text{int}} = \hbar \sum_{j=1}^{3} g_j \left(b_j a^\dagger + b_j^\dagger a\right) \tag{3.10}$$

describes the interaction between the transmons and the cavity. Note that in the array Hamiltonian, we have added a term which allows direct hopping of an excitation between the two qubits on the ends of the array. This term can either exist due to direct capacitive coupling of the outer transmons, or by coupling through the cavity. Parameters which describe the decay dynamics are the linewidth, κ, of the resonator, as well as the decay times (T_1, T_2) of the qubits.

We extract first the frequency and linewidth of the cavity via spectroscopy, finding that the the cavity frequency (with the qubit array in its ground state, or more accurately, in its

thermal-equilibrium state) is 7.116 GHz with a linewidth, κ, of $2\pi \times 10$ MHz.[2] This linewidth is dominated by coupling of the resonator to the transmission lines.

Next, we use *two-tone spectroscopy* to measure the qubit frequencies, and further, the frequencies of the array eigenstates as a function of applied magnetic flux. To do this, we apply one microwave tone to the cavity near the resonance at 7.116 GHz and measure its phase shift as we sweep a second tone, intended to drive the qubits out of their ground state. The dispersive shift between the qubits and cavity causes a change in the reflected phase shift when the qubit is driven, allowing us to determine the frequency accurately.

It is helpful to group eigenstes of the array Hamiltonian into categories based on the total excitation number. Since the Bose-Hubbard Hamiltonian conserves total particle number, eigenstates of the three-qubit array can be grouped into manifolds characterized by this quantum number. In our experiment, we work with the zero, one, and two-particle manifolds, comprising respectively one, three, and six states. We denote the zero-particle state by $|G\rangle$, the single-particle states by $\{|E_i\rangle,\ i \in [1,3]\}$, and the two-particle states by $\{|F_j\rangle,\ j \in [1,6]\}$, with increasing subscript value indicating higher-energy states. The dispersive interaction between each qubit and the cavity transforms into a dispersive pull exerted by each eigenstate of the cavity on the array. It is this dispersive shift which allows us to perform spectroscopy on the array energy levels.

We perform spectroscopy to extract, as a function of applied magnetic flux, the eigenergies of the nine lowest-lying excited states of the array with respect to the global zero-particle ground state. For the initial spectroscopy experiment, we only apply current to the coil wrapped around the cavity (which applies a roughly uniform field to each tunable qubit). We probe the array for coil currents between -2 and +17 mA.

Since the qubit population without any excitation predominantly lies in $|G\rangle$, standard two-tone spectroscopy reveals the $|G\rangle \rightarrow |E_1\rangle$, $|G\rangle \rightarrow |E_2\rangle$, and $|G\rangle \rightarrow |E_3\rangle$ transitions. To perform this spectroscopy, the reflected phase of a tone near the cavity resonance is continuously monitored as a second tone sweeps from 3.7 to 5.3 GHz. This measurement results in Fig. 3.3a, with three main lines indicating the single-particle energies (that is, the energies of the $|E_1\rangle$, $|E_2\rangle$, and $|E_3\rangle$ states).

Extraction of the two-particle energies is more involved. For the $|F_6\rangle$ state, the energy can be directly measured via a two-photon transition from $|G\rangle$, as shown in Fig. 3.3b. For all other $|F_i\rangle$ states, however, the energies must be measured indirectly via transitions from a single-particle state. We use $|E_1\rangle$ and $|E_3\rangle$ as stepping stones to measure the $|E_1\rangle \rightarrow |F_i\rangle$ and $|E_3\rangle \rightarrow |F_i\rangle$ transitions, by running two additional spectroscopy scans: one with the addition of a tone at the $|G\rangle \rightarrow |E_1\rangle$ frequency, and another with the addition of a tone at the $|G\rangle \rightarrow |E_3\rangle$ frequency. The results of this 'three-tone spectroscopy', shown in Fig. 3.3b, allow the identification of all six two-particle states.

Using the results of the two- and three-tone spectroscopy, we can extract the energies

[2]Because the qubits affect the cavity frequency, the cavity frequency shifts by roughly a MHz when the qubit frequencies are tuned. The value given here is the frequency when 10 mA is applied to the uniform bias coil. This is the bias point used in the bath engineering portion of the experiment.

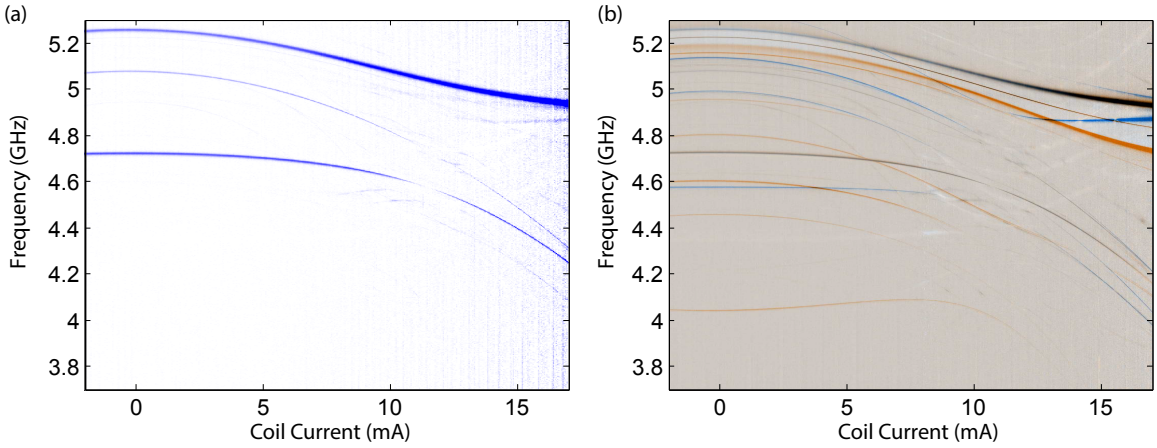

Figure 3.3: Raw data from spectroscopy, showing (a) the $|G\rangle \rightarrow |E_i\rangle$ transitions probed with two microwave tones, and (b) the $|E_1\rangle \rightarrow |F_i\rangle$ (blue) and $|E_3\rangle \rightarrow |F_i\rangle$ (red) transitions probed with three microwave tones.

of all of the states in the one- and two-particle manifolds. These results are plotted in fig. 3.1(b). we extract parameters of our device by fitting these values to predictions based on the Bose-Hubbard Hamiltonian with an additional next-nearest-neighbor coupling term. After taking into account the variation of the qubit frequencies with flux, that Hamiltonian is

$$\hat{H} = \hbar \sum_{i=1}^{3} \left(\omega_i(\phi) \hat{b}_i^\dagger \hat{b}_i + \frac{\alpha_i}{2} \hat{b}_i^\dagger \hat{b}_i^\dagger \hat{b}_i \hat{b}_i \right) + \hbar J \left(\hat{b}_1^\dagger \hat{b}_2 + \hat{b}_2^\dagger \hat{b}_3 + h.c. \right) + J_{13} \left(\hat{b}_1^\dagger \hat{b}_3 + h.c. \right) \tag{3.11}$$

with the qubit frequency as a function of flux described by $\omega(\phi) = \omega_{0i} \sqrt{\cos\left(B_i I + A\right)}$ for the outer qubits with SQUIDS (for the middle qubit ω is constant). The parameters B_i for each edge qubit are the ratio between the current applied to the coil and the flux threading the qubit's SQUID loop, and A is an overall offset due to potential flux trapped in the SQUID loops during cooldown.

As shown in Fig. 3.1, our measurement of the system's one- and two-particle energy states agrees well with predictions based on the attractive 1D Bose-Hubbard Hamiltonian. This is the key takeaway from the spectroscopy measurements: we have verified that, at least up to energy spectra, our three-transmon system is accurately described by the Bose-Hubbard Hamiltonian which we intended to model.

Using the second coil (which applies flux differently to the two tunable qubits), we can move the qubits into frequency regimes in which each qubit is well-separated from the other two (by a factor of roughly ten times the tunneling energy). Here we can extract two more parameters for each qubit: the qubit-cavity couplings g_i and the qubit charging energy E_c/h. The qubit-cavity couplings were measured using a technique based on a combination

of the AC Stark shift and measurement-induced dephasing from a tone at the cavity frequency, while the charging energy was taken to be, in a crude approximation, simply the anharmonicity of each transmon. The charging energy is thus roughly the on-site attractive interaction energy.

It is interesting to look at the parameter regime of the Bose-Hubbard model in which we find ourselves: typically, the quantity of interest here is the ratio between the the on-site interaction energy and the tunneling energy. Our system lies in the parameter regime where the competing tunneling ($J/2\pi \sim 180$ MHz) and on-site interactions ($\alpha/2\pi \sim -220$ MHz) have nearly equal strength.

Bright and dark states

A striking feature observable in spectroscopy, which will become important later on, is the presence of *bright* and *dark* states. By this we mean that certain states (deemed 'bright') are very visible in spectroscopy, while others ('dark') are almost invisible in spectroscopy. We show this for the lowest-lying state of the single-excitation manifold $|E_1\rangle$, in the inset of figure 3.1(b), and one can see it more clearly for both $|E_1\rangle$ and $|E_2\rangle$ in figure 3.3(a). This darkness occurs when the coupling matrix element between the hybridized eigenstate and the cavity—or, equivalently, the electric dipole matrix element between the particular eigenstate and the array's ground state—vanishes. Since this matrix element is very sensitive to qubit frequencies, the darkness only occurs at certain values of the coil current.

If we are interested in coherently populating eigenstates of the array via a transverse microwave drive, this darkness poses a problem, as the required matrix element is small or zero. However, we will see in later sections that by using the bath engineering technique, this limitation can be circumvented. Specifically, we can populate one of the bright states in the array and then use bath engineering to dissipatively prepare a dark state.

Let us take a moment to see how well we can model the location (in flux) of the dark states in the single-excitation manifold. To do so, we can calculate the matrix element of the interaction operator $H_{int} = \hbar \sum_{j=1}^{3} g_j (b_j a^\dagger + b_j^\dagger a)$ between the states $|S, 0_{ph}\rangle$ and $|G, 1_{ph}\rangle$, for desired array eigenstate $|S\rangle$. This calculation yields

$$d_{S,G} = |\langle \Psi_S | H_{int} | \Psi_G \rangle| = \hbar \left| \langle 0_{ph}|a|1_{ph}\rangle \langle S| \sum_{j=1}^{3} g_j b_j^\dagger |G\rangle \right|. \tag{3.12}$$

In Fig. 3.4 we plot this coupling $d_{E,G}$ for the $|E\rangle$-states to ground state G, as a function of flux (current in the coil). The figure shows that the theory is qualitatively in agreement with the measurements. $|E_3\rangle$ is predicted to be always bright, in agreement with the spectroscopy image Fig 3.3. Both $|E_1\rangle$ and $|E_2\rangle$ states instead become dark at a specific value of the flux (current in the coil). There is some uncertainty in the location of this dark spot due to the uncertainty $\Delta g_j = \pm 7$MHz in the measured values of the couplings g_j, which affects this result significantly. Theoretically we find: $I_{dark}(E_1) = 11.3 \pm 0.7$mA and $I_{dark}(E_2) = 13.1 \pm 0.7$mA. These predicted values are shown, with the corresponding error bar, in Fig. 3.4.

Experimentally the measured values are: $I^{exp}_{dark}(E_1) = 10.71$ mA and $I^{exp}_{dark}(E_2) = 10.64$mA; these are marked with a single dashed vertical line in Fig. 3.4 (the two lines are too close to be distinguished on the scale of the graph). The measured value $I^{exp}_{dark}(E_1)$ fits within the uncertainty range of the theoretical prediction; however, $I^{exp}_{dark}(E_2)$ is somewhat off the theoretical prediction, and it is also slightly smaller than $I^{exp}_{dark}(E_1)$, contrary to what the theory would predict.

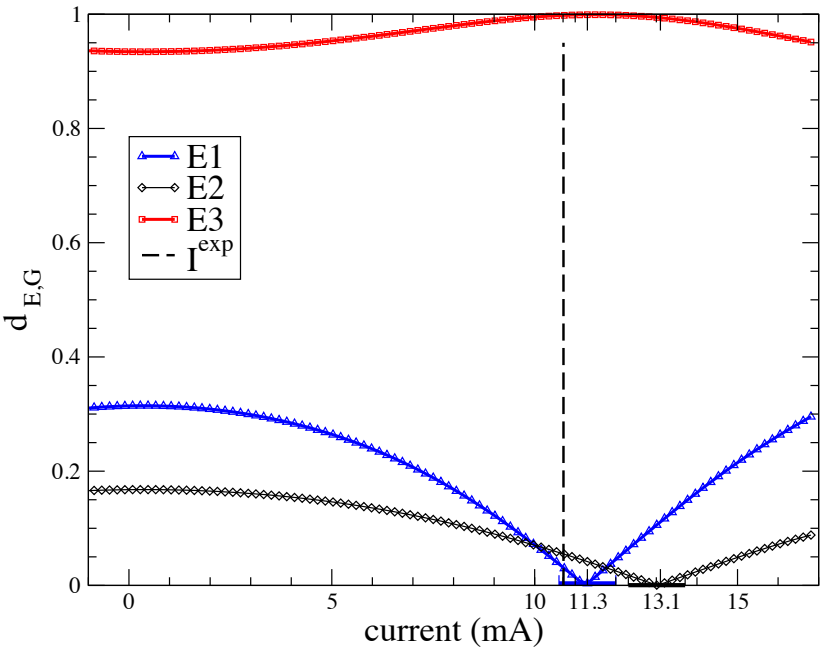

Figure 3.4: Bright and dark features of the E-manifold states. The figure shows the predicted coupling $d_{S,G}$ in Eq. (3.12) between a state S in the single-excitation manifold and the cavity pulse. The vertical line show the experimental value for which the states E_1 and E_2 become dark (the values are very close so cannot be distinguished). The error bars for the theoretical location of the dark point for the E_1 and E_2 states are shown along the horizontal axis.

3.4 Natural decay dynamics

We now turn to discussing the natural decay dynamics of the array. This characterization was done in the absence of any bath-engineering drives in order to better understand the behavior of the array when left to decay into its own, 'naturally occurring' bath. For the majority of

the rest of this chapter, we will work at a flux bias point of 10 mA. Before discussing features of the decay dynamics themselves, we describe how we perform time-domain measurements of the array by using its dispersive coupling to a single cavity mode.

Dispersive readout of the Bose-Hubbard array

Dispersive readout of a single qubit is a standard technique in the field of circuit QED, but typically in these experiments each qubit in the system is coupled to its own readout resonator; in such a situation only two (or sometimes three) states of the transmon need to be distinguished. The challenge in the current experiment is that we are interested in ten states of the array (all of the ones in the zero-, single-, and two-excitation subspaces). Without careful engineering of the couplings to the array, reading out all ten states with high fidelity in a single shot measurement would be essentially impossible. Luckily, none of the experiments we conduct on the array require us to be able to measure the array state in a single shot. Capitalizing on this fact, we can measure averaged populations of each of the eigenstates reasonable well.

Due to the dispersive coupling between the qubits and the cavity, each array eigenstate induces a shift in the resonant frequency of the readout cavity. The frequency corresponding to the array in $|G\rangle$ is measurable simply via the reflected phase measurement on a network analyzer, as the array is in its global ground state without excitation pulses. As described previously, this frequency is 7.116 GHz when our system is biased up to 10 mA. To measure the resonator frequencies corresponding to the excited states, we use microwave pulses to prepare the array in the desired eigenstate $|i\rangle$, then measure the reflected phase θ_i of a 7.116 GHz tone, referenced to the reflected phase with the array in $|G\rangle$. This measurement was done using our parametric amplifier in phase-preserving mode. The standard equations for a reflected phase shift from a resonator yield that the frequency shift χ_i for a given eigenstate is related to θ_i by the equation $\chi_i = \kappa/2 \tan(\theta_i/2)$. The measured reflected phase angle θ_{exp} and the corresponding χ_{exp} are shown in Table 3.1. In the same table are also shown the χ shifts calculated theoretically. In figure 3.5, examples of the histogrammed phase shifts are shown. Except for $|F_3\rangle$ and $|F_4\rangle$, all of the states are resolvable. In fact, by using the parametric amplifier in phase-sensitive mode and adjusting the measurement frequency and amplification axis (phase of the detected quadrature), we can obtain additional separation between states of interest for a particular experimental run.

To extract the population of a given state after a particular experimental sequence, we repeat the sequence several ($\sim$ 1 million) times and histogram the measured phase or quadrature amplitude values. After the run, we take a set of calibration histograms, in which we prepare all ten states and immediately make a measurement with the same frequency and amplification axis used in the experiment. We then fit the measured histograms to a sum of Gaussians with the same mean and variances as the calibration histograms, and from the amplitudes of each Gaussian, extract the corresponding state's population during that run.

Natural decay dynamics were measured by coherently initializing the system in the state of interest, waiting for a time, then measuring the array state, as described above. This is

Table 3.1: Theoretical and experimental dispersive shifts of the linear cavity coupled to the Bose-Hubbard array

state	θ_{exp}(rad)	χ_{exp}/κ	χ_{th}/κ
E1	1.37	0.41	0.49
E2	0.74	0.19	0.26
E3	1.43	0.43	0.48
F1	2.09	0.86	1.07
F2	1.64	0.53	0.68
F3	1.82	0.64	0.75
F4	1.77	0.61	0.70
F5	2.03	0.80	0.82
F6	2.16	0.93	0.90

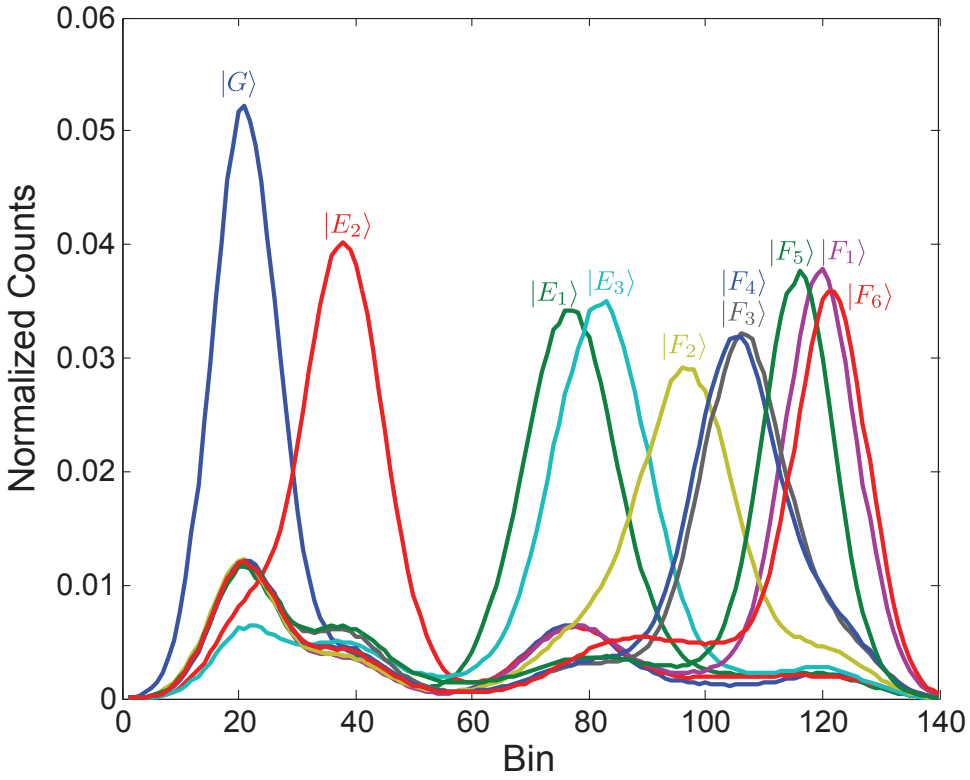

Figure 3.5: An example of calibration histograms, showing each state in the lowest-lying ten energy states of the array. Apart from states $|F_4\rangle$, and $|F_3\rangle$, each states is resolvable given enough measurement records.

essentially a T_1 sequence for a single qubit, except that we initialize not in the single-qubit excited state, but in an array eigenstate. We fit the population dynamics for each state to a

Table 3.2: T_1 experimental fitted downward decay times in μs

state	$\omega/(2\pi)$ GHz	T_1(tot)	$T_1(E_1)$	$T_1(E_2)$	$T_1(E_3)$	$T_1(G)$
E_1	4.6078	28.5				28.5
E_2	4.7854	30.5				30.5
E_3	5.06916	3.2				3.2
F_1	9.1184	18.0	20.4	151		
F_2	9.2592	15.1	30.3	30.1		
F_3	9.4230	8.8	13.5	25.4		
F_4	9.5618	4.6	5.3	34.6		
F_5	9.7788	3.1	100.7	3.3	70.0	
F_6	10.0539	1.5	20.6	42.6	1.6	

decay model given by the matrix rate equation $\partial_t \vec{c} = \Gamma \vec{c}$, where $\vec{c}$ is a vector containing all of the state populations as a function of time and Γ a matrix with transition rates between states. This procedure is similar to that used by Peterer et al. [49] in their study of a single transmon qubit.

Based on previous measurements of multi-level decay in transmons [49], our model does not include direct transitions from the two-particle manifold to the zero-particle ground state. We also suppress transitions between states in the same manifold, since these transition frequencies are on the order of a few hundred MHz, and the photon shot noise spectrum which plays a dominant role in dissipation for this system has very little support at these frequencies. So, for each state in, say the $|E\rangle$ manifold, we only allow downward transitions to the ground state $|G\rangle$. For each of the states in the $|F\rangle$ manifold, we allow it three different downward decay rates, one to each of the states in the $|E\rangle$ manifold. Best-fit parameters are given in table 3.2, and were used to generate the natural decay map in fig. 3.6 which we discuss in the next section. For the bath engineering decays which will be discussed later, a similar model was used for the fit, with the addition of parameters for the intramanifold decay; all intermanifold rates were held fixed to the previously-measured natural values.

Errors in the fit, primarily at low population, occur likely due to effects such as spontaneous T_1 decay which cause the readout histograms to be skewed from their nominally Gaussian shape. See [19] for a detailed explanation of this effect.

Features of the natural decay dynamics

Examples of the population measurements as a function of time for the natural decays decays are shown in Fig. 3.6a-b, for two states in the $|F\rangle$ manifold. In (a), for example, we see that state $|F_5\rangle$ decays quite fast, with an overall T_1 of just 3.1 microseconds. Moreover, the decay is almost entirely to the $|E_2\rangle$ state, which we can see gets rapidly populated before decaying to the $|G\rangle$ state later. The precise fit shows that the decays to the other states in the $|E\rangle$ manifold are slower by almost two orders of magnitude. By contrast, in Fig. 3.6b, we see

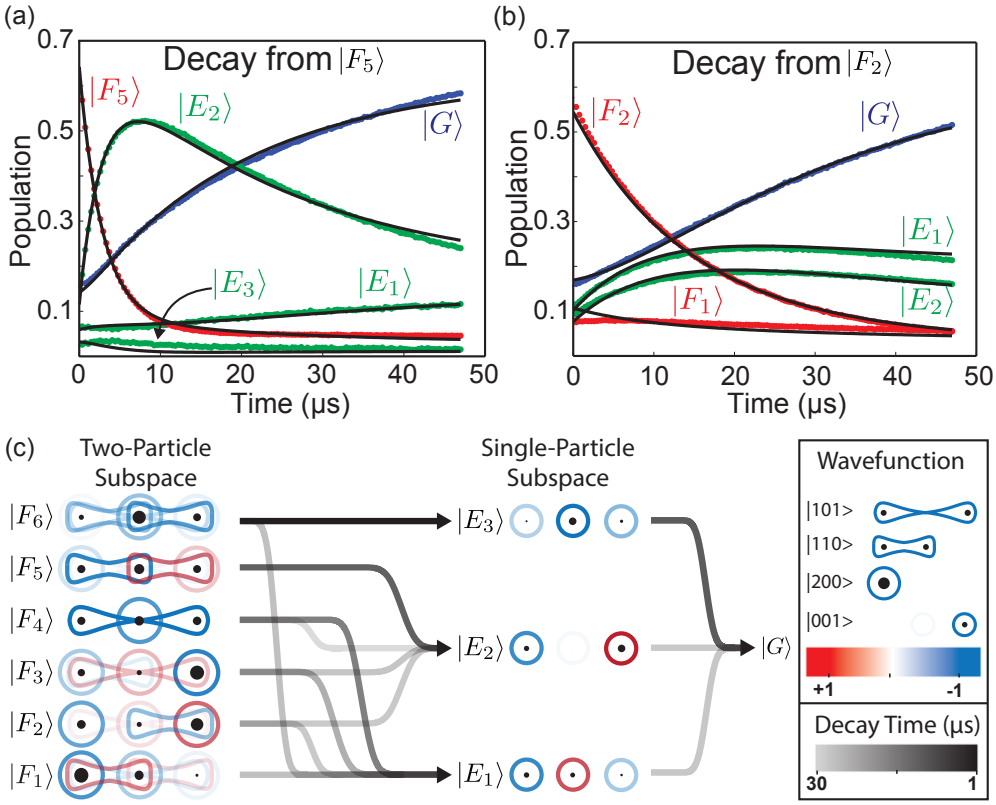

Figure 3.6: (a) and (b) Examples of spontaneous decays from two-particle states to the global ground state via the one-particle subspace. In (a), $|F_5\rangle$ decays rapidly and almost entirely to $|E_2\rangle$, which then decays to $|G\rangle$, while in (b), $|F_2\rangle$ decays with roughly equal rates to $|E_1\rangle$ and $|E_2\rangle$. Overlaid black lines are obtained from fitting the decay data for all nine excited states to a single rate-equation model. (c) An illustration of the natural decay pathways of the system, from the two-particle subspace on the left, through the one-particle subspace in the middle, to the zero-particle state on the right. Each black arrow represents a decay channel, with the opacity of the line indicating the rate of the transition. Darker lines indicate faster rates, as the legend shows. Also shown are representations of the eigenstate wavefunctions in the qubit basis. The black circle radius is proportional to the mean particle number.

that the $|F_2\rangle$ state decays with similar rates to the $|E_1\rangle$ and $|E_2\rangle$ states. Let us emphasize that all of the decays were fit with a single model.

A striking feature of the natural decay dynamics is the discrepancy between decay times of different states in the same manifold. For example, $|E_1\rangle$ and $|E_2\rangle$ live for $\sim 30\mu s$, while $|E_3\rangle$ decays much more quickly, in $\sim 3\mu s$. This is due to the substantially different dipole transition matrix elements that each single-particle state $|E_i\rangle$ exhibits with respect to the final state $|G\rangle$. A related consequence of these dipole moments is shown in the inset of Fig. 3.1(b), where at 10.71 mA, as discussed previously, $|E_1\rangle$ goes fully dark, i.e. becomes

Table 3.3: T_1 experimental fitted *upward* decay time in μs

state	$\omega/(2\pi)$ GHz	T_1(tot)	$T_1(E_1)$	$T_1(E_2)$	$T_1(E_3)$	$T_1(G)$
E_1	4.6078	82.4				82.4
E_2	4.7854	182.3				182.3
E_3	5.06916	167.0				167.0
F_1	9.1184	104.2	104.2			
F_2	9.2592	82.0	237.5	125.2		
F_3	9.4230	45.3	98.1	84.2		
F_4	9.5618	36.7	43.3	239.4		
F_5	9.7788	9.7	50.8	28.2	20.7	
F_6	10.0539	3.0	9.8	33.6	5.0	

impossible to excite via a coherent microwave pulse. Under only Purcell decay—in the absence of material losses in the system—such a dark state would live indefinitely, making it attractive for shelving an excitation if it could be readily prepared. We will return to the preparation of these dark states as one application of our bath engineering protocol.

Because the array is in contact with a bath which is at non-zero temperature, we observed that upward transition rates were also necessary to fit the observed decay curves. These rates are given in table 3.3. In most cases, they are much smaller than the corresponding downward decay rates, indicating that the sample is relatively cold.

Theoretical T_1 decay times

How well do the decay times we measure match our theoretical expectations? We expect decay to be caused mainly by the Purcell effect, by which the coupling of the array to the leaky cavity causes the cavity state to leak as well. We can calculate this decay rate, and compare the calculation to the measured values. We calculate the Purcell relaxation rate as the decay rate of a qubit-array state due to the action of the bare cavity operator a; this operator destroys a photon and induces transitions to lower states. In order to estimate the rate for such a process to occur, we compute the overlap between the $|E_i\rangle$ and $|F_j\rangle$ states and the bare cavity mode a.

The T_1 times found from the above analysis are shown in Table 3.4. Compare these to the measured T_1 decays shown in Table 3.2 for the downward rates. In most of the cases, the theoretical prediction for T_1 is of the same order of magnitude as the experimentally measured value. Nevertheless, there are some qualitative discrepancies. For instance, the theoretical T_1 times for the F-states are in general shorter than the measured ones. We attribute this to the limitation of the single-mode cavity model which can be shown to predict a shorter life-time than a model which takes into account higher modes of the 3D cavity. A more mundane discrepancy arises from the fact that as the $|E_1\rangle$ and $|E_2\rangle$ are almost dark states, their dominant decay channel is not Purcell decay via coupling to the cavity, but rather on-chip material losses.

Table 3.4: T_1 theoretical Purcell-limited decay time in μs

state	$\omega/(2\pi)$ GHz	T_1(tot)	$T_1(E_1)$	$T_1(E_2)$	$T_1(E_3)$	$T_1(G)$
E_1	4.61164	97				97
E_2	4.85539	80				80
E_3	5.0196	0.6				0.6
F_1	9.11862	20	32	201	93	438
F_2	9.3201	7.5	8.8	57	705	>1ms
F_3	9.48676	1.3	1.3	50	212	>1ms
F_4	9.64465	1.2	1.3	69	30	182
F_5	9.7987	0.6	49	0.6	159	>1ms
F_6	9.97278	0.9	78	>1ms	1.17	5.7

3.5 Cooling via an engineered bath

By altering the quantum noise spectrum of the bath interacting with the Bose-Hubbard chain, we can modify the system decay dynamics. In our cooling protocol, this alteration takes the form of an additional microwave drive incident on the cavity, red-detuned from the cavity resonance by an amount Δ_c, as illustrated in Fig. 3.7(a) for the $|E_2\rangle$ to $|E_1\rangle$ transition. This induces quantum photon shot noise whose spectral density peaks at frequency $|\Delta_c|$ [17]. When $\hbar\Delta_c$ matches the energy difference between the arrays initial state $|j\rangle$ and a lower eigenstate $|i\rangle$, the emission of a photon at the cavitys resonance frequency mediates a so-called cooling transition from $|j\rangle$ to $|i\rangle$. The energy gained from the cooling transition augments the incident photon energy to allow emission on resonance. Similarly, a blue-detuned drive induces heating transitions to array states of higher energy. The rate for these processes will depend on both the Raman-transition matrix element between the initial and final array states and on the incident photon flux. The transition rate increases with photon flux up to a value of $\approx \kappa$, saturating there since the dissipative process requires the emission of a photon by the cavity. Since κ is much larger than most of the natural decay rates, this technique is well suited to driving otherwise inaccessible particle-number-conserving transitions in our system.

To characterize the cooling dynamics, we initialize the system into an $|E_i\rangle$ or $|F_j\rangle$ eigenstate and subsequently apply a cooling drive for a variable time and measure the state of the array. Cooling rates are extracted via a fit to a model similar to that used for the natural decays, with additional parameters to capture the induced intramanifold transitions. Because the cavitys density of states exhibits a Lorentzian profile with width κ, so will the transition rate as a function of cooling drive frequency, as shown for the $|E_2\rangle$ to $|E_1\rangle$ transition in Fig. 3.7(c).

For incident powers which cool at a rate $\Gamma_{i\to j}$ much lower than κ, a Fermi Golden Rule calculation shows that

$$\Gamma_{i\to f} \propto P_{in} \left|M_{if}\right|^2 \frac{\kappa}{\left(\omega_i - \omega_f + \Delta_c\right)^2 + (\kappa/2)^2} \tag{3.13}$$

where P_{in} is the incident cooling drive power and M_{if} the matrix element connecting the states $|i\rangle$, $|f\rangle$, of the cooling operator which describes the effect of the dissipative bath; in other words, M_{if} quantifies the coupling between the states $|i\rangle$ and $|j\rangle$ indirectly via the cross-Kerr terms that couple the qubits with cavity. The predicted linear scaling of the peak Γ with P_{in} is shown in the inset of Fig. 3.7(c) for the $|E_2\rangle$ to $|E_1\rangle$ transition. $|M_{ij}|$ provides a measure of the efficacy of each transition; we map out this value for each pair of eigenstates, showing the results in Fig. 3.7(e).

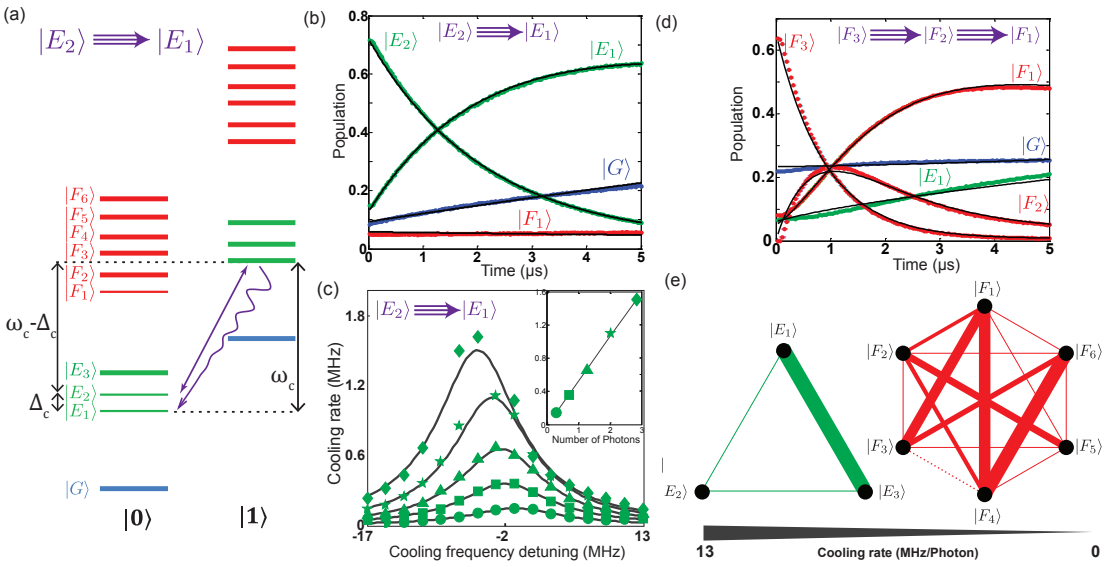

Figure 3.7: (a) An approximate representation of the eigenstates of the array-cavity system; states in the left-hand (right-hand) column contain zero (one) cavity photons. In this picture, our cooling process can be understood qualitatively as follows (taking $|E_2\rangle \rightarrow |E_1\rangle$) as an example: the cooling drive at frequency $\omega_c - \Delta_c$ induces a transition from $|E_2\rangle|0\rangle$ to $|E_1\rangle|1\rangle$, where the second ket indicates the cavity photon number. The cavity state $|1\rangle$ decays via photon emission, leaving the system in the state $|E_1\rangle|0\rangle$, as desired. (b) Example of cooling from $|E_2\rangle \rightarrow |E_1\rangle$ at an incident power corresponding to 1.3 drive photons in the cavity. (c) The cooling rate versus drive frequency is Lorentzian, centered around $\omega_c - (E_2 - E_1)$, with linewidth roughly κ. As the drive power is increased, the Lorentzian peak shifts due to a Stark shift of the relevant transition frequency. The inset shows that in the regime where the cooling rate is much lower than κ, the rate scales linearly with incident power. (d) Example of cascaded cooling, where the system is cooled from $|F_3\rangle$ to $|F_1\rangle$ via the intermediate state $|F_2\rangle$. (e) Connected graphs representing the measured cooling rates per photon in the linear regime for the one- (left) and two- (right) particle subspaces, with the width of the line indicating the rate of the corresponding transition. The dispersive shifts for the $|F_3\rangle$ and $|F_4\rangle$ states are almost identical, so they cannot be distinguished by our measurement. We thus do not measure cooling from $|F_4\rangle$ to $|F_3\rangle$.

Calibration of the Bath Engineering Drive Power

Calibration of powers used to drive the bath-engineering transitions is done in the standard circuit-QED manner [20]: first the qubit-cavity χ-shift is calibrated, then with this value known, the intracavity photon number is then inferred from the Stark shift on the qubit. To do this, in our system, we tune the edge qubits to below 3 GHz, decoupling from the middle qubit. We then measure the χ-shift between the middle qubit and the cavity by measuring, for a variety of incident powers at the cavity frequency, both the measurement-induced dephasing rate and the resulting Stark shift. As shown in Ref. [20], the measurement-induced dephasing rate is $8\chi^2\bar{n}/\kappa$, while the Stark shift is $2\chi\bar{n}$, so by comparing the slopes of these lines vs. power, we extract χ (since κ is known). From there, we use the Stark shift to calibrate the intracavity photon number over the range of frequencies and powers used in the bath-engineering experiment.

Cascaded cooling

In most cases, applying a drive whose frequency is targeted to cool $|i\rangle$ to $|j\rangle$ has no effect on the decay dynamics of the other states, as most cooling drive frequencies are spaced apart by more than several linewidths κ. However, when multiple cooling frequencies are separated by less than κ, a single drive can give rise to a so-called cascaded cooling effect, whereby multiple cooling transitions happen in sequence. In our system, for example, the $|F_3\rangle \rightarrow |F_2\rangle$ and the $|F_2\rangle \rightarrow |F_1\rangle$ transitions are separated by only 17 MHz, so a single tone can cause the system to cascade from $|F_3\rangle$ to $|F_1\rangle$ via the intermediate state $|F_2\rangle$, as shown in Fig. 3.7(d). In the specific example shown, since the cooling matrix element between $|F_3\rangle$ and $|F_2\rangle$ is substantially lower than that of $|F_2\rangle$ and $|F_1\rangle$ ($M_{21} \approx 5M_{32}$), we cooled with the drive frequency tuned to the $|F_3\rangle \rightarrow |F_2\rangle$ transition; this achieved approximately equal cooling rates from $|F_3\rangle$ to $|F_2\rangle$ and $|F_2\rangle$ to $|F_1\rangle$. Cascaded cooling sequences could be useful in larger many-qubit systems with manifolds containing several closely spaced eigenstates.

Using cooling drives to prepare a dark state

Here we show an application of the cooling protocol we have developed in this chapter: namely, it can be used to prepare the system in states which are otherwise tough to initialize using a single coherent drive. For example, the transitions $|G\rangle \rightarrow |E_1\rangle$, $|G\rangle \rightarrow |E_2\rangle$, and $|E_i\rangle \rightarrow |F_1\rangle$ do not interact strongly with the electromagnetic environment of the cavity on account of the symmetry of the states; this decoupling is responsible for their relatively long lifetimes. Correspondingly, however, it is difficult to coherently initialize these states via direct transitions, but our cooling scheme affords their efficient preparation. To illustrate this, consider the $|G\rangle \rightarrow |E_1\rangle$ transition, which as shown in Fig. 3.1, is at its darkest at a flux bias of 10.71 mA. At this bias point, we use the Raman cooling protocol to prepare $|E_1\rangle$ indirectly via the $|E_3\rangle \rightarrow |E_1\rangle$ cooling transition. Further, by combining coherent drives with Raman cooling, we stabilize $|E_1\rangle$ indefinitely against particle loss. As the first part of

Fig. 3.8 illustrates, this is done by coherently driving the $|G\rangle$ to $|E_3\rangle$ with a Rabi frequency of 7 MHz while applying a drive to cool the $|E_3\rangle \rightarrow |E_1\rangle$ transition at a rate of 3 MHz. We next use $|E_1\rangle$ as a stepping stone to stabilize the two-particle ground state $|F_1\rangle$, as shown in the lower part of Fig. 3.8. To accomplish this we add two additional drives, an extra coherent drive from $|E_1\rangle \rightarrow |F_4\rangle$ with a Rabi frequency of 7 MHz, and a cooling drive from $|F_4\rangle \rightarrow |F_1\rangle$ with a rate of approximately 3 MHz. Observed fidelities, while inline with a rate matrix calculation, are primarily limited by the spurious thermal population of dark states, which can be reduced by additional cooling tones. This initialization and maintenance of the array in the ground state of a specific particle-number manifold will be a valuable resource for a hardware simulator.

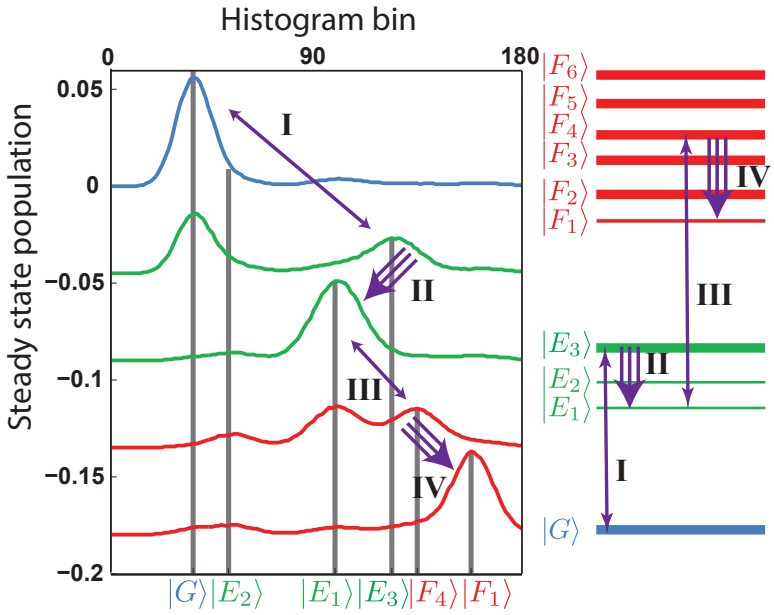

Figure 3.8: Steady state population at the different stages of the persistent stabilization scheme of the two particle ground state $|F_1\rangle$. The top trace shows the thermal equilibrium population, where 78% of the population is in $|G\rangle$. In each subsequent trace a further drive is added: first a coherent drive $|G\rangle \rightarrow |E_3\rangle$ (I), then cooling from $|E_3\rangle \rightarrow |E_1\rangle$ (II), coherent drive from $|E_1\rangle \rightarrow |F_4\rangle$ (III), and finally a cooling drive from $|F_4\rangle \rightarrow |F_1\rangle$ (IV). At the end, 67% of the population is in the desired state, $|F_1\rangle$. $|F_4\rangle$ contains the bulk, 13%, of the residual population. Single-particle ($|E_1\rangle$) stabilization achieves a population of 80%.

How does this initialization compare with attempts to populate the dark states using coherent microwave drives? In theory, without dephasing and dissipation, and in the absence of higher Jaynes-Cummings energy states, one could drive coherent transitions to the desired state except at the singular flux bias point where the matrix element of this transition is exactly zero. In practice, for experimentally available drive powers, driving an almost-dark transition may take such a long time that dissipation (qubit T_1, T_ϕ, cavity loss) reduces

the fidelity to unacceptable values. This was the case at a flux bias of 10 mA (where the single-particle states were almost dark), where, in contrast to the usual coherent pulses which take tens of nanoseconds (we used 64 ns for the coherent pulses), the pulse took around 1 s to excite the $|G\rangle \rightarrow |E_1\rangle$ transition, and this caused our fidelity to be limited to about 65 percent (compare the cooling process, which achieved a fidelity for the single-excitation state of 80 percent). Another limitation of the coherent excitations is that, due to higher levels in the spectrum, off-resonant transitions which have a higher dipole moment than the dark transition may be driven before the desired transition. This was the case at 10.71 mA (complete darkness), where even at the maximum power we could excite with, we saw no population in the $|E_1\rangle$ state, but at these powers higher states (either in the two-excitation subspace or in an even higher manifold; from the dispersive shifts it was difficult to tell properly) began to get populated.

3.6 Conclusion

In this chapter, we have realized a three-qubit transmon array and spectroscopically verified that it obeys an attractive 1D Bose-Hubbard Hamiltonian up to the ten lowest-lying eigenstates, highlighting the use of circuit QED in simulating otherwise challenging quantum systems. Our developed cooling and stabilization protocols, based on quantum bath engineering–a well-studied phenomenon in quantum optics–afford effective control over this solid state system. The capabilities demonstrated here–engineering decay dynamics and stabilizing particular eigenstates–show that dissipation engineering can be a valuable tool as superconducting circuits scale up in complexity to complement simulators based on cold atoms and trapped ions.

Chapter 4

Observing Topological Invariants: Theory

In this chapter, we turn from studying and controlling the dynamics of interacting many-body systems to probing a purely single-particle phenomenon: the occurrence of topological invariants in quantum walks. Using the toolbox available in circuit QED, it is possible to perform a direct measurement of a topological invariant associated with a given one-dimensional walk. We describe the underlying theory in this chapter; the next chapter describes our experimental implementation of the quantum walk in cQED and measurement of the corresponding topological invariant.

4.1 Background: topological features of quantum walks

The discrete-time quantum walk (DTQW), which we will focus on here, is the quantum analogue of the familiar classical random walk. In its simplest, one-dimensional incarnation, the classical random walk involves a walker (sometimes imagined to be an intoxicated patron leaving a bar) moving stochastically along a line. At each time step, the walker flips a coin, and depending on the outcome of the toss, moves either one step left or right. If the coin is fair, then as every student of physics knows, after many time steps the random variable describing the walker's position is described by a Gaussian distribution with root-mean-square deviation proportional to the square root of the elapsed number of time steps. It might be helpful for understanding the quantum case to note that the classical protocol actually encompasses a *family* of different walks: the coin has a bias, between 0 and 1, each one corresponding to a walk featuring different dynamics.

Generalizing this to the quantum case is straightforward. First, one must form the relevant Hilbert space. The Hilbert space of the walker, $\mathcal{H}_W$, consists of discrete position states $|n\rangle$, where n is integer-valued. The Hilbert space of the coin, $\mathcal{H}_C$, is that of a quantum two-level system, whose basis states we will denote $|\uparrow\rangle$ and $|\downarrow\rangle$. The total Hilbert space $\mathcal{H}_T$

is the tensor product of the two, i.e. $\mathcal{H}_T = \mathcal{H}_W \otimes \mathcal{H}_C$.[1] Whereas in the classical case, the walker started at a definite location, we can also (though this turns out to be relatively unimportant when exploring topological features) initialize the combined walker-coin in a definite state, which for convenience we take to be $|\psi_0\rangle = |0\rangle \otimes |\uparrow\rangle$; that is, the walker is initially on lattice site zero with the coin in the spin-up state. Because we are working with discrete-time quantum walks, it is natural to think of the dynamics as arising from the repeated application of a unitary operator U_W. This unitary consists of two parts: a coin toss and a spin-dependent translation. The coin toss, parameterized by a real angle θ, is simply a rotation applied to the coin subsystem. We will take this rotation to be about the y-axis of the Bloch sphere and thus write it as $R_y(\theta) = \exp(-i(\theta/2)\sigma_y)$.

The connection between quantum walks and topological physics was first made in 2010 by Takuya Kitagawa and colleagues at Harvard [31]. The discussion in this section is largely in the spirit of that original work. Briefly, the idea is the following: the unitary operator U_W which generates the walk dynamics defines an effective Hamiltonian H_{eff} via the relation $\exp -iH_{\text{eff}} = U_W$. Since it is a lattice Hamiltonian, this effective Hamiltonian exhibits the standard features which accompany periodic potentials, namely a periodic bandstructure. Corresponding to each quasimomentum or k-vector in the Brillouin zone is a spin eigenstate, or point on the Bloch sphere. The way in which the Bloch vector varies across the Brillouin zone defines the topological phase of the walk. Let us now make the above notions concrete.

Though we will be primarily concerned—both in this chapter and the next—with the so-called *split-step* quantum walk, we will introduce the topological features of quantum walks using the simpler *single-step* quantum walk. First, we write explicitly the walk unitary U_W and its effective Hamiltonian. Defining a spin-dependent translation operator $\hat{T}_{\uparrow\downarrow}$ as

$$\hat{T}_{\uparrow\downarrow} = \sum_x |x+1\rangle\langle x| \otimes |\uparrow\rangle\langle\uparrow| + |x-1\rangle\langle x| \otimes |\downarrow\rangle\langle\downarrow|, \tag{4.1}$$

each step of the single-step quantum walk proceeds via the following protocol:

- Apply the operator $R_y(\theta)$ to the coin system, leaving the lattice Hilbert space alone, and then
- Apply the spin-dependent translation operator $\hat{T}_{\uparrow\downarrow}$, shifting the spin-up component of the wavefunction by a single lattice site to the right and the spin-down component to the left.

Clearly, we have described not just a single protocol but a set of protocols, parameterized by the rotation angle θ. So, let us write $U_W(\theta)$ to make this dependence explicit.

Before proceeding to derive the effective Hamiltonian and topological features of this quantum walk, note that this protocol naturally couples the spin and orbital motion of

[1] When we initially started to think implementing a quantum walk with superconducting circuits, we imagined an implementation with many qubits in a line, in which each qubit would play the part of one site for the walker. In hindsight, this was obviously a wrong approach: the Hilbert space for N qubits is $\mathcal{H}_C^N$, not what we need!

the walker. Those familiar with topological insulators in the condensed-matter context will recognize that spin-orbit coupling is often associated with topological phases of matter, so it should be no surprise to find topological features in a quantum walk.

Though the protocol described above is naturally stroboscopic, we can instead imagine that the dynamics are generated by time-evolution under a static Hamiltonian, $H_{\text{eff}}(\theta)$. Like the unitary $U_W(\theta)$, each value of θ corresponds to a different effective Hamiltonian. Specifically, if we can find an $H_{\text{eff}}(\theta)$ such that

$$\exp -iH_{\text{eff}}(\theta) = U_W(\theta), \tag{4.2}$$

then we can say that $U_W(\theta)$ effectively simulates the dynamics of $H_{\text{eff}}(\theta)$ (here we work with units such that $\hbar = t = 1$).

Because the unitary operator implementing the quantum walk is invariant under translations by a discrete number of lattice sites, we expect the effective Hamiltonian to respect the same symmetry. So, if we define the quasimomentum basis $\{|k\rangle\}$ via the relation

$$|k\rangle = \frac{1}{\sqrt{2\pi}} \sum_x e^{-ikx} |x\rangle , \tag{4.3}$$

then $H_{\text{eff}}(\theta)$ should be block-diagonal in this basis. Note that the Brillouin zone here spans the interval $[-\pi, \pi]$, as $|k\rangle = |k + 2\pi\rangle$. Thus, the most general Hamiltonian which respects discrete translation symmetry has the following form:

$$H_{\text{eff}}(\theta) = \int_{-\pi}^{\pi} dk \; \hat{U}_\theta(k) \otimes |k\rangle \langle k| , \tag{4.4}$$

where $\hat{U}_k(\theta)$ is a general 2×2 Hamiltonian.

For a spin-1/2 system, the Pauli matrices, which we repeat below, form a basis for the space of Hermitian matrices:

$$\sigma_0 = I = \begin{pmatrix} 1 & 0 \\ 0 & 1 \end{pmatrix} \tag{4.5}$$

$$\sigma_1 = \sigma_x = \begin{pmatrix} 0 & 1 \\ 1 & 0 \end{pmatrix} \tag{4.6}$$

$$\sigma_2 = \sigma_y = \begin{pmatrix} 0 & -i \\ i & 0 \end{pmatrix} \tag{4.7}$$

$$\sigma_3 = \sigma_z = \begin{pmatrix} 1 & 0 \\ 0 & -1 \end{pmatrix} \tag{4.8}$$

Thus a general spin-1/2 Hamiltonian can be written

$$H = n_0\sigma_0 + \epsilon(n_x\sigma_x + n_y\sigma_y + n_z\sigma_z) \equiv n_0 + \epsilon\vec{n} \cdot \vec{\sigma}, \tag{4.9}$$

where we enforce unit normalization of the vector $\vec{n} \equiv (n_x, n_y, n_z)$, and pull the magnitude into the value ϵ. So, the quantum walk effective Hamiltonian takes the form

$$H_{\text{eff}}(\theta) = \int_{-\pi}^{\pi} dk \ [n_{0,\theta}(k)\sigma_0 + \epsilon(k)(n_{x,\theta}(k)\sigma_x + n_{y,\theta}(k)\sigma_y + n_{z,\theta}(k)\sigma_z)] \otimes |k\rangle \langle k| , \quad (4.10)$$

It thus remains to find the functions $n_{0,\theta}(k)$, $n_{x,\theta}(k)$, $n_{y,\theta}(k)$, and $n_{z,\theta}(k)$ such that the resulting effective Hamiltonian satisfies eq. 4.2. A straightforward but tedious calculation shows that $n_{0,\theta}(k) = 0$, and the expressions for the other coefficients are:

$$\cos(\epsilon(k)) = \cos(\theta/2)\cos(k) \quad (4.11)$$

$$n_{x,\theta}(k) = \frac{\sin(\theta/2)\sin(k)}{\sin(\epsilon(k))} \quad (4.12)$$

$$n_{y,\theta}(k) = \frac{\sin(\theta/2)\cos(k)}{\sin(\epsilon(k))} \quad (4.13)$$

$$n_{z,\theta}(k) = -\frac{\cos(\theta/2)\sin(k)}{\sin(\epsilon(k))} \quad (4.14)$$

We interpret $\epsilon(k)$ as a bandstructure, analogous to the energy bands in solids. The unit vector $\vec{n}$ points (on the Bloch sphere) in the direction of the spin eigenstate corresponding to the spatial $|k\rangle$ mode. One difference between $\epsilon(k)$ and a true bandstructure should be noted for completeness, though it doesn't matter much for the work in this thesis: because the effective Hamiltonian is only defined via the unitary it generates stroboscopically, the energy $\epsilon(k)$ is only defined up to additions of 2π, and is thus more properly known as a quasienergy.

Finally, we can show the topological feature of the quantum walk. Notice that, for a given value of θ, the entire suite of vectors $\vec{n}_\theta(k)$ as k varies across the Brillouin zone is perpendicular to the vector $\vec{A} \equiv (\cos(\theta/2), 0, \sin(\theta/2))$. This set of vectors is constrained to lie in a great circle of the Bloch sphere. As k traverses the Brillouin zone, the number of times which $\vec{n}_\theta(k)$ winds around the great circle is thus constrained to be an integer, and is known as the *winding number*, the *topological invariant* of the walk.

As one can calculate, for the single-step quantum walk, regardless of the value of θ, the vector $\vec{n}_\theta(k)$ winds around the Bloch sphere exactly once. That is, the phase diagram of the single-step quantum walk features only a single topological phase. In what follows, we will introduce the *split-step* quantum walk, which, depending on its parameters, exhibits two phases: one with winding number unity, and another with winding number zero. Before that, however, we must make a number of clarifications.

First, we have not described the significance of the winding number. In condensed-matter systems, a boundary between two regions with different topological invariants hosts bound states, or *edge modes*. These edge modes are localized to the interface between the two different topological phases. Crucially, the existence of the edge modes is robust to disorder in the system—they are said to be *topologically protected*. Loosely speaking, in this context the robustness to disorder comes about because the winding number is a global property

of the system, i.e. it depends on the behavior of $\vec{n}$ across the entire Brillouin zone. The relationship between topological invariants, a property of bulk systems, and protected edge modes, which are a property of the boundary, is known as the *bulk-boundary correspondence*.

Second, the winding number we have defined is, strictly speaking, not the topological invariant of the quantum walk itself, but rather the topological invariant of the underlying effective Hamiltonian. To properly characterize the topological phase of the quantum walk itself, we must analyze the walk protocol in different *time frames*. For the purposes of this thesis, we need not worry about this distinction, as long as we keep in mind that we are characterizing the topological invariant of an effective Hamiltonian *using* quantum walks as a tool. It is certainly possible to use our protocol to characterize the topological invariant of the quantum walk itself, but this is not what we have done here[2]. For a nice discussion of the true bulk-boundary correspondence for the quantum walks themselves, including the notion of time frames, see [5].

Third, we should emphasize that the discreteness of the winding number arose from the fact that it was constrained to lie in a particular great circle of the Bloch sphere. Stated differently, there is no way to continuously deform a path with unit winding number into a path with zero winding number without leaving the allowed great circle. This constraint is not a coincidence, but in fact arises due to a particular symmetry of the walk, known as *chiral symmetry*. This symmetry is defined by the operator Γ, where

$$\Gamma = e^{-i\pi\vec{A}\cdot\vec{\sigma}/2} \tag{4.15}$$

As can easily be checked, conjugation of H_{eff} by Γ takes H_{eff} to $-H_{\text{eff}}$. What is the physical significance of this symmetry? Surprisingly, it is the analogue of *sublattice symmetry* in solid-state systems [31]. Imagine a system like graphene, which has two sublattices, usually labeled **A** and **B**. In graphene, the tight-binding Hamiltonian only allows tunneling from sublattice **A** to sublattice **B** and vice versa; there is no amplitude for directly tunneling from $\mathbf{A} \to \mathbf{A}$ or $\mathbf{B} \to \mathbf{B}$. In the same way, for quantum walks with chiral symmetry, there is no amplitude for a spin-state along the vector $\vec{A}$ to tunnel directly to $\vec{A}$, but only to $-\vec{A}$. This is another way to state the fact that $\vec{n}_\theta(k)$ is always perpendicular to $\vec{A}$.

With these clarifications out of the way, let us discuss the split-step quantum walk and show that it supports two topologically distinct phases. In the split-step quantum walk, the spin-dependent translation of the single-step quantum walk is split up into two separate spin-dependent translations: one which shifts the spin-up component of the wavefunction to the right while leaving the spin-down component untouched, and another which shifts the spin-down component of the wavefunction to the left while leaving the spin-up component untouched. We denote these operators as $\hat{T}_\uparrow$ and $\hat{T}_\downarrow$, defined by

$$\hat{T}_\uparrow = \sum_x |x+1\rangle\langle x| \otimes |\uparrow\rangle\langle\uparrow| + |x\rangle\langle x| \otimes |\downarrow\rangle\langle\downarrow|, \tag{4.16}$$

$$\hat{T}_\downarrow = \sum_x |x\rangle\langle x| \otimes |\uparrow\rangle\langle\uparrow| + |x-1\rangle\langle x| \otimes |\downarrow\rangle\langle\downarrow|, \tag{4.17}$$

[2]The reason for this omission is simple: when we came up with this experiment, we were not aware of this fact!

In terms of these operators, the split step walk unitary is given by

$$U_{\mathrm{SS}}\left(\theta_1,\theta_2\right)=T_{\downarrow}R_y\left(\theta_2\right)T_{\uparrow}R_y\left(\theta_1\right) \tag{4.18}$$

That is, in the split-step quantum walk, we 'toss the coin' once by an angle θ_1, shift the spin-up components of the state, 'toss the coin' again by an angle θ_2, and shift the spin-down component of the state. While a single angle θ defined the single-step quantum walk, the space of split-step quantum walks is two-dimensional, parameterized by θ_1 and θ_2.

As in the single-step walk, one can check that the split-step walk protocol also features a chiral symmetry, with the vector $\vec{A}=(\cos(\theta_1/2),0,\sin(\theta_1/2))$ always perpendicular to the great circle containing the spin eigenstates. Again the effective Hamiltonian respects translation invariance and has the form

$$H_{\mathrm{eff}}(\theta)=\int_{-\pi}^{\pi}dk\;\epsilon_{\theta_1,\theta_2}(k)\;\vec{n}(\theta_1,\theta_2)\cdot\vec{\sigma}\otimes|k\rangle\langle k|\,. \tag{4.19}$$

Explicitly,

$$\begin{aligned}
\cos\epsilon_{\theta_1,\theta_2}(k) &= \cos(\theta_2/2)\cos(\theta_1/2)\cos k-\sin(\theta_1/2)\sin(\theta_2/2) && (4.20)\\
n_x(k) &= \frac{\cos(\theta_2/2)\sin(\theta_1/2)\sin k}{\sin\epsilon_{\theta_1,\theta_2}(k)} && (4.21)\\
n_y(k) &= \frac{\sin(\theta_2/2)\cos(\theta_1/2)+\cos(\theta_2/2)\sin(\theta_1/2)\cos k}{\sin\epsilon_{\theta_1,\theta_2}(k)} && (4.22)\\
n_z(k) &= \frac{-\cos(\theta_2/2)\cos(\theta_1/2)\sin k}{\sin\epsilon_{\theta_1,\theta_2}(k)} && (4.23)
\end{aligned}$$

With some tedious algebra,[3] one can see that depending on the values of θ_1 and θ_2, the vector $\vec{n}$ either wraps around the great circle once or not at all.

They key takeaway from this background section is that the topological invariant of a quantum walk (in one dimension) is given by a winding number. The number of times, W, which the Bloch vector $n(\hat{k})$ winds around the origin as k varies from $[-\pi,\pi]$ defines the topological invariant of the walk [31]. Depending on $\{\theta_1,\,\theta_2\}$, the split-step quantum walk mimics motion either in a trivial band with winding number zero or a topological band with winding number unity.

Having established this background, we now describe our proposed method for measuring the topological invariant of the quantum walk.

4.2 Measuring the winding number

Imagine adiabatically deforming the quantum walk Hamiltonian in a way that translates it across the Brillouin zone by one period. By the adiabatic theorem, whatever the initial state

[3] To check for yourself, rotate the vectors such that the vector $\vec{A}$ is mapped to one of the coordinate axes.

of the system was, the unitary evolution induced by this adiabatic evolution will return the system to its initial state modulo a global phase, known as the Berry phase. For a spin-1/2 system, it is known that the Berry phase corresponding to evolution on a closed path on the Bloch sphere is given by half the subtended solid angle of the enclosed surface. Thus, the Berry phase directly encodes the winding number of the quantum walk: if the vector $n(\hat{k})$ winds around the origin a single time as k sweeps through the Brillouin zone, the corresponding Berry phase will be half of 2π, or π; while, if the vector $n(\hat{k})$ makes zero revolutions during this evolution, the corresponding Berry phase will be zero. Thus, we can write that ϕ_{geo}, the Berry (geometric) phase, is given by $\phi_{geo} = \pi W$, where W is the winding number.

The Berry phase gives us a measurable quantity which distinguishes the two topological phases of the split-step quantum walk. It is this correspondence between the Berry phase and the winding number which we hope to exploit in order to measure the underlying topological invariant. But how to measure the Berry phase in a quantum walk?

First let us answer the question of how to imprint the Berry phase on the state of the walking system. Imagine for a moment that instead of instead of stroboscopic evolution simulating static Hamiltonian evolution, we had a true static system described by the quantum walk's effective Hamiltonian. If we wanted to make the system acquire a Berry phase, we would simply do the adiabatic deformation described two paragraphs above: slowly translate the Hamiltonian in momentum space until it shifts by a single period. That is, if the original hamiltonian is given by

$$H_{\text{eff}} = \epsilon_{\theta_1,\theta_2}(\hat{k})\mathbf{n}_{\theta_1,\theta_2}(\hat{k}) \cdot \sigma, \tag{4.24}$$

then we would make a time-dependent Hamiltonian given by shifting $\hat{k} \to \hat{k} + \alpha t$, where t is time and α is the rate of dragging the Hamiltonian. The dynamics resulting from this sort of deformation have been studied extensively in solid-state and cold atomic systems, and are known as Bloch oscillations.

Since we do not have such a static system, we can instead simulate the deformation of this Hamiltonian, in what we call digital Bloch oscillations. To do that, we make the quantum walk time-dependent: that is, instead of applying the same unitary at each step of the walk, we change the unitary we apply at each step such that the effective Hamiltonian moves along in k-space. Specifically, the modified m^{th} step unitary is

$$U_{\text{SS}}^{(m)}(\theta_1, \theta_2) = T_{\downarrow} R_z(-m\phi) R_y(\theta_2)\, T_{\uparrow} R_z(-m\phi) R_y(\theta_1), \tag{4.25}$$

where $R_z(-m\phi) = e^{i\sigma_z m\phi/2}$ and $\phi = 2\pi/N$ for $N \in Z$. As the above equation shows, the way we have modified the unitary is to insert a σ_z rotation of the walker state before each spin-dependent translation. To see that this implements the k-space translation we were after, note that $T_{\uparrow} R_z(-m\phi) = e^{im\phi/2} e^{i(\hat{k}+m\phi)(\sigma_z-1)/2}$ and $T_{\downarrow} R_z(-m\phi) = e^{-im\phi/2} e^{i(\hat{k}+m\phi)(\sigma_z+1)/2}$, so the additional z-rotations simply shift the original quasi-momentum by a step-dependent amount and result in a modified effective Hamiltonian,

$$\hat{H}_{\text{eff}}^{(m)} = \epsilon_{\theta_1,\theta_2}(\hat{k} + m\phi)\mathbf{n}_{\theta_1,\theta_2}(\hat{k} + m\phi) \cdot \sigma. \tag{4.26}$$

In the limit $\phi \ll 1$, this shift defines an adiabatic translation of momentum space, where the quantum walker traverses the full Brillouin zone in precisely N steps.

Let us precisely study the dynamics of this Bloch-oscillating quantum walk, to show that it indeed causes the system state to pick up a Berry phase. To do this, we map the discrete evolution associated with the series of step-dependent unitaries, $U_{\rm SS}^{(m)}$, to continuous evolution under a time-dependent Schrödinger equation: $i\partial_t|\psi\rangle = H_{\rm eff}(\hat{k}+\Delta k(t))|\psi\rangle$, where $H_{\rm eff}(\hat{k}+\Delta k(t))$ captures the step-dependent effective Hamiltonian via $\Delta k(t) = \phi\sum_m \Theta(t-m)$, where Θ is the Heaviside step function. Note that this is close to the ideal dynamics we had wanted when considering the static Hamiltonian case, except that the Hamiltonian in this case is piecewise constant.

The analogy to Bloch oscillations is best captured by moving into a non-uniformly accelerating frame via the transformation, $U_{\Delta k(t)} = e^{i\hat{x}\Delta k(t)}$, wherein the state, $|\tilde{\psi}\rangle = U^\dagger_{\Delta k(t)}|\psi\rangle$ satisfies

$$i\partial_t|\tilde{\psi}\rangle = \left(H_{\rm eff}(\hat{k}) + \hat{x}\phi\sum_m \delta(t-m)\right)|\tilde{\psi}\rangle\,. \tag{4.27}$$

The above time-evolution mirrors that of a particle on a stationary lattice receiving periodic kicks of magnitude ϕ and the resulting dynamics resemble Bloch oscillations.

To see this, let us consider an initial state $|\tilde{\psi}(0)\rangle = |k\rangle\otimes|\mathbf{n}_k^+\rangle$, where $|\mathbf{n}_k^+\rangle$ and $|\mathbf{n}_k^-\rangle$ are the spinor eigenstates (at momentum k) of the upper and lower bands, respectively. For $\phi \ll 1$, the adiabatic theorem allows one to explicitly solve Eq. (4) (see below),

$$|\tilde{\psi}(t)\rangle = e^{i\phi_{\rm dyn,\pm}}e^{i\phi_{\rm geo,\pm}}|k+m\phi\rangle|\mathbf{n}^\pm_{k+m\phi}\rangle\,. \tag{4.28}$$

The momentum and spinor eigenstates simply follow their adiabats while the overall wavefunction acquires both a dynamical and geometric phase,

$$\begin{aligned}\phi_{\rm dyn,\pm} &= \pm\sum_{m\geq 0}\epsilon(k+m\phi)\\ \phi_{\rm geo,\pm} &= i\phi\sum_{m\geq 0}\langle\mathbf{n}^\pm_{k+m\phi}|\partial_k\mathbf{n}^\pm_{k+m\phi}\rangle\,.\end{aligned} \tag{4.29}$$

Since $|k+2\pi\rangle|\mathbf{n}^\pm_{k+2\pi}\rangle = |k\rangle|\mathbf{n}^\pm_k\rangle$, $|\tilde{\psi}(m)\rangle$ exhibits a recurrence to its initial state—up to a global phase—whenever m/N is an integer [9, 12]; this is precisely analogous to Bloch oscillations, in which Bloch waves recover their initial momentum upon any full traversal of the Brillouin zone.

This recurrence forms the basis of our protocol to measure topological invariants in quantum walks. By performing an interference measurement (e.g. Ramsey spectroscopy) between the refocused wavefunction, $|\tilde{\psi}(m)\rangle$, and a reference state, one can directly extract the overall global phase $\phi_T = \phi_{\rm dyn}+\phi_{\rm geo}$. As will be shown below, it is possible to disentangle the dynamical and geometric contributions to ϕ_T by simply varying the overall step number. In this way, one can extract $\phi_{\rm geo}$, thereby directly measuring the topological winding number.

Explicit solution of the digital Bloch oscillations

Here we take a break from the main story to provide an explicit derivation of the equations (4.29) above. The reader who is willing to take these on faith can simply skip this section.

In the accelerating frame, the Schrödinger equation transforms into $i\partial_t |\tilde{\psi}\rangle = (\tilde{H} - iU^\dagger_{\Delta k(t)}\partial_t U_{\Delta k(t)})|\tilde{\psi}\rangle$, where $\tilde{H} = U^\dagger_{\Delta k(t)} H(t) U_{\Delta k(t)} = H_{\text{eff}}(\hat{k})$. Inserting the time-dependence of $\Delta k(t)$ yields:

$$i\partial_t |\tilde{\psi}\rangle = \Big(H_{\text{eff}}(\hat{k}) + \hat{x}(\partial_t \Delta k)\Big)|\tilde{\psi}\rangle\,. \tag{4.30}$$

In the non-accelerating lab frame, an initial plane-wave state $|k\rangle$ is stationary. In the accelerating frame, plane wave states evolve through the Brillouin zone: $|k\rangle \to |k - \Delta k\rangle$. Thus, one can consider a (completely general) ansatz for $|\tilde{\psi}\rangle$:

$$|\tilde{\psi}\rangle = \frac{1}{2\pi}\int_{\text{BZ}} dk\ \ |k + \Delta k(t)\rangle \left(c_k(t)\,|\mathbf{n}^+_{k+\Delta k(t)}\rangle + d_k(t)\,|\mathbf{n}^-_{k+\Delta k(t)}\rangle\right). \tag{4.31}$$

To solve for $c_k(t)$ and $d_k(t)$, we start by evaluating the LHS of eq. (4.30) with the above ansatz:

$$\begin{aligned}
i\partial_t |\tilde{\psi}\rangle &= \frac{i}{2\pi}\int_{\text{BZ}} dk\ \partial_t \left[|k + \Delta k(t)\rangle \left(c_k(t)\,|\mathbf{n}^+_{k+\Delta k(t)}\rangle + d_k(t)\,|\mathbf{n}^-_{k+\Delta k(t)}\rangle\right)\right] \\
&= \frac{i}{2\pi}\int_{\text{BZ}} dk\ \ |k + \Delta k(t)\rangle \left[(\partial_t c_k(t))\,|\mathbf{n}^+_{k+\Delta k(t)}\rangle + (\partial_t d_k(t))\,|\mathbf{n}^-_{k+\Delta k(t)}\rangle\right] \\
&\quad + \frac{i}{2\pi}\int_{\text{BZ}} dk\ \ |k + \Delta k(t)\rangle \left[c_k(t)\partial_t\,|\mathbf{n}^+_{k+\Delta k(t)}\rangle + d_k(t)\partial_t\,|\mathbf{n}^-_{k+\Delta k(t)}\rangle\right] \\
&\quad + \frac{i}{2\pi}\int_{\text{BZ}} dk\ \ (\partial_t\,|k + \Delta k(t)\rangle) \left[c_k(t)\,|\mathbf{n}^+_{k+\Delta k(t)}\rangle + d_k(t)\,|\mathbf{n}^-_{k+\Delta k(t)}\rangle\right].
\end{aligned}$$

The final term in the above expression can be rewritten as:

$$\partial_t\,|k + \Delta k(t)\rangle = (\partial_t \Delta k)\partial_k\,|k + \Delta k(t)\rangle = (\partial_t \Delta k) \tag{4.32}$$

$$\partial_k \left(\frac{1}{\sqrt{2\pi}}\sum_x e^{-ikx}\,|x\rangle\right) = (\partial_t \Delta k)\,(-i\hat{x}\,|k + \Delta k(t)\rangle)\,. \tag{4.33}$$

We can thus simplify the expression for the LHS of eq. (4.30):

$$\begin{aligned}
i\partial_t |\tilde{\psi}\rangle &= \frac{i}{2\pi}\int_{\text{BZ}} dk\ \ |k + \Delta k(t)\rangle \left[(\partial_t c_k(t))\,|\mathbf{n}^+_{k+\Delta k(t)}\rangle + (\partial_t d_k(t))\,|\mathbf{n}^-_{k+\Delta k(t)}\rangle\right] \\
&+ \frac{i}{2\pi}\int_{\text{BZ}} dk\ \ |k + \Delta k(t)\rangle \left[c_k(t)\partial_t\,|\mathbf{n}^+_{k+\Delta k(t)}\rangle + d_k(t)\partial_t\,|\mathbf{n}^-_{k+\Delta k(t)}\rangle\right] + \hat{x}(\partial_t \Delta k)\,|\tilde{\psi}\rangle
\end{aligned}$$

Inspection reveals that the term $\hat{x}(\partial_t \Delta k)\,|\tilde{\psi}\rangle$ appears on both the LHS and RHS of the Schrödinger equation, so we can cancel this term, giving

$$\begin{aligned}
&\frac{i}{2\pi}\int_{\text{BZ}} dk\ \ |k + \Delta k(t)\rangle \left[(\partial_t c_k(t))\,|\mathbf{n}^+_{k+\Delta k(t)}\rangle + (\partial_t d_k(t))\,|\mathbf{n}^-_{k+\Delta k(t)}\rangle\right] \\
&+ \frac{i}{2\pi}\int_{\text{BZ}} dk\ \ |k + \Delta k(t)\rangle \left[c_k(t)\partial_t\,|\mathbf{n}^+_{k+\Delta k(t)}\rangle + d_k(t)\partial_t\,|\mathbf{n}^-_{k+\Delta k(t)}\rangle\right] = H_{\text{eff}}(\hat{k})\,|\tilde{\psi}\rangle\,.
\end{aligned}$$

At this point, all of the plane-wave states $|k\rangle$ with differing momenta are uncoupled. Projecting onto a particular plane wave state:

$$(i\partial_t c_k(t))\,|\mathbf{n}^+_{k+\Delta k(t)}\rangle + (i\partial_t d_k(t))\,|\mathbf{n}^-_{k+\Delta k(t)}\rangle = H_{\text{eff}}(k)\,|\tilde{\psi}\rangle - ic_k(t)\partial_t\,|\mathbf{n}^+_{k+\Delta k(t)}\rangle - id_k(t)\partial_t\,|\mathbf{n}^-_{k+\Delta k(t)}\rangle\,. \tag{4.34}$$

Further projecting onto the states $|\mathbf{n}^\pm_{k+\Delta k(t)}\rangle$ gives two coupled equations for c_k and d_k:

$$\begin{aligned}
i\dot{c}_k(t) = &\quad \epsilon(k+\Delta k)c_k(t) - i(\partial_t\Delta k)\,\langle \mathbf{n}^+_{k+\Delta k(t)}|\partial_k|\mathbf{n}^+_{k+\Delta k(t)}\rangle\, c_k(t)\\
&- i(\partial_t\Delta k)\,\langle \mathbf{n}^+_{k+\Delta k(t)}|\partial_k|\mathbf{n}^-_{k+\Delta k(t)}\rangle\, d_k(t)\\
i\dot{d}_k(t) = &- \epsilon(k+\Delta k)d_k(t) - i(\partial_t\Delta k)\,\langle \mathbf{n}^-_{k+\Delta k(t)}|\partial_k|\mathbf{n}^-_{k+\Delta k(t)}\rangle\, d_k(t)\\
&- i(\partial_t\Delta k)\,\langle \mathbf{n}^-_{k+\Delta k(t)}|\partial_k|\mathbf{n}^+_{k+\Delta k(t)}\rangle\, c_k(t).
\end{aligned}$$

The three terms on the RHS of eqs. (4.35,4.35) correspond to, respectively, the dynamical phase, the Berry phase, and the non-adiabatic mixing between bands. We neglect the mixing term in our initial analysis (see the next subsection for details), which decouples the equations for $c_k(t)$ and $d_k(t)$, yielding solutions

$$c_k(t) = \exp\Big[\int_0^t -i\epsilon(k+\Delta k(\tau)) - (\partial_\tau\Delta k)\,\langle \mathbf{n}^+_{k+\Delta k(\tau)}|\partial_k|\mathbf{n}^+_{k+\Delta k(\tau)}\rangle\, d\tau\Big]c_k(0) \tag{4.35}$$

$$d_k(t) = \exp\Big[\int_0^t i\epsilon(k+\Delta k(\tau)) - (\partial_\tau\Delta k)\,\langle \mathbf{n}^-_{k+\Delta k(\tau)}|\partial_k|\mathbf{n}^-_{k+\Delta k(\tau)}\rangle\, d\tau\Big]d_k(0). \tag{4.36}$$

Performing the integration gives the dynamics as a function of the step number m:

$$c_k(m) = \exp\Big[\; -i\textstyle\sum_{m\geq 0}\epsilon(k+m\phi) - \phi\sum_{m>0}\langle \mathbf{n}^+_{k+m\phi}|\partial_k|\mathbf{n}^+_{k+m\phi}\rangle\,\Big]c_k(0) \tag{4.37}$$

$$d_k(m) = \exp\Big[\; i\textstyle\sum_{m\geq 0}\epsilon(k+m\phi) - \phi\sum_{m>0}\langle \mathbf{n}^-_{k+m\phi}|\partial_k|\mathbf{n}^-_{k+m\phi}\rangle\,\Big]d_k(0). \tag{4.38}$$

The first sum in the exponential corresponds to the discretized dynamical phase $\phi^\Delta_{\text{dyn},\pm}$, while the second corresponds to the discretized Berry phase $\phi^\Delta_{\text{Berry},\pm}$:

$$\phi^\Delta_{\text{dyn},\pm} = \pm\sum_{m\geq 0}\epsilon(k+m\phi) \tag{4.39}$$

$$\phi^\Delta_{\text{Berry},\pm} = i\phi\sum_{m\geq 0}\langle \mathbf{n}^\pm_{k+m\phi}|\partial_k|\mathbf{n}^\pm_{k+m\phi}\rangle\,. \tag{4.40}$$

When the number of steps in the walk is such that the entire Brillouin zone is traversed, and in the limit of small ϕ (or equivalently, large N), the discretized Berry phase approaches the continuous Berry phase $i\oint\langle \mathbf{n}^\pm_k|\partial_k\mathbf{n}^\pm_k\rangle\,dk$. The dynamical phase can also be approximated in this limit as $\phi^\Delta_{\text{dyn},\pm}\to\pm N/(2\pi)\oint\epsilon(k)\;dk$.

Calculation of the non-adiabatic (Landau-Zener) transition probability

Here, we derive an approximate formula for the interband transitions introduced by our time-dependent quantum walk protocol. Again, the reader willing to take the equations above on faith can skip this section.

We again solve the Schrödinger equations for the $c_k(t)$ and $d_k(t)$ coefficients, this time keeping the final non-adiabatic terms. In this calculation we estimate the contribution of interband mixing while staying close to the adiabatic limit. To do this, we consider the situation in which the state is initialized in a single $|k\rangle$ state and in the lower band so that d_k is always close to unity and $c_k \ll 1$. Instead of solving for $|c_k|^2$ directly, we solve for $c_k^* d_k$, since approximately $|c_k^* d_k|^2 \approx |c_k|^2$. Equations 4.35 and 4.35 can be combined to read

$$i\partial_t(c_k^* d_k) = -2\epsilon(k+\Delta k)c_k^* d_k - i\partial_t \Delta k \, \langle \mathbf{n}^-_{k+\Delta k}|\partial_k|\mathbf{n}^+_{k+\Delta k}\rangle \, (|c_k|^2 - |d_k|^2), \tag{4.41}$$

which, by enforcing normalization ($|c_k|^2 + |d_k|^2 = 1$), transforms into

$$i\partial_t(c_k^* d_k) = -2\epsilon(k+\Delta k)c_k^* d_k - i\partial_t \Delta k \, \langle \mathbf{n}^-_{k+\Delta k}|\partial_k|\mathbf{n}^+_{k+\Delta k}\rangle \, (2|c_k|^2 - 1). \tag{4.42}$$

Assuming that the band mixing is small, so that $|c_k^* d_k|^2 \ll 1$, this equation becomes

$$\partial_t(c_k^* d_k e^{-2i\int_0^t d\tau \ \epsilon(k+\Delta k)}) \approx \partial_t \Delta k \, \langle \mathbf{n}^-_{k+\Delta k}|\partial_k|\mathbf{n}^+_{k+\Delta k}\rangle \, e^{-2i\int_0^t d\tau \epsilon(k+\Delta k)}, \tag{4.43}$$

which can be directly integrated to yield

$$|c_k^* d_k|(t) \approx \left| \int_0^t d\tau \ (\partial_\tau \Delta k) \, \langle \mathbf{n}^-_{k+\Delta k}|\partial_k|\mathbf{n}^+_{k+\Delta k}\rangle \, e^{-2i\int_0^\tau d\tau' \epsilon(k+\Delta k)} \right|. \tag{4.44}$$

Inserting explicitly the time-dependence of $\Delta k(t)$—composed of step functions—gives δ-functions in the integrand, transforming the integral into a discrete sum. Here we specialize to a full traversal of the Brillouin zone (in N steps), so

$$|c_k^* d_k| \approx \phi \left| \sum_{m=1}^{N} \langle \mathbf{n}^-_{k+n\phi}|\partial_k|\mathbf{n}^+_{k+m\phi}\rangle \, e^{-2i\sum_0^m \epsilon(k+p\phi)} \right|. \tag{4.45}$$

Thus, the approximate probability for interband transitions is given by

$$P_{\uparrow\downarrow} \approx \phi^2 \left| \sum_{m=1}^{N} \langle \mathbf{n}^-_{k+m\phi}|\partial_k|\mathbf{n}^+_{k+m\phi}\rangle \, e^{-2i\sum_0^m \epsilon(k+p\phi)} \right|^2. \tag{4.46}$$

Dynamical phases and refocusing

We pick up the main story again, from the calculation of the dynamic and geometric phases accrued by the Bloch-oscillating quantum walk. Remember that we had shown that for initial momentum or spinor eigenstates, the Bloch-oscillating walk causes a recurrence of the initial state. Although recurrence always occurs for initial momentum/spinor eigenstates (e.g. $|\tilde{\psi}(0)\rangle = |k\rangle \otimes |\mathbf{n}_k^\pm\rangle$), quantum walks are typically initialized with the particle localized at a single initial site. As such states consist of superpositions of eigenstates in both the upper and lower energy bands,

$$|\tilde{\psi}(0)\rangle = \sum_k c_k \, |k\rangle \, |\mathbf{n}_k^+\rangle + d_k \, |k\rangle \, |\mathbf{n}_k^-\rangle \, , \tag{4.47}$$

their refocusing behavior is significantly more subtle, requiring not only that each constituent eigenstate return to itself, but also that the total accrued phase is identical for all components. While the geometric phase acquired after N steps is πW for all eigenstates, the dynamical phase acquired by states in the upper and lower bands are opposite [Eq. 4.29]. Thus, the final state will generally *not* refocus to the initial state, and the wavefunction instead will remain spread over a number of sites.

Fortunately, one can always ensure near-perfect refocusing (i.e. enforcing a dynamical phase which is arbitrarily close to a multiple of 2π [4]) by first characterizing the fidelity as a function of total step number. In particular, in the limit of large step number, the dynamical phase becomes proportional to N: $\phi_{\text{dyn}} \approx N \times \bar{\epsilon}$, where $\bar{\epsilon} = \int dk\ \epsilon(k)/2\pi$ [5]. The refocusing fidelity, $\mathcal{F} = |\langle\psi_0|\psi_f\rangle|^2$, is then given by

$$\mathcal{F} = \cos^2(N\bar{\epsilon}), \tag{4.48}$$

enabling one to control the refocusing via a choice of N.

To derive the above equation, write $|\psi_0\rangle$ in terms of $|k\rangle$ states: $|\psi_0\rangle = \int dk\ (c_k |k\rangle |\mathbf{n}_k^+\rangle + d_k |k\rangle |\mathbf{n}_k^-\rangle)$, The state after the Bloch-oscillating quantum walk (apart from a global Berry phase which does not impact refocusing fidelity) is given by

$$|\psi_f\rangle = \int dk\ (c_k e^{i\phi_{\text{dyn}}} |k\rangle |\mathbf{n}_k^+\rangle + d_k e^{-i\phi_{\text{dyn}}} |k\rangle |\mathbf{n}_k^-\rangle). \tag{4.49}$$

The refocusing fidelity $|\langle\psi_f|\psi_0\rangle|^2$ is then

$$|\langle\psi_f|\psi_0\rangle|^2 = \left| e^{i\phi_{\text{dyn}}} \left(\int dk\ |c_k|^2 \right) + e^{-i\phi_{\text{dyn}}} \left(\int dk\ |d_k|^2 \right) \right|^2 = \cos^2(\phi_{\text{dyn}}), \tag{4.50}$$

where we have used a specific relation between the inner product of two spinor states and their corresponding Bloch-sphere vectors, namely that $|\langle\psi|\phi\rangle|^2 = (1/4)\,|\vec{n} + \vec{m}|^2$, where $\vec{n}$ and $\vec{m}$ point in the direction of the states ϕ and ψ. Using this relation, one can easily show that (for the specific initial state localized on a single lattice site and in a σ_z eigenstate) the two integrals in eq. (4.50) evaluate to 1/2.

Summary

So far we have shown how to construct a Bloch-oscillating quantum walk from an arbitrary split- or single-step quantum walk. By choosing the number of steps N such that the state of the particle is refocused, one finds that the final wavefunction differs from the initial state by only an imprinted geometric phase, which encodes the topology of the quantum walk. While global phases are generally non-measurable, below we show how this geometric phase can be extracted interferometrically in a system with an additional internal state.

[4] We note that refocusing also occurs for dynamical phases that are an odd multiple of π. In such cases, one simply needs to account for the dynamical phase when calculating the winding number W or double the total number of steps.

[5] This is analogous to continuous-time evolution, where ϕ_{dyn} is directly proportional to the time taken to traverse a path in parameter space.

4.3 Experimental proposal

In the previous sections, we have shown how we can map the winding number of a particular topological quantum walk onto a Berry phase, and how we can modify a static quantum walk to imprint precisely that Berry phase on the state of the walker. To complete the story, we must show how one can measure the Berry phase. Typically, Berry phases are not measurable. But luckily, we can take advantage of the toolbox associated with circuit QED to make a system in which one part of the state undergoes the quantum walk while the other remains stationary. By doing this we convert the geometric phase into a relative phase between the walking and stationary components of the wavefunction, which can then be measured interferometrically. In fact, we do exactly that measurement in the next chapter. Here we give a simplified description of the experiment, in order to complete the theoretical story.

We consider a superconducting transmon qubit [33] coupled to a high-quality-factor electromagnetic cavity and envision the quantum walk to take place in the phase space of the cavity mode [59]. Each lattice site corresponds to a particular coherent state of the cavity and the two logical states of the transmon ($|g\rangle, |e\rangle$) form the internal spin of the walker [64].

Spin rotations $R_y(\theta)$ and $R_z(\phi)$ can be performed using coherent microwave driving, with state-of-the-art pulse shaping techniques enabling single-qubit X and Y Clifford gates with greater than 99.9% fidelity in as little as 20 ns [14]. Spin-dependent translations arise naturally from the dispersive coupling between the qubit and the cavity, $H_{\text{int}} = \hbar(\chi/2)a^\dagger a\sigma_z$ [56]. Here, σ_z is the Pauli z-operator of the transmon qubit, $a^\dagger$ (a) the cavity raising (lowering) operator, and χ the strength of the qubit-cavity dispersive coupling. In combination, the above operations enable the realization of a quantum walk on a circular lattice in cavity phase space . In particular, one initializes the cavity in a coherent state $|\alpha\rangle$, with the qubit in the ground state $|g\rangle$. After applying the desired unitary rotation to the qubit, a waiting period of time t allows the dispersive interaction to naturally implement the spin-dependent translation. Indeed, a coherent state $|\alpha\rangle$ in the cavity frame precesses either clockwise ($|\alpha\rangle|e\rangle \rightarrow |\alpha \exp(i\chi t/2)\rangle|e\rangle$) or counterclockwise ($|\alpha\rangle|g\rangle \rightarrow |\alpha \exp(-i\chi t/2)\rangle|g\rangle$) depending on the qubit state. Choosing t such that $\chi t = 2\pi/L$ defines the L coherent state "lattice sites": $\{|\alpha \exp(i2\pi\ell/L)\rangle, \ell \in [0, L-1]\}$.

These two basic steps (unitary rotation and spin-dependent translation) can then be repeated to realize a Bloch-oscillating quantum walk. Measurement of the quantum walker's spin and position after each step can be performed via full tomography of the cavity-qubit system [61].

To directly probe the topological invariant via the imprinted geometric phase, one must perform interferometry between the refocused wavefunction and a reference state. This is naturally enabled by the proposed cQED architecture, where one can initialize the system in a cavity Schrödinger cat state, corresponding to a coherent superposition, $1/\sqrt{2}(|\alpha\rangle|g\rangle + |0\rangle|f\rangle)$, where $|0\rangle$ is the vacuum state of the cavity and $|f\rangle$ is the second excited state of the qubit. Crucially, the $|0\rangle|f\rangle$ state behaves as a phase reference since it is immune to both the unitary spin rotations and the dispersive coupling. The $|f\rangle$ state in transmon qubits

can exhibit coherence and decay times in excess of 20 μs [49], while the aforementioned pulse-shaping techniques result in off-resonant leakage errors $< 10^{-5}$.

Upon refocusing of the $|\alpha\rangle|g\rangle$ component, the final wavefunction takes the form:

$$|\psi\rangle = 1/\sqrt{2}(e^{i\pi W}|\alpha\rangle|g\rangle + |0\rangle|f\rangle), \tag{4.51}$$

and the topological winding number manifests in the geometric relative phase between the two components. After disentangling the spin and cavity degrees of freedom via number-selective qubit pulses (i.e. $|0\rangle|f\rangle \rightarrow |0\rangle|g\rangle$) [6], one can perform full Wigner tomography of the cavity state. The resulting interference patterns will display fringes whose phase corresponds to πW.

4.4 Conclusion and Future Work

In this chapter, we have described how the simulation platform associated with quantum walks can enable the direct measurement of bulk topological invariants. In particular, by constructing Bloch-oscillating analogues of both split- and single-step quantum walks, we have introduced an interferometric protocol to directly measure the winding number associated with a quantum walks effective band structure. A key feature of such Bloch-oscillating quantum walks is their natural refocusing behavior, whose microscopic origin arises from an interplay between dynamical and geometric phases as well as non-adiabatic transitions. Looking forward, our results can be directly extended to measurements of quantum walk topological invariants in higher dimensions, and provide a bridge toward probing many-body invariants associated with interacting quantum walks.

[6] By using a single local oscillator to perform both excitation into and out of the $|f\rangle$ state, the evolved dynamical phase associated with this state is automatically kept track of and cancelled.

Chapter 5

Observing Topological Invariants: Experiment

This chapter describes the experimental implementation of the theoretical proposal outlined in the previous chapter. As a reminder, the direct measurement of topological invariants in both engineered and naturally occurring quantum materials is a key step in classifying quantum phases of matter. In this chapter, we perform an experiment illustrating how a time-dependent quantum walk can be used to digitally simulate single-particle topological band structures. Our experiment uses a superconducting transmon qubit dispersively coupled to a microwave cavity to implement two classes of split-step quantum walks and directly measure the topological invariant (winding number) associated with each. The measurement relies upon interference between two components of a cavity Schrödinger cat state and the implementation of a digital version of Bloch oscillations. Our scheme can readily be extended to higher dimensions, whereby quantum walk-based simulations might probe topological phases ranging from the quantum spin Hall effect to the Hopf insulator.

This chapter is intended to be self-contained, in that it can be read without having read the previous theory chapter. The reader wishing to understand the basics of the experiment should read this chapter first and can use the previous chapter to fill in details as desired.

5.1 Motivation

Topological phases elude the Landau-Ginzburg paradigm of symmetry-breaking. Unlike conventional phases, they do not exhibit order parameters that can be locally measured. Rather, their distinguishing features are hidden in quantized, non-local topological invariants, which are robust to all local perturbations [40, 23]. While tremendous theoretical progress has been made toward the full classification of topological phases of matter [30, 54], a general experimental platform for the direct measurement of topological invariants is lacking. With this experiment, we demonstrate that time-dependent quantum walks comprise a powerful class of unitary protocols capable of digitally simulating single-particle topological bandstructures

and directly observing the associated non-local invariants.

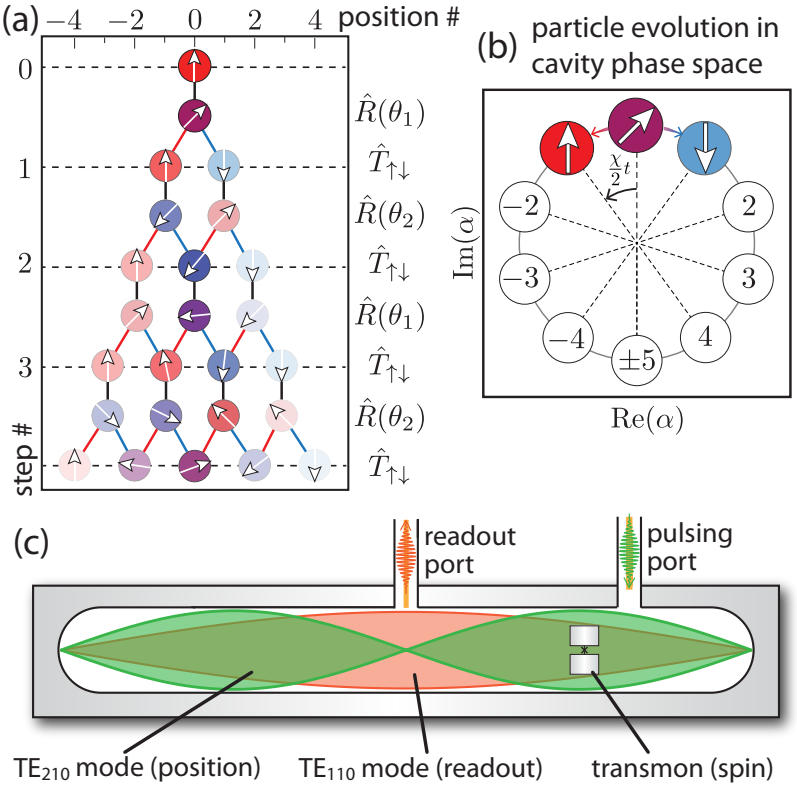

Figure 5.1: **Quantum walk implementation in cavity phase space. a.** Schematic representation of a split-step quantum walk on a line, with rotations $\hat{R}(\theta_1)$ and $\hat{R}(\theta_2)$ and spin-dependent translation $T_{\uparrow\downarrow}$. Red (blue) lines show spin-up (-down) components moving left (right). The opacity of each circle indicates the population on the corresponding lattice site. **b.** Set of ten cavity coherent states on which the walk takes place, in the phase space of the TE_{210} cavity mode. **c.** Cavity resonator and qubit. The fundamental (TE_{110}, orange) mode at $\omega_R = 2\pi \times 6.77$ GHz is used to measure the qubit state. This mode couples strongly ($\kappa = 2\pi \times 600$ kHz $= 1/(260$ ns)) to a 50-ohm transmission line via the readout port at the center of the cavity. The TE_{210} cavity mode (green) at $\omega_C = 2\pi \times 5.2$ GHz is long lived with an inverse lifetime, $\kappa = 2\pi \times 4$ kHz $= 1/(40\ \mu$s). The transmon qubit (coin) has transition frequency $\omega_C = 2\pi \times 5.2$ GHz, relaxation times $T_1 = 40\ \mu$s and $T_2^* = 5.2\ \mu$s, and is dispersively coupled to both cavity modes, with the dispersive shift of the walker mode, $\chi = 2\pi \times 1.61$ MHz.

5.2 Realizing quantum walks in circuit QED

A quantum walk [2, 28, 51, 18, 4, 15] describes the motion of a particle with internal (spin) degrees of freedom moving on a discrete lattice. Much like their classical cousins, quantum walks have stimulated activity across a broad range of disciplines [18, 4, 15]. Formally, the quantum walk is comprised of two unitary operations (see Fig. 5.1A): a *coin toss*, denoted $\hat{R}(\theta)$, which rotates the spin state; and a *spin-dependent translation*, denoted $\hat{T}_{\uparrow\downarrow}$, which translates the particle's position by a single lattice site in a direction determined by the internal spin state. In our circuit quantum electrodynamics implementation of the quantum walk, the particle is encoded as a coherent state of an electromagnetic cavity mode [47] where its position is defined in the cavity's phase space, as shown in figure 5.1B. Its spin degrees of freedom are formed by a superconducting transmon qubit [34] with basis states $\{|\uparrow\rangle, |\downarrow\rangle\}$. To enable the qubit state to control the direction of motion of the coherent state, we realize a strong dispersive coupling between the cavity and qubit,

$$\hat{H}/\hbar = \omega_q \hat{\sigma}_z/2 + \omega_c \hat{a}^\dagger \hat{a} - \chi_{qs} \hat{a}^\dagger \hat{a} \hat{\sigma}_z/2, \tag{5.1}$$

where $\omega_{q,s}$ are the qubit and cavity transition frequencies respectively, $\hat{a}$ ($\hat{a}^\dagger$) is the lowering (raising) operator for the cavity mode, σ_z the Pauli z-matrix for the qubit levels, and χ_{qs} the dispersive interaction strength (see Fig. 5.1C). Dispersive coupling produces a qubit dependent shift in the cavity oscillation frequency. Viewed in the rotating frame of the cavity at ω_c, the dispersive interaction causes the coherent state to move clockwise (counterclockwise) at a rate $\chi_{qs}/2$ through phase space when the qubit is in the $|\uparrow\rangle$ ($|\downarrow\rangle$) state. Thus, free evolution under the dispersive interaction precisely enables the spin-dependent translation needed for the quantum walk [65, 59].

We realize a particular class of quantum algorithm known as the *split-step* quantum walk [32, 31], which alternates two coin tosses (with rotation angles θ_1 and θ_2) between two spin-dependent translations, so that each step of the walk consists of the unitary operation $\hat{U}_W(\theta_1, \theta_2) = \hat{T}_{\uparrow\downarrow}\hat{R}(\theta_2)\hat{T}_{\uparrow\downarrow}\hat{R}(\theta_1)$ (see Fig. 5.1A). The coin toss operations $\hat{R}_x(\theta) = e^{i\theta\hat{\sigma}_x/2}$ are applied via short (7.5 ns) coherent microwave pulses resonant with the qubit transition. By waiting for a time interval $t = 2\pi(10\chi_{qs})^{-1} = 124$ ns between successive coin tosses, we allow the dispersive coupling to naturally implement the spin-dependent translation. This time interval determines the lattice on which the walk takes place; here, it is a circular lattice of ten sites in cavity phase space (Fig. 5.1B).

We begin by performing a pair of topologically distinct split-step quantum walks, the first (topologically trivial) with unitary $\hat{U}_0 = \hat{U}_W(3\pi/4, \pi/4)$, and the second (topologically non-trivial) with $\hat{U}_1 = \hat{U}_W(\pi/4, 3\pi/4)$. To demonstrate the robustness of the winding number, we also implement an additional pair of walks which are continuously connected to $\hat{U}_0$ and $\hat{U}_1$ (e.g. without closing the gap). The experimental sequence is shown in Fig. 5.2A. The cavity mode is initialized ($\mathcal{D}_\beta$) in a coherent state $|\beta\rangle$ with $|\beta|^2 = 8$ photons, after which the walk unitary is repeatedly applied. To directly reconstruct the walker's quantum state on the phase space lattice, we first projectively measure the qubit state and subsequently measure the Q-function of the cavity mode. Figure 5.2B depicts the measured lattice site populations

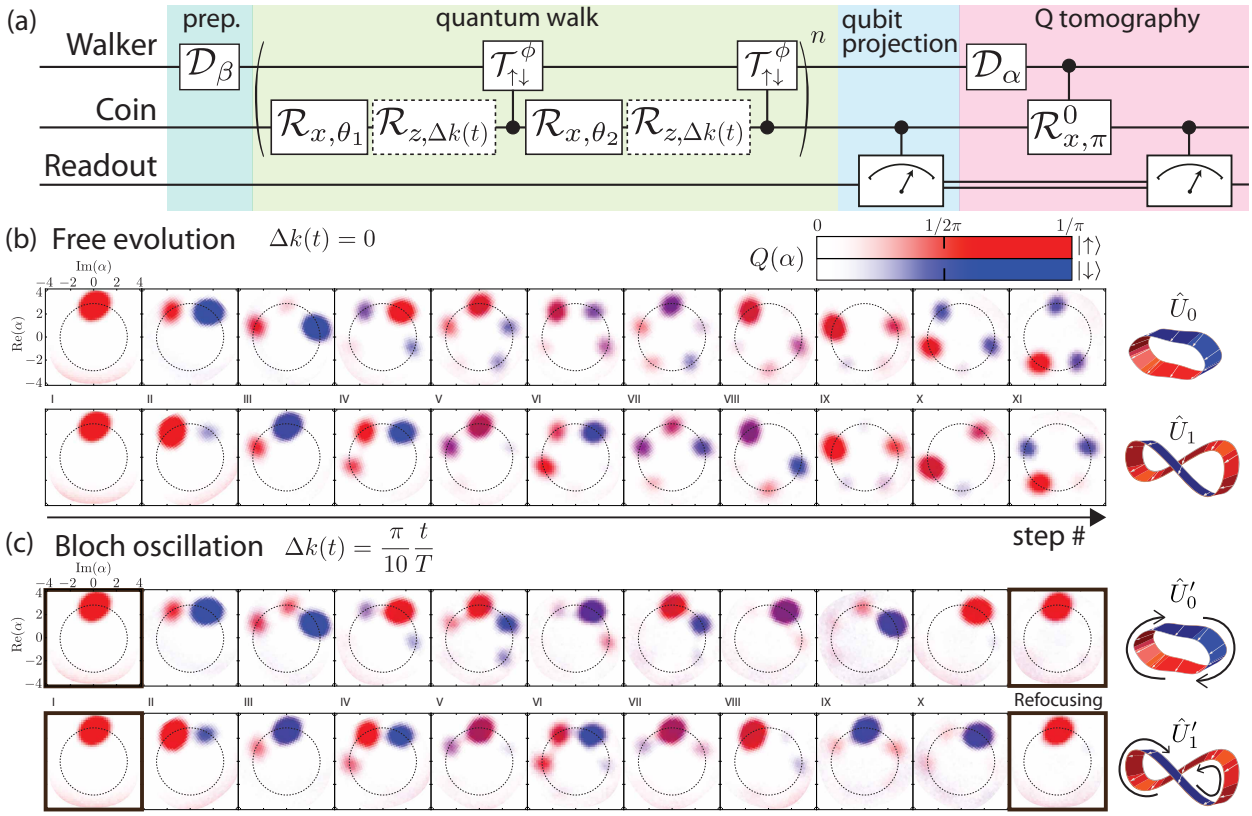

Figure 5.2: **Quantum walk protocol and resulting populations. a.** Protocol used to perform the quantum walk, showing cavity state preparation (blue), quantum walk (green), qubit state measurement (blue), and Q function measurement (pink). The dashed boxes with σ_z gates are performed to implement the Bloch oscillation. **b.** Cavity Q functions after each step of the quantum walk without Bloch oscillations, $\hat{U}_0$ (top strip) and $\hat{U}_1$ (bottom strip). Spin-up (red) and spin-down (blue) Q functions are superimposed. Average fidelity of the populations compared to theoretical predictions is 0.97 and 0.96 for $\hat{U}_0$ and $\hat{U}_1$, respectively. **c.** Cavity Q functions after each step of the refocusing quantum walk with Bloch oscillations. The state refocuses after ten steps, as shown in the final frame for both $\hat{U}_0$ and $\hat{U}_1$. Refocusing fidelities (to the initial state) for $\hat{U}_0$ and $\hat{U}_1$ are 0.83 and 0.87, respectively.

after each step of the walk. We observe the expected ballistic expansion of the coherent state in cavity phase space, consistent with theoretical predictions (population fidelities $> 90\%$).

As the walk unitary, $\hat{U}_W$, directly couples the particle's spin and position degrees of freedom, the resulting dynamics mimic those of spin-orbit interacting materials. More precisely, the unitary quantum walk protocol simulates continuous evolution under an effective spin-orbit Hamiltonian $\hat{H}_W$, which generates the same transformation as a single step of the walk when $\hat{U}_W = e^{-i\hat{H}_W}$. Since the unitary is translation invariant, the effective Hamiltonian exhibits Bloch bands of quasienergy $\pm\epsilon(k)$, where the quasimomentum, k, lies in

the Brillouin zone; figures 5.3A and 5.3B show respectively the bandstructures underlying the walks $\hat{U}_0$ and $\hat{U}_1$. The corresponding eigenstates consist of extended Bloch waves with spin polarization $\pm\vec{n}(k)$ [31]. Depending on symmetry, the bandstructure of such spin-orbit-coupled Hamiltonians can feature quantized topological invariants. In the case of the split-step quantum walk, $\Gamma = e^{-i\pi\vec{A}\cdot\vec{\sigma}/2}$ plays the role of a so-called chiral symmetry [31, 5], with $\Gamma^\dagger\hat{U}_W\Gamma = -\hat{U}_W$. This symmetry constrains the spin polarization vector $\vec{n}(k)$ to lie on a great circle of the Bloch sphere, perpendicular to $\vec{A} = (\cos(\theta_1/2), 0, \sin(\theta_1/2))$ (Fig. 5.3C and D). Thus, the number of times $\vec{n}(k)$ wraps around the origin as k varies through the Brillouin zone—known as the winding or Chern number $\mathcal{W}$—naturally defines the topological invariant [31] of the walk. While the energy spectra of $\hat{U}_0$ and $\hat{U}_1$ are identical, they lie in topologically distinct phases, with $\hat{U}_0$ having zero winding number and $\hat{U}_1$ a winding number of unity. Analogous to the number of twists in a closed ribbon, winding numbers are quantized and robust to local perturbations [40].

The direct measurement of topological invariants in solid-state materials is an outstanding challenge [6, 3, 53], owing to the non-local nature of the order parameter. Our method makes use of a time-dependent modification of the quantum walk which, in the Hamiltonian picture, mimics an adiabatic translation of the underlying bandstructure across the Brillouin zone [8, 21, 38, 13]. The resulting dynamics effectively constitute digital Bloch oscillations, a phenomenon whereby a particle on a lattice subjected to a constant force undergoes oscillations due to the periodicity of the Brillouin zone. In our system, these oscillations manifest as a refocusing of the quantum walker to its initial position, with a Berry phase—a signature of the bandstructure topology (see Fig. 5.3)—imprinted during the evolution. In practice, this refocusing depends on choosing the number of steps in the walk such that the accrued dynamical phase—which has opposite signs in either band and thus impedes refocusing—effectively vanishes. This is described in a later section.

In addition to the dynamical phase, upon traversing the Brillouin zone, the particle's spin winds around the Bloch sphere, encoding its path in the accumulated Berry phase [67],

$$\phi_B = i\int_{\mathrm{BZ}}\langle k, \vec{n}(k)|\partial_k|k, \vec{n}(k)\rangle dk = \pi \times \mathcal{W} \tag{5.2}$$

which thus becomes an observable manifestation of the winding number $\mathcal{W}$—the Hamiltonian's topological invariant. As one cannot directly observe the quantum mechanical phase of a wavefunction, measuring this Berry phase requires an interferometric approach. To this end, we perform the time-dependent walk with the cavity-qubit system initialized in a Schrödinger cat superposition of two coherent-state components: one component undergoes the walk, while the other is unaffected by the unitaries. The Berry phase thus appears as the relative phase between the two components and is observable via direct Wigner tomography.

The additional steps used in performing the time-dependent walks are shown in dashed boxes in Fig. 5.2A. Beginning with either $\hat{U}_0$ or $\hat{U}_1$, we insert rotations by Δk about $\hat{\sigma}_z$ after each coin toss rotation $\hat{R}(\theta_1)$ and $\hat{R}(\theta_2)$. In contrast to the original operations comprising $\hat{U}_0$ and $\hat{U}_1$, the rotation angle Δk varies in time. Since a $\hat{\sigma}_z$ rotation is equivalent to a translation of the underlying Hamiltonian in quasimomentum space, this time-varying rotation angle

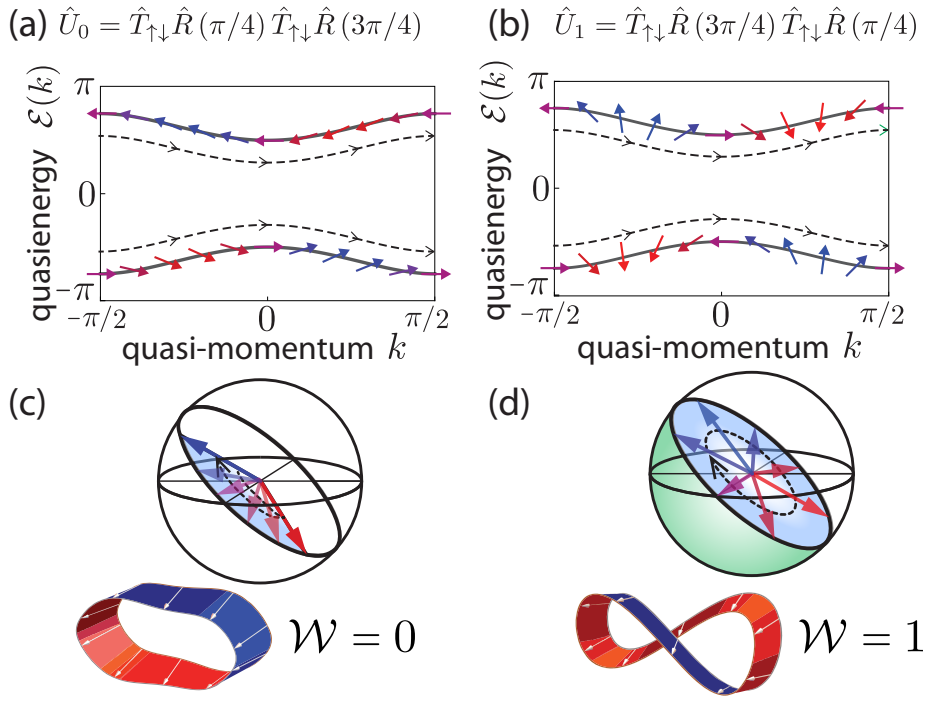

Figure 5.3: **Topological classes of split-step quantum walks** Calculated band structures, quasienergy ϵ versus quasimomentum k, corresponding to the two walks we perform in the experiment, $\hat{U}_0 = \hat{T}_{\uparrow\downarrow}\hat{R}(\pi/4)\hat{T}_{\uparrow\downarrow}\hat{R}(3\pi/4)$ (**a**) and $\hat{U}_1 = \hat{T}_{\uparrow\downarrow}\hat{R}(3\pi/4)\hat{T}_{\uparrow\downarrow}\hat{R}(\pi/4)$ (**b**). Though the energy bands of the two walks are identical, they are topologically distinct, with the topology given by the winding of $\vec{n}(k)$ as k varies through the Brillouin zone, shown in **c** and **d**. In **c**, the trivial case $\hat{U}_0$, $\vec{n}(k)$ does not complete a full revolution around the Bloch sphere, while in the topological case $\hat{U}_1$ **d**, it does perform a full revolution. This also provides a direct connection to the Berry phase, as for a spin-1/2 system the Berry phase is simply half the subtended solid angle of the Bloch sphere path. A schematic representation of the variation of $\vec{n}(k)$ is shown by the ribbons below the Bloch spheres. The arrows on this strips point in the direction of $\vec{n}(k)$. Analogous to the number of twists in closed ribbons, winding numbers are quantized and robust to local perturbations.

implements a digital Bloch oscillation. We choose Δk to vary in steps of $\pi/10$ from 0 to π, traversing the Brillouin zone exactly once.

Populations resulting from the time-dependent walks (with the system initialized in a single coherent state) are shown in Fig. 5.2C. Unlike the ballistic dynamics resulting from the original walks, the Bloch oscillation (traversal of the Brillouin zone) causes the walker wavefunction to refocus [8, 21, 38, 13] to both its initial position and spin state. The intuition underlying this refocusing is that both the dynamical and Berry phase accumulated by each quasimomentum-component of the walker is identical upon full traversal. In practice, we observe refocusing fidelities $> 90\%$, limited by incomplete adiabaticity and experimental

imperfections.

Having verified the refocusing behavior of the time-dependent quantum walks, we initialize the cavity-qubit system in a Schrödinger cat state to measure the accumulated Berry phase. One component of the cat is precisely the initial state of the previous walks, $|\beta, \uparrow\rangle$. The other component is $|0, f\rangle$, where the cavity in its ground (vacuum) state and the transmon in its second excited state [34], $|f\rangle$. Shelving the vacuum component of the cat in the $|f\rangle$ state renders it immune to the coin toss rotations, as the $|f\rangle \leftrightarrow |\downarrow\rangle$ transition is far detuned (225 MHz) from the $|\uparrow\rangle \leftrightarrow |\downarrow\rangle$ transition. Thus, this component of the cat lies dormant during the walk, acting as a phase reference for the observation of the Berry phase.

Our method of preparing the cat, a modification of the protocol introduced in ref. [62], is shown in Fig. 5.4A. With the cat initialized, we perform the time-dependent walk over a full Bloch oscillation, applying the same set of pulses that resulted in the final frames of Fig. 5.2C. After the walking component of the cat refocuses, we disentangle the qubit from the cavity with the operation $|0, f\rangle \rightarrow |0, \uparrow\rangle$. This leaves the oscillator in the state

$$|\psi\rangle = |0\rangle - e^{i\phi_B}|\beta\rangle, \tag{5.3}$$

where ϕ_B is the Berry phase.

While Q tomography lends itself well to measuring coherent state occupations, coherences between these states are largely invisible in this representation. To measure the Berry phase, we therefore apply direct Wigner tomography to the final cavity state [52, 62]. As figures 5.4 B, C, and D show, the Wigner functions of two-component cat states display interference fringes, whose phase directly encodes the relative phase between the dormant ($|0, f\rangle$) and walking ($|\beta, \uparrow\rangle$) components of the cat. Figures 5.4 D and E display the measured Wigner functions for both split-step walks. In the topologically trivial phase (Fig. 5.4D), the interference fringes do not acquire any phase shift after the walk, besides a small offset due to technical imperfections. For the topologically nontrivial walk (Fig. 5.4E), however, the fringes visibly shift (Fig. 5.4C), corresponding to an acquired phase of $\phi_B = 1.05\pi \pm 0.06\pi$. The topologies of the Hamiltonians which generate the walks are thereby clearly imprinted on the Wigner functions of the refocused states. A key feature of such topology is its robustness to all perturbations that do not close the spectral gap. To this end, we have performed an additional pair of quantum walks, $\hat{U}_0' = \hat{U}_W(0.64\pi, 0.28\pi)$ and $\hat{U}_1' = \hat{U}_W(0.28\pi, 0.64\pi)$ which are continuously deformable from the original walks. In this case, linecuts of the two Wigner functions yield an extracted Berry phase difference of $\Delta\phi = 1.07\pi \pm 0.09\pi$. Thus, we have successfully observed, in a systematic fashion, both phases in the canonical BDI topological insulator class [54, 30].

Additional Winding Number Measurement

Here we present an additional measurement of the winding number, in which we performed both time-independent and time-dependent split-step quantum walks with angles $\theta_1 = 0.28\pi$ and $\theta_2 = 0.64\pi$. These results of these operations are shown in figure 5.5.

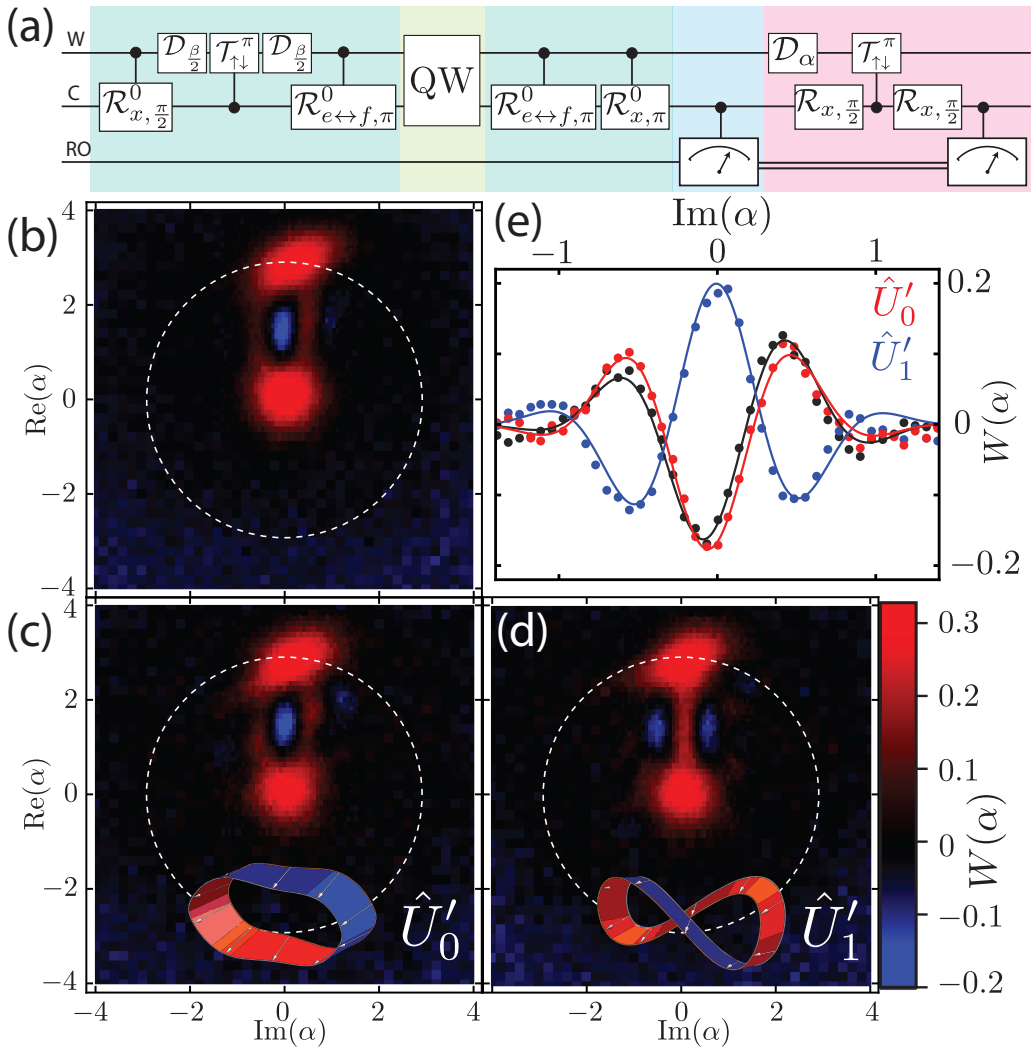

Figure 5.4: **Winding number measurement via direct Wigner tomography of refocused Schrödinger cat states. a.** Protocol for measuring topology via a time-dependent walk (Bloch oscillations). The Schrödinger cat state is first prepared (blue), after which the ten-step refocusing quantum walk is performed (green). The qubit and cavity state are then disentangled, the qubit state is purified (blue), and direct Wigner tomography on the cavity state is performed (pink). Wigner tomography of **b.** the cat undergoing no quantum walk, **c.** the cat after undergoing the trivial $\hat{U}_0$ walk, and **d.** after undergoing the topological $\hat{U}_1$ walk. Fidelities of these resulting cat states compared to pure cat states are 0.68, 0.69, and 0.67 respectively. **e.** A cut of the Wigner function, showing the fringes which encode the relative phase between the two cat components. The Berry phase—captured by the phase difference between the topological and the trivial walks—is $\phi_B = 1.05\pi \pm 0.06\pi$ in experiment, consistent with the theoretical expectations of π.

Specifically, the unitary operations, $\hat{U}_0'$ and $\hat{U}_1'$, for each step of these split-step walks are given by

$$\hat{U}_0' = \hat{T}_{\uparrow\downarrow}\hat{R}(0.28\pi)\hat{T}_{\uparrow\downarrow}\hat{R}(0.64\pi) \quad (5.4)$$

$$\hat{U}_1' = \hat{T}_{\uparrow\downarrow}\hat{R}(0.64\pi)\hat{T}_{\uparrow\downarrow}\hat{R}(0.28\pi) \quad (5.5)$$

In the measurement presented earlier in this chapter, we used a lattice with 10 sites; here, we use a lattice with 12 sites. In figure 5.5A, we plot the free evolution under this quantum walk, with the state of the walker evolving for 12 steps. As with the corresponding free-evolution walk presented previously, this serves primarily to benchmark our experimental platform, demonstrating its capability to perform the quantum walk algorithm. The population fidelities of the final walker state to theoretical predictions are quite high, above 93% in all cases, and with an average of 0.97% for both $\hat{U}_0'$ and $\hat{U}_1'$.

Our time-dependent modification of the walk protocol which transports the walker around the Brillouin zone is, as before, accomplished by inserting effective σ_z rotations before each spin-dependent translation step. Here, we use a time-dependent quantum walk with 12 steps. In this case, the fidelity of refocusing is, respectively 82% for $\hat{U}_0'$ and 80% for $\hat{U}_1'$.

Using the Schrödinger cat, we again extract a measurement of the accumulated Berry phase, and hence the winding number, from a linecut of the data. The corresponding plots are shown in panels C and D of supplementary figure 5.5, with the linecut shown in panel E. As the panels show, there is, as before, a striking difference in the Wigner functions between the topological and trivial walks. We extract a Berry phase of $1.07\pi \pm 0.09\pi$.

5.3 Details of the experimental toolbox

In this section, we describe the tools in the experimental toolbox we used to perform the quantum walk and the corresponding topological phase measurement.

Qubit-cavity system

The Hamiltonian of the qubit-cavity system (not including the fundamental cavity mode, which is used for readout only) is the dispersive Jaynes-Cummings Hamiltonian [47]:

$$\hat{H}/\hbar = \omega_q\hat{\sigma}_z/2 + \omega_c\hat{a}^\dagger\hat{a} + \chi\hat{a}^\dagger\hat{a}\hat{\sigma}_z/2 \quad (5.6)$$

Effectively, this can be viewed as a cavity with a frequency which depends on the state of the qubit. Therefore, the free evolution operator in the rotating frame of the cavity for a time t corresponds to a spin-dependent phase shift given by

$$\hat{T}_{\uparrow\downarrow} = e^{i\phi\hat{a}^\dagger\hat{a}\hat{\sigma}_z} \quad (5.7)$$

where the phase shift is $\phi = \chi t/2$. Since the lattice is a set of coherent states in the phase space of the cavity, namely $\{|x\rangle = |\beta e^{ix\phi}\rangle, x \in Z\}$ (where $\phi = 2\pi/10$), this unitary operation

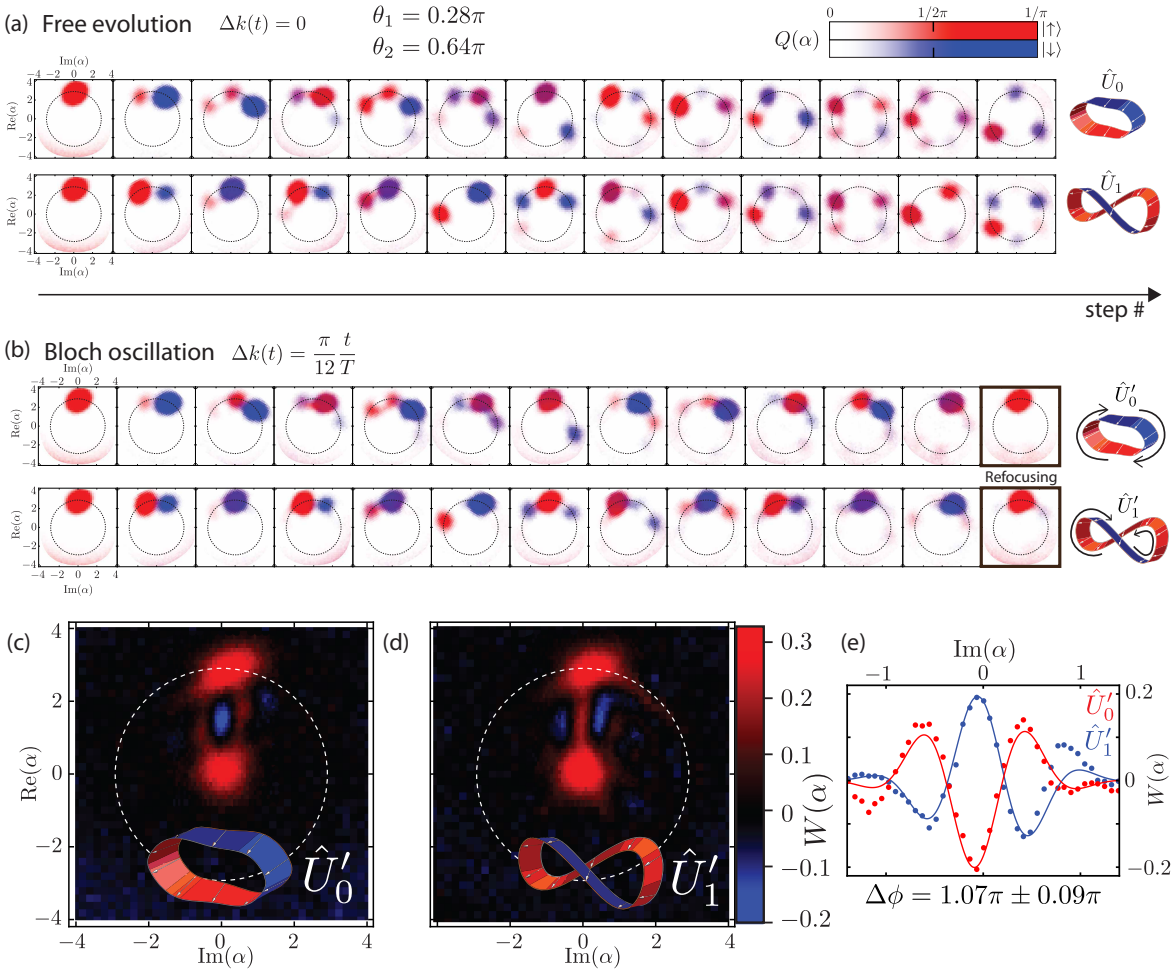

Figure 5.5: **Quantum walk with angles $\theta_1 = 0.28\pi$ and $\theta_2 = 0.64\pi$ a.** Lattice site populations (cavity Q functions) after each step of the time-independent versions of $\hat{U}_0'$ (top strip) and $\hat{U}_1'$ (bottom strip). Spin-up (red) and spin-down (blue) Q functions are superimposed, as with the walk performed in the main text. Average fidelity of the populations compared to theoretical predictions is 0.97 for both $\hat{U}_0$ and $\hat{U}_1$. **b.** Cavity Q functions after each step of the refocusing quantum walk with Bloch oscillations. The state refocuses after ten steps, as shown in the final frame for both $\hat{U}_0'$ and $\hat{U}_1'$. Refocusing fidelities (to the initial state) for $\hat{U}_0'$ and $\hat{U}_1'$ are 0.82 and 0.80, respectively. Wigner tomography of **c.** the initial cat, **d.** the cat after undergoing the trivial $\hat{U}_0'$ walk, and **d.** after undergoing the topological $\hat{U}_1'$ walk. **e.** Linecuts of the two Wigner functions, showing the extraction of the Berry phase difference, in this case $\Delta\phi = 1.07\pi \pm 0.09\pi$.

acts as a spin-dependent translation on the set of lattice states defined in the main text.

Explicitly,

$$\hat{T}_{\uparrow\downarrow}|\beta e^{ix\phi}\rangle|\uparrow\downarrow\rangle = |\beta e^{i(x\pm1)\phi}\rangle|\uparrow\downarrow\rangle \tag{5.8}$$

Thus, the crucial spin-dependent translation gate is implemented by simply waiting for a time t between successive rotations, where $t = 2\phi/\chi = 124$ ns.

Cavity field representation

Measurement of the system state after the walk, including both the lattice populations and their corresponding spin states, is performed via a sequence of two measurements: first, the qubit state is measured; second, cavity state tomography is performed. We perform two types of tomography of the cavity state to measure one of two phase space quasiprobability distributions: either the Husimi Q-function or the Wigner function. The Q function encodes the overlap of the resonator state $|\psi\rangle$ with a coherent state $|\alpha\rangle$: $Q_0(\alpha) = |\langle\alpha|\psi\rangle|^2/\pi$. Since the lattice for our implementation of the walk is a set of coherent states, Q tomography is well suited to measure site populations. However, the coherences between different states are exponentially suppressed in the Q function. Wigner tomography, on the other hand, emphasizes coherences in the form of interference fringes. Thus, for the Berry phase measurement discussed in the main text, we use Wigner tomography. Wigner tomography consists of measuring the parity Π of the oscillator state after displacing it in phase space by an amount α: $W(\alpha) = \langle\psi|D_\alpha \Pi D_{-\alpha}|\psi\rangle/\pi$. Protocols to measure these distributiosn for cavities dispersively coupled to qubits were developed at Yale by the groups of Michel Devoret and Rob Schoelkopf. We use them with slight modifications here, which we now describe.

Husimi Q tomography

To measure the Q function for a state $|\psi\rangle$, denoted $Q_{|\psi\rangle}(\alpha)$, we use the standard protocol [29] with a minor modification. $Q_{|\psi\rangle}(\alpha)$ is normally measured by displacing the oscillator by an amount α, then measuring the probability for the cavity to contain 0 photons. This photon number measurement makes use of the qubit: a number-selective π pulse is applied, mapping the zero-photon cavity population to the excited state of the qubit, whose state is then measured. This process is done repeatedly, and the measurement statistics of the qubit give the zero-photon cavity population. For this protocol to work, the qubit is assumed to start in the ground state, which in our case it does not due to the quantum walk. In our experiment, the qubit-cavity system starts out in an entangled state $|\psi\rangle = c_\uparrow|\psi_\uparrow,\uparrow\rangle + c_\downarrow|\psi_\downarrow,\downarrow\rangle$. So we first displace the state by $|\alpha\rangle$, and then measure the state of the qubit, picking out the displaced excited or ground state wavefunction. Then we apply a selective π pulse to the qubit and measure its state. Each frame of the Q functions shown in figure 5.3 consists of a 41-by-41 grid of displacements. In total, 12 million measurements were acquired with a repetition rate of 500 μs. All displacements were performed at the cavity frequency corresponding to the qubit in the ground state, so to work in the desired frame (the rotating frame of the bare cavity frequency), the plots were rotated after acquisition. Performing displacements at the bare cavity frequency was not practically feasible for technical reasons.

The distribution plotted in figure 5.3 corresponds to the superposition of the two weighted Q-functions, namely $|c_\uparrow|^2 Q_{|\psi_\uparrow\rangle}(\alpha)$ and $|c_\downarrow|^2 Q_{|\psi_\downarrow\rangle}(\alpha)$. The qubit populations $|c_\uparrow|^2$ and $|c_\downarrow|^2$ are extracted via the first QND readout. The detailed pulse sequence is shown in supplementary Fig. 5.6A.

Wigner tomography

To measure the Wigner function for a state $|\psi\rangle$, denoted $W_{|\psi\rangle}(\alpha)$, we again use the standard protocol [62] with a minor modification. $W_{|\psi\rangle}(\alpha)$ is normally measured by displacing the oscillator by an amount α, then measuring the parity of the resulting state. This parity measurement is accomplished using the qubit, by applying two unconditional $\pi/2$ pulses separated in time by an amount $1/2\chi$. Qubit measurement statistics give the state parity. Our modification to this protocol, like in the Q-function measurement, puts the cavity displacement before the initial readout to project the qubit. Each frame of figure 5.4, with the cat Wigner functions, consists of two sets of data, one coarse and one fine, meshed together. We zoomed in on the cat, taking 50 million measurements on a 41-by-41 grid of tomographic displacements corresponding to the $\alpha = [-1.25, 1.25] \times [-0.75, 3.75]$ region. The coarse set of data, superimposed, consists of another 41-by-41 grid in the $[-4, 4] \times [-4, 4]$ region with a total of 20 million measurements. We used a repetition rate of 500 μs. The detailed pulse sequence is shown in Fig. 5.6B.

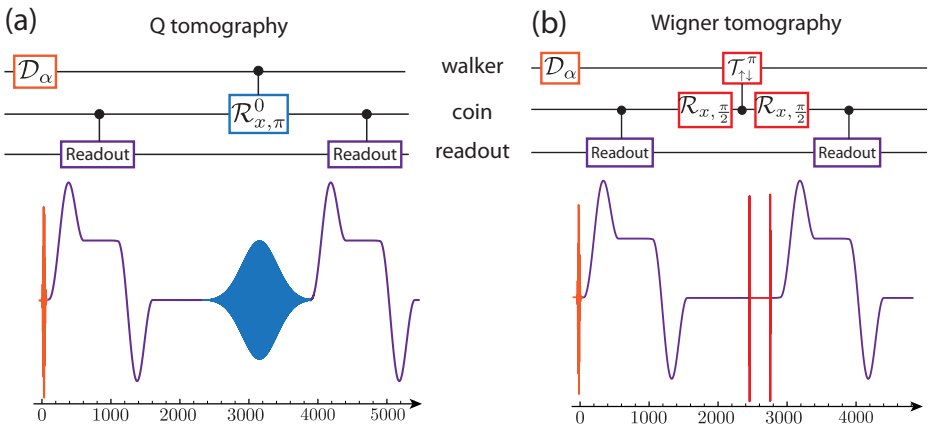

Figure 5.6: **Pulse shaping for Q and Wigner Tomography a.** Gate sequence implemented to perform the Q tomography and the corresponding pulse sequence. **b.**Gate sequence implemented to perform the Wigner tomography and the corresponding pulse sequence.

Population fidelity

Populations $P(x,\uparrow\downarrow)$ on each lattice site $|x\rangle$ for the qubit state $|\uparrow\downarrow\rangle$ were extracted from the Q tomography using a Gaussian fit at the expected lattice position. The population fidelity to the theoretical expectation $P_{\rm th}(x,\uparrow\downarrow)$ is then calculated using the following relation

$$F_{\rm pop} = \sum_x \sqrt{P(x,\uparrow)P_{\rm th}(x,\uparrow) + P(x,\downarrow)P_{\rm th}(x,\downarrow)}. \tag{5.9}$$

This definition of population fidelity is similar to the standard definition of quantum fidelity, but it only considers the populations and disregards the coherences, which we do not directly measure using Q tomography.

Wigner tomography fidelity

The fidelities of the cat states to a pure target state $|\phi\rangle$ have been directly calculated from the Wigner tomography according to the following relation [62]

$$F = \langle\phi|\rho|\phi\rangle = 1\pi \int W_{target}(\alpha)W_{cat}(\alpha)d^2\alpha \tag{5.10}$$

where $W_{target}(\alpha)$ is the Wigner function of the target state $|\psi\rangle$ and $W_{cat}(\alpha)$ is the measured Wigner tomography of the cat states associated to the density matrix ρ.

Errors associated with Wigner tomography measurement

As Wigner tomography is a parity measurement of the displaced cavity state, the measurement of which is done via a qubit measurement, associated error bars can be calculated from a binomial distribution. Here the probability of success is simply determined by the parity itself (the fraction of qubit measurements which collapsed to the excited state), calculated from the measured Wigner tomography value as $p = (1 + \pi W(\alpha))/2$. After n tries, the standard-error associated with binomial distribution is given by $\sigma = 2/\pi\sqrt{p(1-p)/n}$.

We performed 5×10^7 projective measurements per Wigner tomography on a 41-by-41 grid, resulting in $n = 3 \times 10^4$ projective measurements per point. Thus, the standard error is bounded by $1.4 \times 10^{-3} < \sigma < 1.8 \times 10^{-3}$. The radius of the points in the figure, 6×10^{-3}, is slightly larger the error bar associated with the noise due to projective measurements. Thus, we have not shown any error bars in the figure.

Implementing the Bloch oscillations

Here, we expand on the discussion of Bloch oscillations given earlier. Starting with the time-independent split step quantum walk $\hat{U}_W$ with unitary

$$\hat{U}_W(\theta_1,\theta_2) = T_{\uparrow\downarrow}R(\theta_1)T_{\uparrow\downarrow}R(\theta_2), \tag{5.11}$$

in terms of the quasimomentum operator $\hat{k} = \int_{BZ} k|k\rangle\langle k|$, this can be written

$$\hat{U}_W(\theta_1, \theta_2) = \exp(i\hat{k}\sigma_z)R(\theta_1)\exp(i\hat{k}\sigma_z)R(\theta_2). \tag{5.12}$$

The underlying Hamiltonian stems $\hat{H}_W$ from this expression, by equating it to $\exp(-i\hat{H}_W t/\hbar)$. Shifting the underlying Hamiltonian in quasimomentum space to implement the digitized Bloch oscillation can thus be accomplished by replacing $\hat{k}$ with $\hat{k} + \Delta k$ in the above expression:

$$\begin{aligned} \hat{U}_W &= \exp(i(\hat{k} + \Delta k)\sigma_z)R(\theta_1)\exp(i(\hat{k} + \Delta k)\sigma_z)R(\theta_2) & (5.13)\\ &= \exp(i\hat{k}\sigma_z)\exp(i\Delta k\sigma_z)R(\theta_1)\exp(i\hat{k}\sigma_z)\exp(i\Delta k\sigma_z)R(\theta_2). & (5.14)\end{aligned}$$

To sweep out the entire Brillouin zone, we make the momentum shift in $\hat{U}_W$ vary at each step. Choosing a value of N, the discretization of the Brillouin zone, we sweep the shift in units of $\Delta k = \pi/N$. In our case, $N = 10$.

In practice, the σ_z rotation is realized by composing a π-rotation about σ_x with another π-rotation about $\vec{n} = \cos\frac{\Delta k}{2}\vec{x} - \sin\frac{\Delta k}{2}\vec{y}$ by virtue of the identity

$$e^{\frac{i}{2}\Delta k\sigma_z} = e^{\frac{i}{2}\pi(\cos\frac{\Delta k}{2}\sigma_x - \sin\frac{\Delta k}{2}\sigma_y)}e^{-\frac{i}{2}\pi\sigma_x}. \tag{5.15}$$

In practice, we contract two σ_x rotations, the quantum walk rotation $R_x(\theta)$ with the first Bloch rotation $R_x(-\pi)$. We can thus implement the quantum walk with Bloch oscillation by applying only two rotations in a row which reads

$$R_n(\pi)R_x(\theta - \pi) = R_z(\Delta k)R_x(\theta). \tag{5.16}$$

In the ideal case, the value of Δk within a single step would be constant, as shown in 5.14. However, it turns out to be more feasible experimentally to make Δk vary smoothly over the entire protocol, so that instead of implementing at the nth step the unitary

$$\hat{U}_W(n) = \exp(i\hat{k}\sigma_z)\exp(in\Delta k\sigma_z)R(\theta_1)\exp(i\hat{k}\sigma_z)\exp(in\Delta k\sigma_z)R(\theta_2), \tag{5.17}$$

we actually implement

$$\hat{U}_W(n) = \exp(i\hat{k}\sigma_z)\exp(in\Delta k\sigma_z)R(\theta_1)\exp(i\hat{k}\sigma_z)\exp(i(n+1/2)\Delta k\sigma_z)R(\theta_2), \tag{5.18}$$

Simulations show that for the value of $N = 10$ and $N = 12$ we use in the experiment, the behavior of this walk and the ideal are essentially identical.

Pulse sequence

In this experiment, we use fixed frequency interactions and qubit/cavity drives in order to performs the requisite gates. We can perform both conditional and unconditional qubit/cavity operations by controlling the duration and shape of the driving fields used. The pulse sequences are presented in figures 5.7 and 5.6.

Unconditional rotations

Implementing the quantum walk consists of unconditional qubit rotations interspersed with spin-dependent translations corresponding to the free-evolution under the dispersive JC Hamiltonian for a time $\delta t = 2\pi/(5\chi) = 124$ ns. Qubit rotations have to be much shorter than this time to remain unconditional with respect to the cavity state. In practice, we use 7.4 ns cosine-shaped pulses for unconditional qubit rotations. In order to prevent interaction and leakage to the $|f\rangle$ state, the second excited state of the transmon, we implement pulse-shaping techniques developed by [14], particularly using the Derivative Reduction for Adiabatic Gate (DRAG) pulse combined with a static detuning of 13.5 MHz. In our experiment, these short pulses are generated using a single channel Arbitrary Wavefrom Generator (Tektronix 615) clocked at 2.7 GS.s^{-1} and modulated at 675 MHz. Note that we use similar $\pi/2$-pulses to perform the parity measurement for the Wigner tomography.

Conditional rotations

Conditional rotations are used to prepare the cat state. A number-selective rotation is enabled by the dispersive Hamiltonian, particularly the fact that the qubit transition frequency depends on the photon occupation number of the cavity through $\omega_q^n = \omega_q^0 - n\chi$. By addressing individually one of these transitions, one can perform a photon-number-resolved qubit-rotation $R^n(\theta) = R(\theta)\otimes|n\rangle\langle n| + I\otimes(I - |n\rangle\langle n|)$. The selectivity of the rotation directly depends on the spectral selectivity of the pulse. For Gaussian pulses $\epsilon(t) = Ae^{-t^2/(2\sigma)}$ one has to ensure that $\sigma \gg \chi^{-1} = 100$ ns to achieve a fully selective rotation. In our experiment, the Q-tomography is performed with a π-rotation highly selective with respect to the vacuum state $|0\rangle$: we use $\sigma = 250$ ns with a modulation frequency of 675 MHz.

However, for the cat state preparation, the constraint is less strict since we want to perform a vacuum-state-selective rotation with respect to a coherent state separated by an amplitude of $\beta = 2.78$, for which the first Fock state occupation remains small [62]. Therefore, we perform selective pulses with a high fidelity using a Gaussian shape with $\sigma = 63$ ns, and with a modulation frequency of 675 MHz. Note that the selective π-rotation on the $|e\rangle \leftrightarrow |f\rangle$ transition is performed with the same pulse timing with a modulation frequency of 450 MHz. These shorter pulses enabled us to dramatically increase the fidelity of the cat state preparation by mitigating errors originating from dephasing and the cavity's self-Kerr interaction [29].

Cavity displacement

Cavity displacements are unconditional with respect to the qubit state. We use Gaussian pulses with a width $\sigma = 10$ ns. Cavity displacements are generated by a two-channel arbitrary waveform generator (Tektronix AWG520) clocked at 1 GS.s^{-1} and modulated at 125 MHz. In practice, we perform the cavity displacement for the Q and Wigner tomography before the first qubit projection. This enables us to avoid the deformation of the cavity state by the self-Kerr interaction during the readout time (2.4 μs) and further allows us to avoid

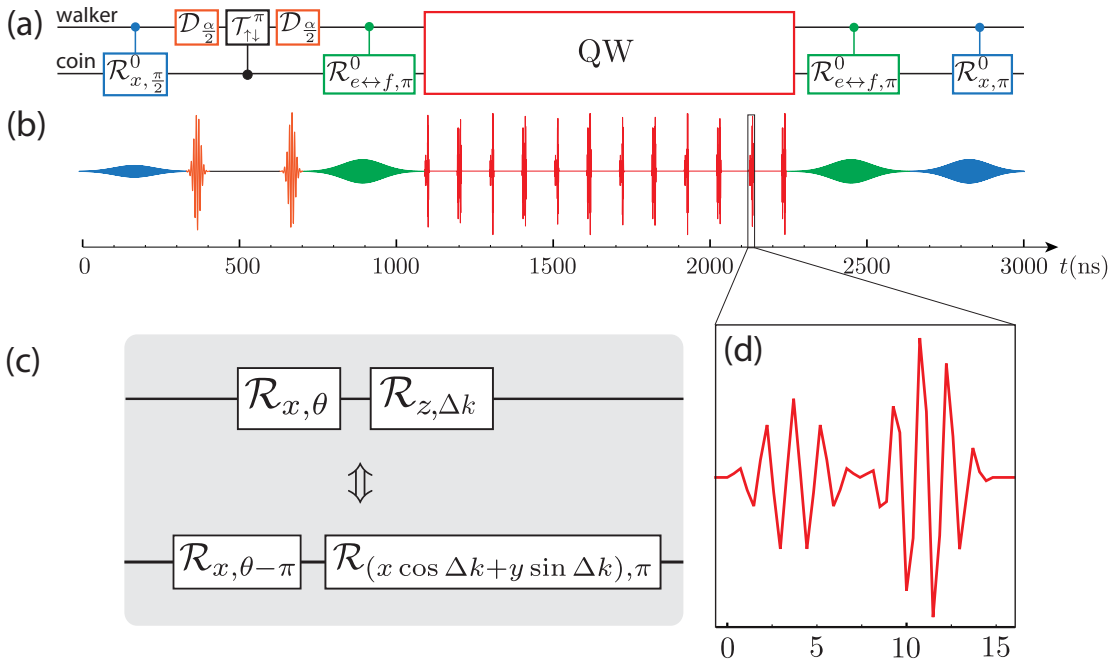

Figure 5.7: **Pulse shaping for quantum walk a.** Sequence of pulses which implement the quantum walk, including initialization of the Schroedinger cat state. **b.** Pulse shaping and timing corresponding to the sequence. **c.** Equivalence between two sets of composed rotations, with the bottom one implemented in the experiment.**d.** An expanded view showing the qubit rotation pulse shapes used for the time-dependent quantum walk.

interaction with the readout mode distorting the cavity state. Since the cavity lifetime (40 μs) is much larger than the readout time, the Q and Wigner tomography are not affected by this operation.

Readout Pulse

Three readouts are performed within a single pulse sequence: a first readout is used to herald the ground state of the qubit at the beginning of the experiment, a second one is performed for projecting the readout after the walk, and a last one is used for Q or Wigner tomography. The readout pulses have been optimized for minimizing the readout time while achieving a high readout fidelity. The shape of the pulses can be decomposed into three components: a high amplitude gaussian rise to quickly populating the readout mode followed by a medium amplitude plateau to hold the readout photon number during the actual measurement and finally a large Gaussian rise with opposite phase to quickly depopulate the readout mode. The relative amplitudes of the three components have been optimized such that the total readout time is 2.4 μs including the full depopulation time while achieving a readout fidelity of $F = 96$ %. Note that the actual recording time, corresponding to the holding plateau,

lasts 800 ns. Readout pulses are generated by a two-channel AWG (Tektronix 520) clocked at 1 GS.s^{-1} without modulation.

Device parameters

Here we give parameters specific to our experimental implementation of the toolbox described above.

Transmon qubit

The qubit consists of two aluminium paddles connected by a double-angle-evaporated aluminium Josephson junction deposited on double-side-polished sapphire. The resistance of the Josephson junction at room temperature is 7.1 kΩ.

Superconducting cavity

The qubit-cavity system is shown in supplementary Fig. 5.8. The superconducting cavity is a 3" $\times$ 0.96" $\times$ 0.2" rectangular cavity made of high-purity aluminum (5N) [47]. Three access ports are symmetrically positioned in the cavity. The readout port in the center strongly couples the TE_{110} mode (readout) to a 50 Ω line through a non-magnetic SMA connector inserted in the cavity. The pulsing port on one side of the cavity is very weakly coupled to the TE_{210} mode in order to preserve its high quality factor while being able to address it. The port on the other side is not used but it is crucial to keep the overall symmetry of the cavity. Two slots are positioned symmetrically on each side of the cavity. One slot hosts the qubit chip while the other one hosts a blank sapphire chip with the same dimensions. The blank chip enables us to enforce the symmetry of the cavity modes and therefore to preserve the high-quality factor (2×10^6) of the TE_{210} mode despite the strongly coupled readout pin sitting in the center.

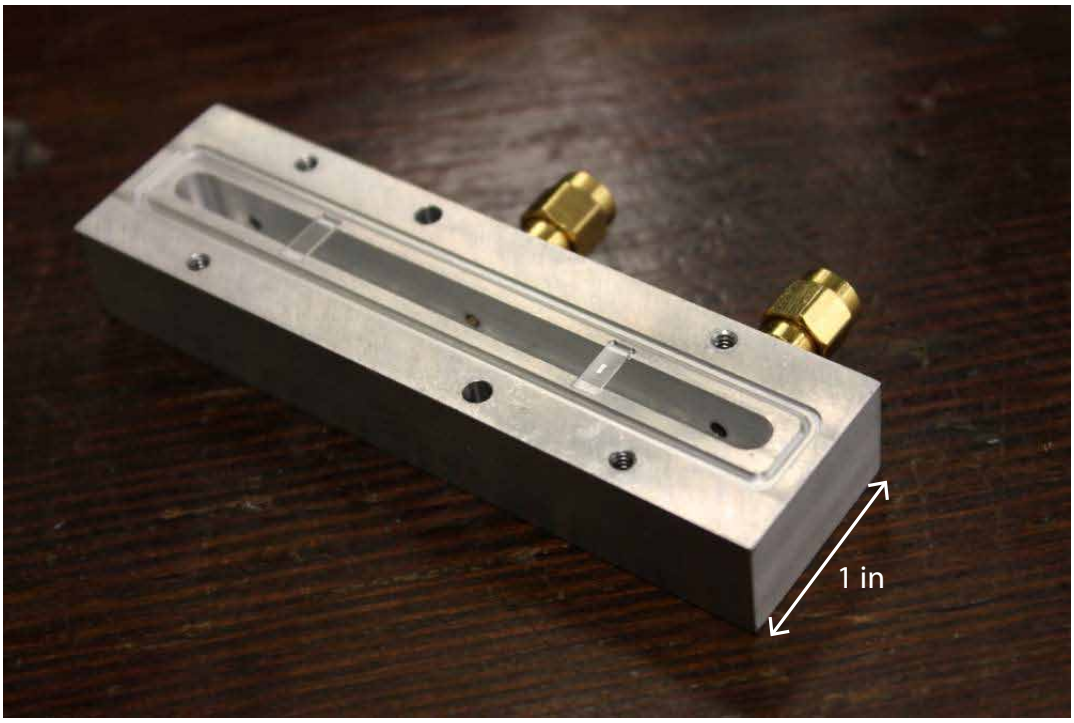

Figure 5.8: **Picture of the cavity embedding the superconducting transmon.** Two sapphire chips sit in the cavity; one contains the transmon used in the experiment, while the other is meant to preserve the symmetry of the high-Q mode used as the walker. Unthreaded holes are used to align the two halves of the cavity. Indium wire makes the seal between the two halves. The cavity is made from 5N aluminum, and with this geometry, the high-Q mode achieves a Q factor around 2 million.

qubit

$\omega_q/2\pi$	5.186 GHz
T_1	30 μs
T_2^*	5.3 μs
T_2	9 μs
α	225 MHz
$\chi_{RO}/2\pi$	1.1 MHz
$\chi_m/2\pi$	1.6125 MHz

TE_{210} mode

$\omega_m/2\pi$	7.414 GHz
T_1	40 μs
Q	2×10^6
$self-Kerr\ K/2\pi$	~ 3 kHz
$\chi_m/2\pi$	1.6125 MHz

TE_{210} mode (readout)

$\omega_m/2\pi$	6.767 GHz
κ_{ext}	$(270\text{ ns})^{-1}$
Q	10^4
$\chi_{RO}/2\pi$	1.1 MHz

Parametric amplifier

The lumped-element Josephson parametric amplifier (LJPA) [24] used to increase readout fidelity consists of a two-junction SQUID, formed from 2 μA Josephson junctions shunted by 3 pF of capacitance, and is flux biased to provide 20 dB of gain at the cavity resonance frequency. The LJPA is pumped by two sidebands equally spaced 300 MHz above and below the cavity resonance.

5.4 Theoretical details

We expand on the topological features of quantum walks discussed in the main text, directing the reader to refs. [31, 32] for the original exposition. Our definition of the split-step quantum walk discussed in the main text differs slightly from that of refs. [31, 32]: we define the split-step quantum walk to consist of repeated applications of the operator

$$U(\theta_1, \theta_2) = T_{\uparrow\downarrow} R_x(\theta_1) T_{\uparrow\downarrow} R_x(\theta_2). \tag{5.19}$$

where $R_x(\theta) = \cos(\theta/2)\hat{I} - i\sin(\theta/2)\sigma_x$ is a rotation operator acting only on the spin degrees of freedom, and

$$T_{\uparrow\downarrow} = \sum_x \left[|x+1\rangle\langle x| \otimes |\uparrow\rangle\langle\uparrow| + |x-1\rangle\langle x| \otimes |\downarrow\rangle\langle\downarrow| \right] \tag{5.20}$$

is the spin-dependent translation operator. A Hamiltonian H_W exists such that

$$e^{-iH_{\mathrm{W}}\Delta t/\hbar} = U(\theta_1, \theta_2), \tag{5.21}$$

where Δt is the interval between successive applications of $U(\theta_1, \theta_2)$. The dynamics of a system evolving continuously under the steady-state Hamiltonian H_{W} are the same as the quantum walk dynamics if the state of the system is probed only at integer multiples of Δt. We take $\Delta t/\hbar = 1$.

The unitary operator performing the walk commutes with translations of the system by an integer number of lattice sites, so the stationary states of the walk are products of the spin-1/2 wave function and plane wave states $|k\rangle$ given by

$$|k\rangle = \sum_x e^{ikx} |x\rangle. \tag{5.22}$$

Because the quantum walk protocol is invariant under discrete lattice translations, the Hamiltonian must be block diagonal in the quasimomentum basis; thus the most general form it can have is

$$H(\hat{k}) = \epsilon(\hat{k})\vec{n}(\hat{k}).\vec{\hat{\sigma}} + \gamma(\hat{k})I \tag{5.23}$$

In the quantum walk protocols we consider, the term proportional to the identity (a quasimomentum-dependent band offset) turns out to zero, giving the form

$$H(\hat{k}) = \epsilon(\hat{k})\vec{n}(\hat{k}).\vec{\hat{\sigma}}. \tag{5.24}$$

Substituting this into eq. 5.21 gives the expressions for $\epsilon(k)$ and $\vec{n}$:

$$\begin{aligned}
\cos\epsilon(k) &= \cos 2k \cos(\theta_2/2)\cos(\theta_1/2) + \sin(\theta_2/2)\sin(\theta_1/2) \\
n_x(k) &= \cos 2k \cos(\theta_2/2)\sin(\theta_1/2) + \sin(\theta_2/2)\cos(\theta_1/2)\sin\epsilon(k) \\
n_y(k) &= -\sin 2k \cos(\theta_2/2)\sin(\theta_1/2)\sin\epsilon(k) \\
n_z(k) &= -\sin 2k \cos(\theta_2/2)\sin(\theta_1/2)\sin\epsilon(k)
\end{aligned} \tag{5.25}$$

For a particular walk (i.e. a particular value of θ_1 and θ_2), there exists a vector $\vec{A}$ such that $\hat{n}(k)$ is perpendicular to $\vec{A}$ for all k:

$$\vec{A} = -\cos(\theta_1/2)\vec{y} + \sin(\theta_1/2)\vec{z} \tag{5.26}$$

This constraint forces $\vec{n}(k)$, a unit vector by definition, to lie along the great circle of the Bloch sphere perpendicular to $\vec{A}$. H_{W} can thus be characterized by the number of times $\hat{n}(k)$ winds around the vector $\vec{A}$ as k traverses the Brillouin zone.

Dynamical Phase in Quantum Walks

As stated in the main text, the digital Bloch oscillation imprints a Berry (geometric) phase on the wavefunction. However, in general, the Bloch oscillation also imprints a dynamical phase on the walker. The existence of this dynamical phase ϕ_d prevents the state from refocusing unless ϕ_d is a multiple of 2π, since unlike the Berry phase, the dynamical phase has opposite signs for states in different bands (that is, states in the upper band pick up a dynamical phase $+\phi_d$, while states in the lower band pick up a dynamical phase $-\phi_d$). In continuous-time systems with energy bands given by $\epsilon(k)$, the dynamical phase ϕ_d is given by ($\hbar = 1$)

$$\phi_d = \int_{t_i}^{t_f} \epsilon(k(t))\ dt. \tag{5.27}$$

Assuming a linear traversal of the Brillouin zone with velocity $v = dk/dt$, the dynamical phase is simply related to the integral under the energy bands:

$$\phi_d = \frac{1}{v}\int_{\mathrm{BZ}} \epsilon(k)\ dk \tag{5.28}$$

In the digital analogue of Bloch oscillations performed in the experiment, this formula takes the form

$$\phi_d = \frac{N}{\pi}\int_{\mathrm{BZ}} \epsilon(k)\ dk, \tag{5.29}$$

where N is the number of steps in which the Brillouin zone traversal is discretized. By choosing a suitable value of N, we can make the acquired dynamical phase arbitrarily close to a multiple of 2π, so that it can be ignored. For the bandstructure of our walks, with coin toss angles $\pi/4$ and $3\pi/4$, choosing $N = 10$ gives a dynamical phase which is close to a multiple of 2π and thus allows the state to refocus.

View of Evolution in Quasimomentum Space

As the quantum walk is initialized with the walker localized on a single lattice site, the initial wavefunction is not an eigenstate of the effective Hamiltonian but rather a superposition of all the quasimomentum states allowed by the periodic boundary conditions of our system and their corresponding spin eigenstates. That is, for those quasimomenta k satisfying $e^{ikN} = 1$, with N the number of lattice sites in the circle, the initial wavefunction can be written

$$|\Psi\rangle = \sum_k \alpha_k |k, \hat{n}(k)\rangle + \beta_k |k, -\hat{n}(k)\rangle, \tag{5.30}$$

where $|\hat{n}(k)\rangle$ and $|-\hat{n}(k)\rangle$ are the spin eigenstates corresponding to the quasimomentum k, i.e. the spin eigenstates of the Hamiltonian $H = \hat{n}(k) \cdot \vec{\sigma}$.

Upon undergoing the refocusing quantum walk, the states in the upper and lower bands evolve as follows:

$$|k, \hat{n}(k)\rangle \rightarrow e^{+i\phi_d + i\phi_B^+} |k, \hat{n}(k)\rangle \tag{5.31}$$

$$|k, -\hat{n}(k)\rangle \rightarrow e^{-i\phi_d + i\phi_B^-} |k, -\hat{n}(k)\rangle \tag{5.32}$$

Here ϕ_d is the dynamical phase, which for the number of steps we have chosen, is a multiple of 2π and can be neglected; while ϕ_B^+ and ϕ_B^- are the Berry phases corresponding to the upper and lower bands, given by (compare Eq. (2) in the main text)

$$\phi_B^{\pm} = i \int_{\mathrm{BZ}} \langle k, \pm\vec{n}(k) | \partial_k | k, \pm\vec{n}(k)\rangle dk \tag{5.33}$$

$$\tag{5.34}$$

As for general spin-1/2 systems, the Berry phase is equal to half the subtended solid angle of the path $\vec{n}(k)$ as k traverses the Brillouin zone. In our case, $\vec{n}(k)$ either winds around the Bloch sphere once or zero times; in either case, the winding of $\vec{n}(k)$ and $-\vec{n}(k)$ is the same, and thus the accumulated Berry phase is the same for both bands.

5.5 Conclusion

In this chapter, we have demonstrated a quantum-walk based simulator capable of emulating topological phases and directly measuring their topological invariants. These invariants underlie phenomena such as topologically protected edge states [32], which have been previously observed with quantum walks. In directly measuring the associated topological invariants, our work provides the missing piece of this bulk-edge correspondence for quantum walks. A direct extension of our protocol is the realization of multi-dimensional quantum walks [31], which has the potential to simulate novel topological insulators in two and three dimensions (e.g. Hopf insulator) [41]. Looking forward, an outstanding challenge is the generalization of our protocol beyond single-particle physics, to measure topological invariants of interacting quantum many-body systems [55].

Building on the toolbox we have presented in these two chapters, there are many follow-on experiments which can be imagined using superconducting circuits to explore properties of quantum walks.

A first follow-on, which might even be possible with the same experimental setup described in this chapter, is to perform a two-dimensional (or even three-dimensional) quantum walk. This could be done simply by coupling up to three transmon qubits to two or three long-lived cavity modes. Here, each cavity mode would act as one spatial dimension of the quantum walk. If each transmon interacts dispersively with each oscillator mode, then by tuning the relative dispersive shifts between each transmon and each oscillator, it should be possible to perform spin-dependent translations in two or three different dimensions. Whereas the one-dimensional quantum walk we presented in this chapter took place on a circle, the two-dimensional quantum walk would take place on a torus, and the three-dimensional version would take place on whatever the three-dimensional analogue of a torus is.

Experimentally, the cavity we used for the quantum walk experiment in this chapter features multiple long-lived modes. Remember that the feature of the mode which made it long-lived was the node at the center of the cavity (where the fast readout mode coupled to the transmission line). Simulations and initial spectroscopy suggested that the next mode with a node at the center had a frequency of around 8.7 GHz. We spent some time trying to measure the coupling of this mode to the transmon, but were unsuccessful. This might be because the transmon's location inside the cavity was near another node of the 8.7 GHz mode, or because of the low signal-to-noise ratio of our measurement chain at that frequency. Either way, it should not be difficult to redesign the cavity/transmon system to enable at least the two-dimensional quantum walk.

The implementation of the two- and three-dimensional quantum walks would be interesting for at least two reasons. First, as shown by some experiments by the Silberhorn group, quantum walks (featuring a single walker) in higher dimensions can simulate the dynamics of interacting quantum particles in lower dimensions. Second, one can explore topological featues of quantum walks in higher dimensions using this approach. It is thought that quantum walks can realize all known types of topological band structures in two and three dimensions. A particularly attractive target might be the implementation of a topological quantum walk in three dimensions which can realize an as-yet unexplored (experimentally) phase of matter known as the Hopf insulator. Our approach of using Bloch-oscillating quantum walks to extract topological phases should generalize to higher dimensions.

A more speculative long-term direction is using quantum walks to study topology in interacting or many-body quantum systems. All of the experiments discussed so far have been non-interacting, or single-particle experiments. The topological features have been present in the bandstructures of the system. However, it might be possible to use quantum walks with multiple walkers to controllable build up to many-body systems, which feature their own topological properties. We should emphasize that while this would be an extremely interesting line of work, it is not known at the time of writing whether it is even possible to simulate a many-body topological system using a quantum walk. Even if it were possible

to devise such a quantum walk protocol, mapping the many-body topological invariant to a measurable quantity would present a new challenge. Unlike single-particle topological invariants, which can be mapped on to Berry phases, the topological invariants typically studied in many-body systems are of a different type. It is unclear how one would measure such a topological invariant.

Another long-term goal would be the execution of a quantum walk on an arbitrary graph. This has yet to be demonstrated on any platform in which quantum walks have been executed, but would likely have many applications in using quantum walks to perform quantum algorithms. One possibility for realizing this in a circuit-QED system would be a two-mode cavity (for a two-dimensional embedding of the graph) with tunable dispersive shifts between the transmon and each of the two modes. This might not allow for a realization of the quantum walk on an arbitrary graph, but should allow for more complex structures than have been seen to date. It would be interesting theoretically to explore what sorts of graphs one could create using this scheme.

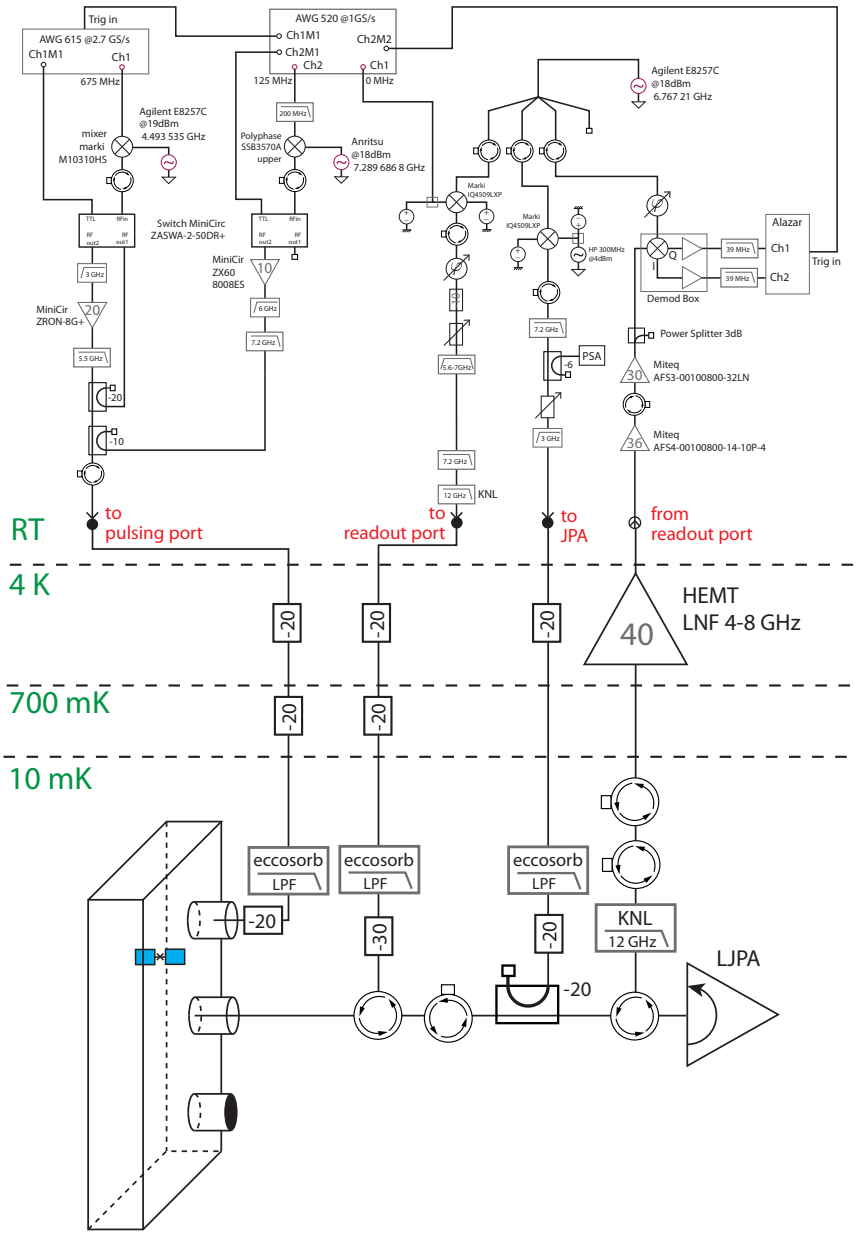

Figure 5.9: **Detailed block diagram of the measurement setup** Our measurement is performed in a dilution refrigerator at a base temperature of 10 mK. We use two input lines. One, directed into the weakly coupled pulsing port, serves three purposes: it has a high-amplitude channel for unconditional qubit pulses, a low-amplitude channel for conditional qubit pulses, and a channel for cavity displacement pulses. The other line is directed toward the readout port and is used to perform a homodyne reflection measurement of the TE_{110} mode of the cavity. The readout signal is sent through a chain of low-noise amplifiers before down-conversion and digitization, allowing for qubit state measurement. A third line is used to pump the parametric amplifier with detuned sidebands.

Chapter 6

Molecular Spectra with a Hybrid Algorithm

In previous chapters, we've used transmon circuits to perform quantum simulation in the *analog* sense: that is, in those experiments the transmons and coupled cavities were used to directly realize either a particular Hamiltonian (in the case of the Bose-Hubbard experiments) or class of unitary dynamics (in the case of the quantum walk). In the remainder of this thesis, we switch gears slightly to digital quantum simulation. In digital quantum simulation, we abstract the transmons as qubits and perform logic gates on them, after which their states are measured in the computational basis.

This chapter is concerned with a particular simulation algorithm known as the *variational quantum eigensolver* (VQE). This algorithm aims to solve the problem of determining the energy spectra of complex quantum systems, particularly those of large molecules which may have technological significance. The variational quantum eigensolver is not a purely quantum algorithm but rather a *hybrid* quantum-classical algorithm: as will be described in more detail below, the algorithm leverages both quantum and classical computational resources in the calculation of molecular spectra. In effect, VQE uses the quantum computer only to perform a particular subroutine which is thought to be difficult for a classical computer: determining the average energy of a particular quantum state of the system.

The main result reported in this chapter is the use of a two-qubit transmon processor to execute a particular version of the VQE algorithm, with the proof-of-principle task of extracting the spectrum of the H_2 molecule. While experimental implementations of VQE had previously been reported in a variety of quantum systems, this work is the first to use a novel variant of the basic VQE algorithm, known as the *quantum subspace expansion* (QSE). The QSE has two nice properties which make it attractive for quantum chemistry calculations:

- The QSE can mitigate the effect of some incoherent errors which occur on the quantum processor, and

- Using the QSE, energies of both ground and low-lying excited states can be extracted. Previous VQE implementations had focused mostly on the ground state.

6.1 Variational Quantum Eigensolver: Theory and Background

The basic idea underlying the VQE algorithm is the quantum variational principle, which is covered in most undergraduate quantum mechanics courses. The principle simply states that for a quantum system prepared in an arbitrary state, the expectation value of the system Hamiltonian is greater than the ground-state energy. This suggests a simple (though impractical) method for placing an upper bound on the ground-state energy of any Hamiltonian: guess a bunch of system states, calculate the expectation value of the Hamiltonian $\langle H \rangle$ for each one, and take the minimum value. In practice—or, at least on homework sets—one usually takes a slightly more sophisticated approach, by parameterizing a family of candidate system wavefunctions, and finding the minimum value $\langle H \rangle$ for each one. By the variational principle, this minimum value places an upper bound on the ground-state energy of H, though how good a bound this is depends on how close the parameterized set of wavefunctions comes to including the true ground-state wavefunction.

In principle, the variational principle can be used on arbitrary quantum systems, except that, unlike the classroom example in which one typically finds the minimum value analytically, numerical optimization would generally be used. However, an obvious problem arises when one attempts to use the variational principle to calculate the ground state energy of a large, complicated system—such as a molecule—using only classical resources: for classical computers, even representing the wavefunction corresponding to a highly-entangled quantum state is costly, in the worst case scaling exponentially with system size. So, given a particular parameterized set of wavefunctions, the step of *evaluating the expected value of the Hamiltonian for a given set of parameters* turns out to be prohibitively expensive. This is where the VQE algorithm comes in: instead of using the classical computer to compute $\langle H \rangle$, in VQE the energy is evaluated using measurements carried out on the quantum processor.

A precise description of the VQE algorithm is as follows: given a Hamiltonian of interest, one first picks a basis and maps the Hamiltonian to a system of qubits, expressing it usually in terms of products of Pauli operators. Stated another way, the electronic structure Hamiltonian, an operator on the space of electronic wavefunctions, is first cast into a form suitable for evaluation on a quantum processor. For example, as we will see shortly, the molecular hydrogen Hamiltonian we work with can be converted into the qubit form

$$H_Q = g_0 + g_1\sigma_z^1 + g_2\sigma_z^2 + g_3\sigma_z^1\sigma_z^2 + g_4\sigma_y^1\sigma_y^2 + g_5\sigma_x^1\sigma_x^2, \tag{6.1}$$

where the coefficients g_i, and thus the Hamiltonian itself, depend parametrically on R, the separation between the two hydrogen nuclei. For a given two-qubit state $|\psi\rangle$, prepared on the quantum processor, the expectation $\langle H_Q \rangle$ can then be evaluated through repeated

measurements of Pauli correlators. So, the next step in the algorithm is to parameterize a family of quantum circuits which act on the system of qubits to prepare such states. Starting with a random value of the parameters, the quantum computer executes the corresponding circuit, (starting in the state $|00\rangle$), and the expectation values of all of the operators in the above expression are measured. This yields an estimate of the expectation value of the Hamiltonian for the given parameters, which is then used (by the classical computer) in an optimization routine to suggest a new value of the parameters, and the process is repeated until convergence (specified by the optimization routine). Once converged, the algorithm has arrived at an estimate of the ground state energy of H_Q. Schematically, the VQE algorithm is shown in figure 6.1.

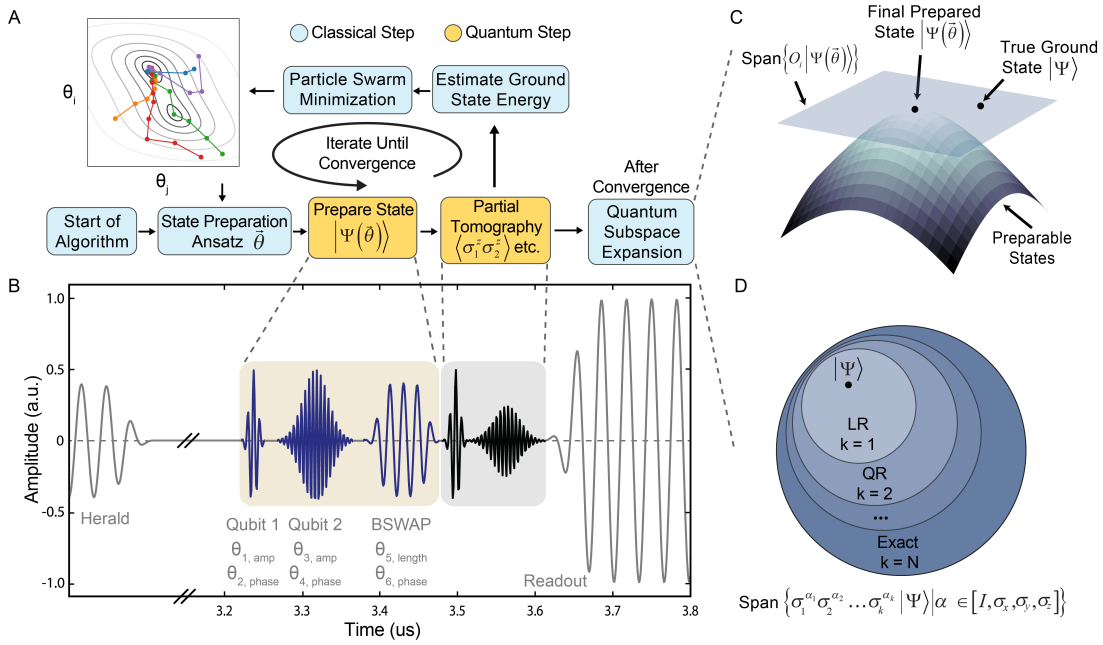

Figure 6.1: Description of the variational quantum eigensolver algorithm and associated quantum subspace expansion. (A) Flowchart outline of the algorithm with classical resources colored in blue and quantum resources colored in yellow. (B) Typical qubit preparation and measurement sequence consisting of a herald, single-qubit and two-qubit pulses, tomography and readout. (C) Cartoon of the QSE protocol; operators from O_i are used to expand about the variational solution provided by the VQE, allowing for the mitigation of incoherent errors that otherwise render the true ground state inaccessible. (D) QSE basis hierarchy obtained from expanding about the VQE reference solution. At $k = 1$ one has the linear response (LR) subspace while at $k = N$ one spans the entire subspace corresponding to the particle number of the reference state, adapted from [39].

Quantum subspace expansion

The VQE algorithm gives a nice way to estimate both the ground-state energy and the parameterized circuit to prepare the ground-state wavefunction on the quantum processor. However, quantum hardware, at least prior to the experimental implementation of error correction, will be plagued by gate errors, both coherent and incoherent. In principle, the VQE algorithm should be able to correct for coherent errors, as it is based on an optimization; however, incoherent errors cannot be corrected by the bare VQE algorithm. Also, the VQE algorithm described thus far only determines ground-state energies; in some cases it might be desirable to also determine the energies of low-lying excited states. This is where the quantum subspace expansion, which is the novel feature of the experiments described here, comes in.

Once the bare VQE algorithm has converged on an estimate of the ground state wavefunction, the quantum subspace expansion can be applied. It proceeds by measuring additional Pauli correlators (which were not necessarily present in the original Hamiltonian) that form an approximate matrix representation of H_Q within an expanded subspace. This matrix can then be diagonalized classically to yield both low-lying excited-state energies and a refined ground-state energy estimate (Fig. 6.1C). If the expansion is chosen such that its dimension scales polynomially with system size, this classical matrix calculation is efficient [39]. The effectiveness of the QSE thus requires the existence of such a subspace which captures a significant amount of the excited state support.

We expect that molecular excited energy levels differ from the ground state primarily by excitations which promote a single electron from an occupied to an unoccupied orbital. Therefore to a good approximation, these states are linear combinations of $\{S_1 : a_i^\dagger a_j \left|\psi_{GS}\right\rangle\}$, where a_j ($a_i^\dagger$) are fermionic annihilation (creation) operators for the electronic orbitals. While S_1 could serve as a subspace, a more natural choice when working with qubits involves the set of single Pauli flips $\{P_1 : \sigma_\alpha^k \left|\psi_{GS}\right\rangle \mid \alpha \in \{x, y, z\}, k \in \{1, 2\}\}$ (Fig. 6.1D), which we refer to as a linear response expansion. To calculate the matrix elements H_{ij} in the P_1 basis, we use the quantum processor to evaluate the inner products

$$H_{ij} = \left\langle\psi_{GS}\right| \sigma_i^\dagger H_Q \sigma_j \left|\psi_{GS}\right\rangle , \tag{6.2}$$

where $\left|\psi_{GS}\right\rangle$ is taken to be the initial approximate ground state $\left|\psi(\vec{\theta}_{min})\right\rangle$, found via the VQE routine.

Beyond providing a means of calculating molecular excited state energies, it was conjectured in ref. [39] that the inclusion of specific measurement operators expanding the number of states under consideration, the QSE could improve the accuracy of the initial VQE ground state estimate. While the VQE can in principle correct for the presence of coherent gate errors, the QSE was thought to additionally correct for incoherent errors, such as dephasing or amplitude damping. As discussed in the results section, we find experimental support for this conjecture.

Mapping the H_2 Hamiltonian to two qubits

In this section, we describe the mapping between the Hamiltonian of molecular hydrogen and the two-qubit Hamiltonian suitable for our experimental system. The first step is the choice of basis in which to expand the Hamiltonian. In this work, we use the standard Gaussian STO-3G basis set [25]. Common in computational chemistry, the STO-nG basis sets are *minimal* basis sets, meaning that the set consists of only enough orbitals to contain all the electrons in the neutral atom. Thus, for a hydrogen atom, the basis set consists of only a single orbital, the $1s$ orbital. The number '3' in STO-3G indicates that the molecular orbitals (in this case, only the $1s$ orbital) are approximated by a linear combination of 3 Gaussian functions:

$$\psi_{STO-3G}(s) = c_1\phi_1 + c_2\phi_2 + c_3\phi_3, \tag{6.3}$$

where each ϕ_i is given by a radial Gaussian function:

$$\phi_1 = \left(\tfrac{2\alpha_1}{\pi}\right)^{3/4} e^{-\alpha_1 r^2} \tag{6.4}$$

$$\phi_2 = \left(\tfrac{2\alpha_2}{\pi}\right)^{3/4} e^{-\alpha_2 r^2} \tag{6.5}$$

$$\phi_3 = \left(\tfrac{2\alpha_3}{\pi}\right)^{3/4} e^{-\alpha_3 r^2} \tag{6.6}$$

Here, the six numbers c_1, c_2, c_3, α_1, α_2, and α_3 are determined by fitting eqn. (6.3) to a Slater-type orbital. For hydrogen, a Slater-type orbital is defined simply by

$$\psi_{1s}(\mathbf{r}) = \left(\frac{1}{\pi}\right)^{\frac{1}{2}} e^{-\mathbf{r}} \tag{6.7}$$

After expressing the hydrogen Hamiltonian in the STO-3G basis set, the resulting Hamiltonian was then projected onto a particle-conserving and spin-conserving manifold, since the interaction Hamiltonian should conserve both of these quantities. That is, within a molecular orbital basis we define spatial orbitals 1 and 2 with possible spins α and β such that the 4 spin-orbitals in the system can be populated by the second quantized operators $a^\dagger_{1\alpha}, a^\dagger_{1\beta}, a^\dagger_{2\alpha}, a^\dagger_{2\beta}$. We start with the reference state defined by $a^\dagger_{1\alpha}a^\dagger_{1\beta}\left|vac\right\rangle$, where $\left|vac\right\rangle$ is the Fermi vacuum state. This generates the following four basis states that we map to computational basis states explicitly as follows:

$$\begin{aligned}
a^\dagger_{1\alpha}a^\dagger_{1\beta}\left|vac\right\rangle &\rightarrow \left|00\right\rangle \\
a^\dagger_{1\alpha}a^\dagger_{2\beta}\left|vac\right\rangle &\rightarrow \left|01\right\rangle \\
a^\dagger_{2\alpha}a^\dagger_{1\beta}\left|vac\right\rangle &\rightarrow \left|10\right\rangle \\
a^\dagger_{2\alpha}a^\dagger_{2\beta}\left|vac\right\rangle &\rightarrow \left|11\right\rangle
\end{aligned}$$

Note that the states we have left out of this expansion, namely $a^\dagger_{1\alpha}a^\dagger_{2\alpha}\left|vac\right\rangle$ and $a^\dagger_{1\beta}a^\dagger_{2\beta}\left|vac\right\rangle$, do not couple (via the Hamiltonian) to the four states above, as such a coupling would require a spin flip.

We note that such a reduction to two qubits or fewer can also be achieved either through the Bravyi-Kitaev transformation, as noted by O'Malley et al. [45], or through alternative symmetry enforcing transformations as introduced by Bravyi et al [11]. The Hamiltonian in this space was then expressed in the basis of Pauli operators to yield a Hamiltonian of the form:

$$H_Q(R) = \sum_{ij}^{\alpha\beta} g_{ij}(R)\sigma_\alpha^i \sigma_\beta^j \tag{6.8}$$

for each nuclear configuration R, where σ_α^i is a Pauli operator acting on qubit i from $\sigma_\alpha^i \in \{I^i, \sigma_x^i, \sigma_y^i, \sigma_z^i\}$. Due to additional spatial, spin, and time-reversal symmetry in the molecular Hamiltonian, many of the coefficients are 0 for all nuclear configurations R and all are real-valued. As a result, the Hamiltonian may be more compactly expressed as

$$H_Q(R) = g_0(R) + g_1(R)\sigma_z^1 + g_2(R)\sigma_z^2 + g_3(R)\sigma_z^1\sigma_z^2 + g_4(R)\sigma_y^1\sigma_y^2 + g_5(R)\sigma_x^1\sigma_x^2. \tag{6.9}$$

6.2 Experimental Methods

Quantum processing

The quantum processor we use to evaluate expectation values consists of two transmon qubits. The qubits are initialized in the joint ground state $|00\rangle$ via a heralding measurement [27]. A generating circuit $U(\vec{\theta})$ is then used to prepare the desired trial wavefunction (with $\vec{\theta}$ specified by the classical hardware—see next section).

$U(\vec{\theta})$ consists of three microwave pulses resonant with the desired qubit transition (shown in Fig. 6.1*B*). First, two single-qubit rotations take place, parameterized by amplitudes (θ_1, θ_3) and phases (θ_2, θ_4). Second, an entangling operation, known as the bSWAP gate [50], performs a rotation within the subspace spanned by $\{|00\rangle, |11\rangle\}$, parameterized by a length (θ_5) and a phase (θ_6).

Single-qubit pulses on qubit A and B last 50 and 70 *ns* respectively, and achieve fidelities of ∼99%. The two-qubit pulse takes up to 310 ns and approaches a fidelity of ∼96%. After state preparation via $U(\vec{\theta})$, tomographic reconstruction is used to evaluate $\langle H\rangle = \sum_{ij} h_{ij}\langle\sigma_i\sigma_j\rangle$. A near-quantum-limited traveling wave parametric amplifier [35, 44] enables high-fidelity single-shot measurement of the joint qubit state (see next subsection). The entire sequence, including both state preparation and measurement, comprises less than ∼1.5 μs, well below the coherence times of the qubits: 16 μs T_{1A}, 13.5 μs T_{2A}^*, 12 μs T_{1B}, 3.5 μs T_{2B}^*.

Quantum hardware — details

Here we provide details of the quantum processor used in the experiment. The device consists of two superconducting transmon qubits [34] on a single silicon chip, mounted in and coupled

to a three-dimensional copper cavity [47]. Each transmon consists of a capacitor shunted by a nonlinear inductance; in our device one of the qubits uses a single Josephson junction as the nonlinear inductance, with a fixed frequency of 3.788 GHz, while the other uses a SQUID loop, allowing for tuning the frequency (via an external magnetic field) from a zero-flux value of roughly 5 GHz to the working frequency of 4.111 GHz. The copper cavity exhibits a resonant frequency of 7.122 GHz with a loaded linewidth $\kappa_{ext} \approx 8$ MHz, set primarily by the coupling (in a reflection geometry) to a 50-ohm environment (see Fig. 6.2). The cavity is mounted at the 10 mK stage of a dilution refrigerator.

We detect the state of the qubits by using a heterodyne measurement (at heterodyne frequency 11 MHz) of the resonant cavity frequency, exploiting the dispersive shift between the qubits and cavity. Because the two-qubits are coupled to a single cavity, the dispersive shift is roughly equal in magnitude for both qubits, and thus distinguishing the states $|01\rangle$ and $|10\rangle$ with single-shot fidelity is impossible. However, our measurement is able to distinguish the joint two-qubit ground state $|00\rangle$ from all other computational states, which is sufficient for reconstructing the Pauli correlators necessary for evaluating the expectation value $\langle H \rangle$. To evaluate $\langle H \rangle$ we first reconstruct the two-qubit density matrix using a set of 32 tomographic measurements (see [16] for details), then calculate the necessary correlators given the density matrix. In future implementations of VQE on larger quantum systems, full tomography will be impossible (due to an exponential scaling of the number of required measurements). Instead, only the necessary correlators will be directly measured. For this reason, our reconstruction of the two-qubit density matrix from the tomographic measurements did not use any method such as maximum-likelihood estimation which enforces physicality (positivity and trace-normalization) on the result.

Classical processing

With the two-qubit processor providing a means to efficiently evaluate $\langle H \rangle(\vec{\theta})$, the classical computer uses a particle-swarm optimizer (PSO) to find parameter values $\vec{\theta}_{min}$ which minimize this objective function, as shown in Fig. 6.2*A*. The PSO approach has two properties useful for this work: it is likely to avoid getting trapped in local minima and it is more robust to noisy objective-function calls [48]. The optimization treats a single point in parameter space as a particle, which has a velocity and position. A swarm of n such particles $\{|\psi(\vec{\theta}_{s,i})\rangle, i \in [1, n]\}$ (with s the swarm iteration number) is first randomly initialized and then at each iteration, the particles' positions are updated based on both their own energy evaluation and those of others in the swarm. Figure 6.2*B* shows how iterating through this loop allows the particles to converge on a set of control parameters that prepares the best approximation of our system's ground state $\left|\psi(\vec{\theta}_g)\right\rangle$ and its associated energy.

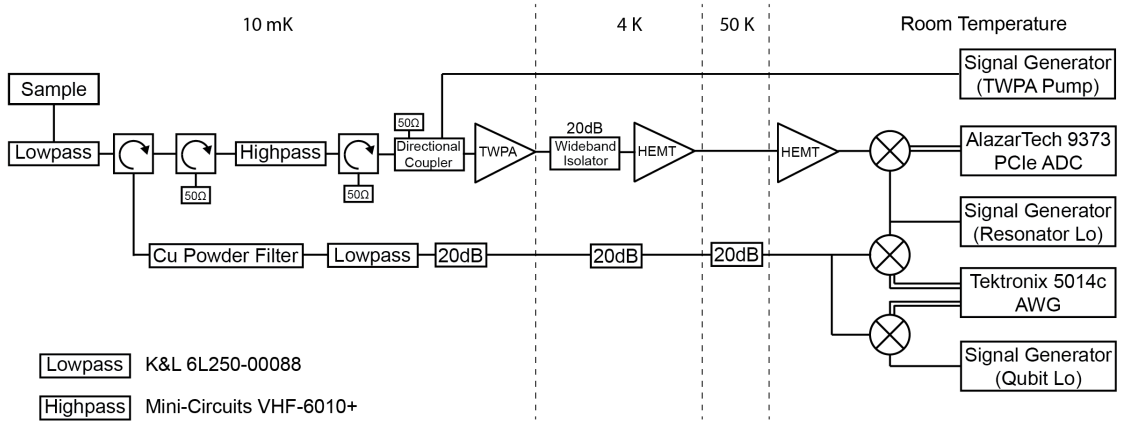

Figure 6.2: Schematic of the measurement setup used in the experiment. At the 10 mK stage of the dilution refrigerator, the sample is connected in a reflection geometry to the 50 ohm environment from which it receives qubit/cavity pulses. These pulses are generated at room temperature by the electronics shown on the right of the figure, and pass through several stages of attenuation on the way to the sample. To enable high-fidelity measurement of the qubit state, a near-quantum-limited Traveling Wave Parametric Amplifier (TWPA) [35] amplifies the signal after reflection off the cavity. Further amplification is provided by a HEMT amplifier at the 4 K state of the dilution refrigerator, after which the signal is amplified at room temperature, downconverted to a heterodyne frequency of 11 MHz, and digitized by an AlazarTech 9373 ADC. From this data, the qubit state is determined in software.

6.3 Results

We apply our algorithm to the H_2 molecule for 45 internuclear distances between 0.05 Å and 3.85 Å. As shown in Fig. 6.2*A* for a internuclear distance of 1.55 Å and a random initialization of 20 swarm particles over $\vec{\theta}$, we observe good convergence of the control parameters within 12 swarm iterations. Each function evaluation consists of 10,000 acquisitions and lasts on the order of a minute, resulting in a total algorithm run time of approximately four hours. Experimentally optimized parameters show deviation from those that would be expected in the case of idealized gates. In particular, while the experimental single-qubit gate amplitudes and two-qubit bSWAP length agree with numerical simulations, the phase of the bSWAP differs significantly, most likely due to an unaccounted for Stark shift during application of the gate. The successful convergence of the algorithm despite this miscalibration thus provides additional proof of the protocols intrinsic ability to correct for coherent errors.

Plotting the median energy of the swarm as a function of iteration number, we observe a large initial energy error due to the random nature of the particle initialization, followed by an almost monotonic decrease towards the exact theoretical value. When calculating

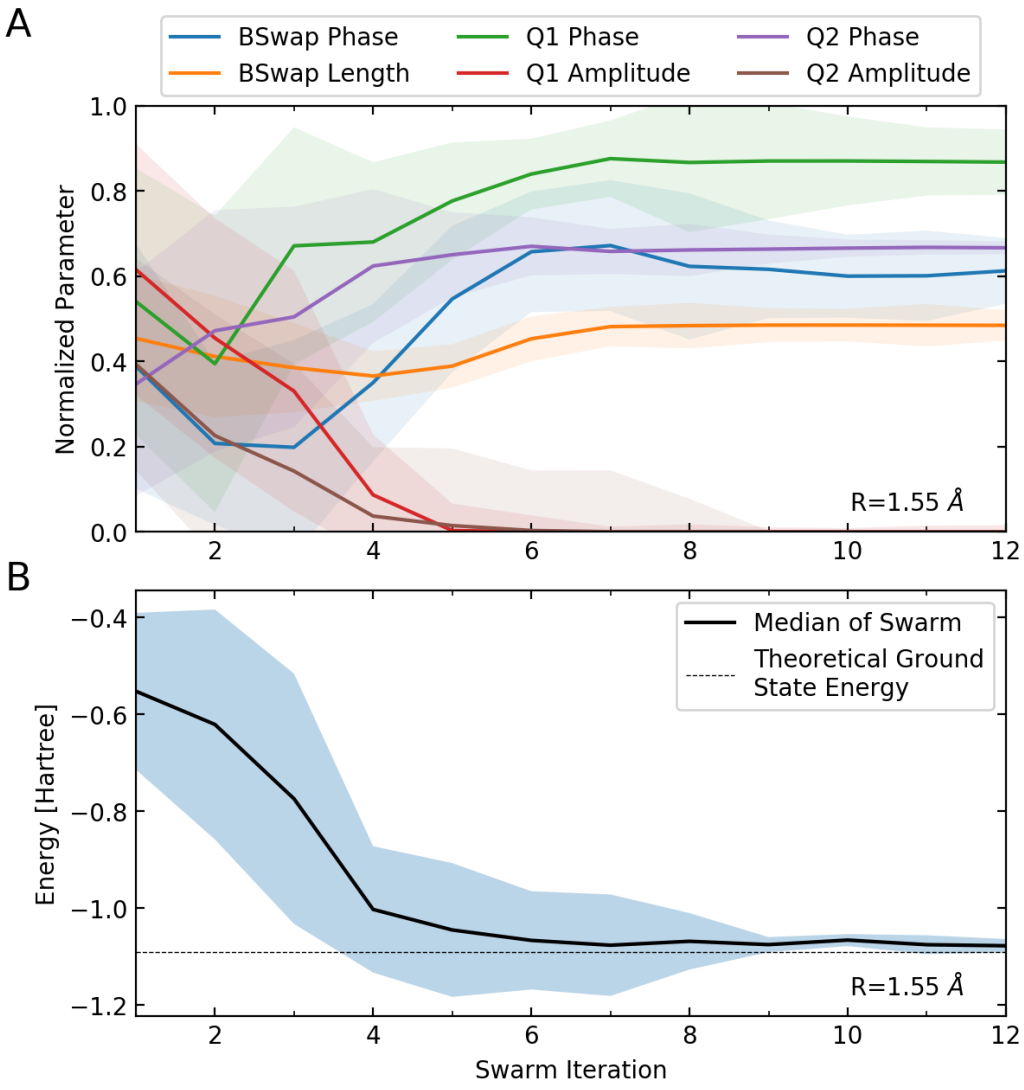

Figure 6.3: Control parameter convergence as a function of classical optimizer iteration. (A) Median (solid line) and standard deviation (shaded region) for all 6 normalized parameter values as a function of swarm iteration number at an internuclear bond distance of 1.55 Å. A swarm of 20 particles demonstrates convergence after approximately 12 iterations or equivalently 240 function evaluations. (B) Median energy (solid line) and standard deviation (shaded region) of swarm particles as a function of iteration number for the corresponding data in (A). Monotonic convergence of median energy towards the theoretical value is observed followed shortly thereafter by a rapid decrease in swarm energy variance.

an estimate for a new internuclear distance, we exploit the smoothness of the parameter landscape and re-initialize the swarm particles around the minimum found in the preceding

run, allowing them to vary by only 5% from their previous optimum values. This results in subsequent runs requiring fewer resources—20 particles and 6 swarm iterations—in order to reach convergence. Once each internuclear separation of interest has been processed, we have an initial approximation for the ground state energy function of the H_2 molecule.

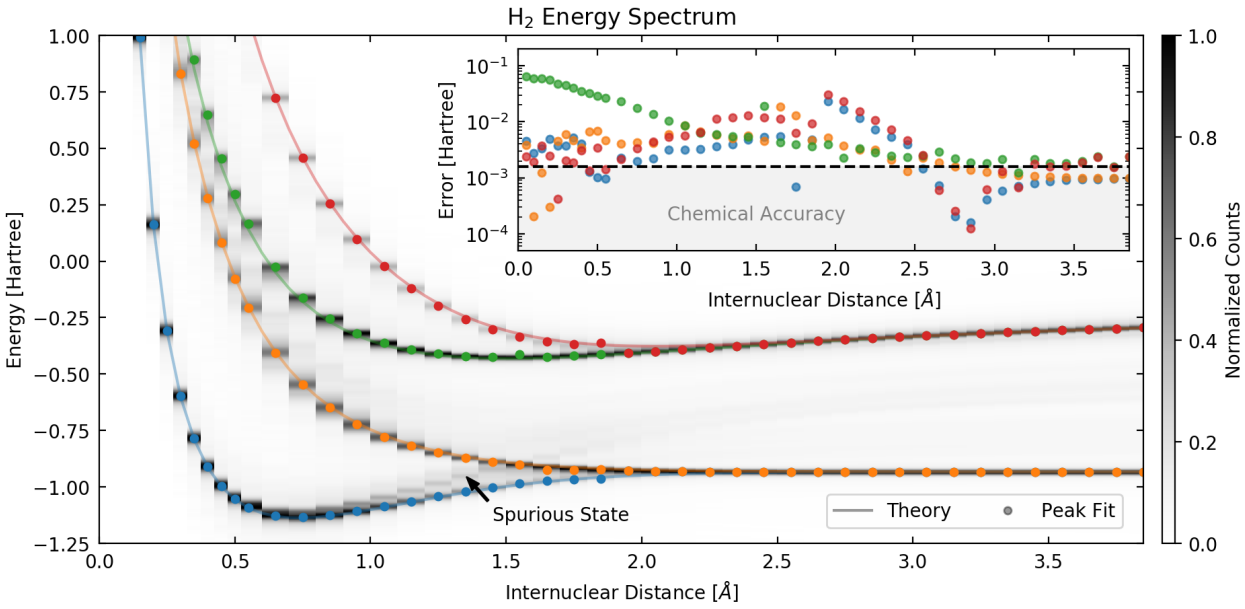

Figure 6.4: H_2 energy spectrum as a function of internuclear distance. Swarm particle energies for each bond length are histogrammed after application of a linear response expansion and Gaussian filter. Energy estimates obtained by a peak finding routine are indicated by dots with theoretically predicted energy levels shown as solid lines. An unphysical spurious state emerges at internuclear distances greater than ~ 1.2 Å due to uncorrected incoherent errors. Inset shows errors in the estimated ground and excited state energies as compared to chemical accuracy (1.6×10^{-3} Ha).

To derive excited states from this approximate ground state, we apply the linear-response QSE to each individually-reconstructed density matrix recovered during the minimization process. The results of applying this expansion are plotted in Fig. 6.3 where data are binned with 1.5 mHa resolution before convolution with a Gaussian filter (standard deviation of 7.5 mHa). Peak-finding routines are then used to estimate the mean energies for both the corrected ground and excited states. This shows improved robustness for small numbers of swarm iterations as it is less affected by outlying particles in the swarm yet to reach the global minimum.

Errors between experimentally predicted energies for the ground and excited states and their true values are plotted in the inset of Fig. 6.3. Chemical accuracy, the level required to make realistic chemical predictions, is achieved for the ground and highest excited state

across a wide range of internuclear distances. Estimates of the second and third excited state energies are generally within an order of magnitude of this level. It is interesting to note that although the ground electronic state wavefunction near equilibrium requires little entanglement to accurately represent, the same is not true of the excited states. The QSE is able to approximate these states with only additional local measurements and efficient classical computation, without an increase in required entanglement on the quantum state of the qubits.

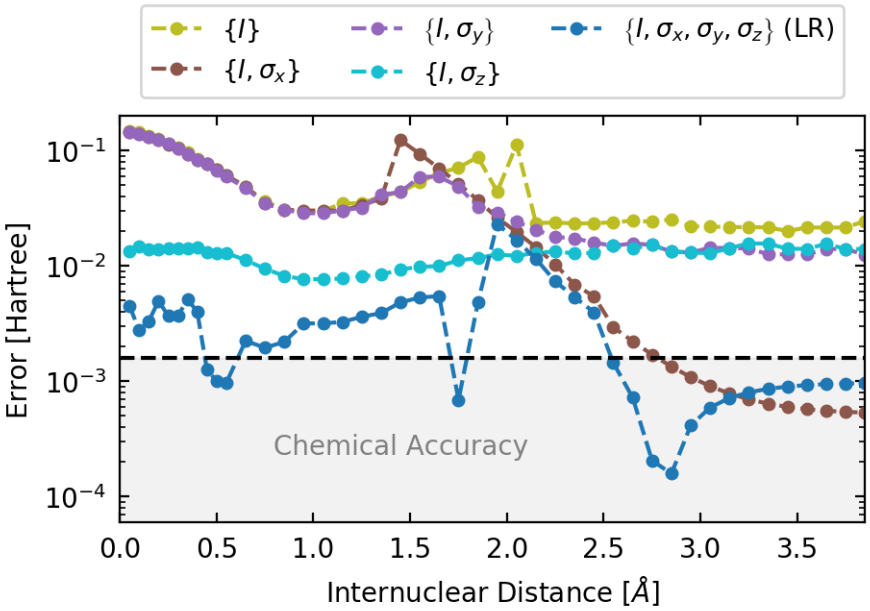

Figure 6.5: Comparison of errors in the ground-state energy estimate when applying the QSE protocol using various combinations of expansion operators. The linear response expansion (dark blue dots) provides an improvement of more than an order of magnitude over the bare VQE estimate (yellow dots) for the majority of internuclear distances computed.

Figure 6.3 shows the deviations from the theoretically expected values for the corrected ground-state energies when using different underlying measurement operators for the applied QSE. Those involving just a single Pauli operator offer sporadic improvement over the uncorrected case, with the σ_z operator achieving best results at smaller internuclear separations while the σ_x operator is most useful at larger ones. The complete linear-response expansion is able to mitigate incoherent errors for which that the bare VQE algorithm is unable to compensate and produces a reduction in the energy estimate error of almost two orders of magnitude over the entire range.

Note that ideally, the total number of extracted energy levels should be upper-bounded by the dimension of the Hamiltonian. However, if the extant error channels cause the prepared VQE ground state to be sufficiently mixed (for a given set of QSE operators), it is possible

to extract additional "spurious" energy levels. Such a spurious state is observed as indicated in Fig. 6.3 for internuclear distances between $\sim$ 1.2Å and $\sim$ 1.7Å. In some cases, these states may be discarded on the basis of continuity of the energy as a function of internuclear distance. Alternatively, these states can be removed by increasing the span of the QSE operators (at the cost of an increased tomographic measurement overhead). The exact conditions for the presence of a spurious state are currently being investigated theoretically.

QSE and Choice of Expansion Operators

The choice of operators which act on the ground-state density matrix to form the expanded subspace influences which excited states can be extracted. This we show in figure 6.3. Using only the identity and single Pauli operators (on each qubit) results in only a partial resolution of the low-lying excited states, while the full linear-response is able to resolve the entire spectrum.

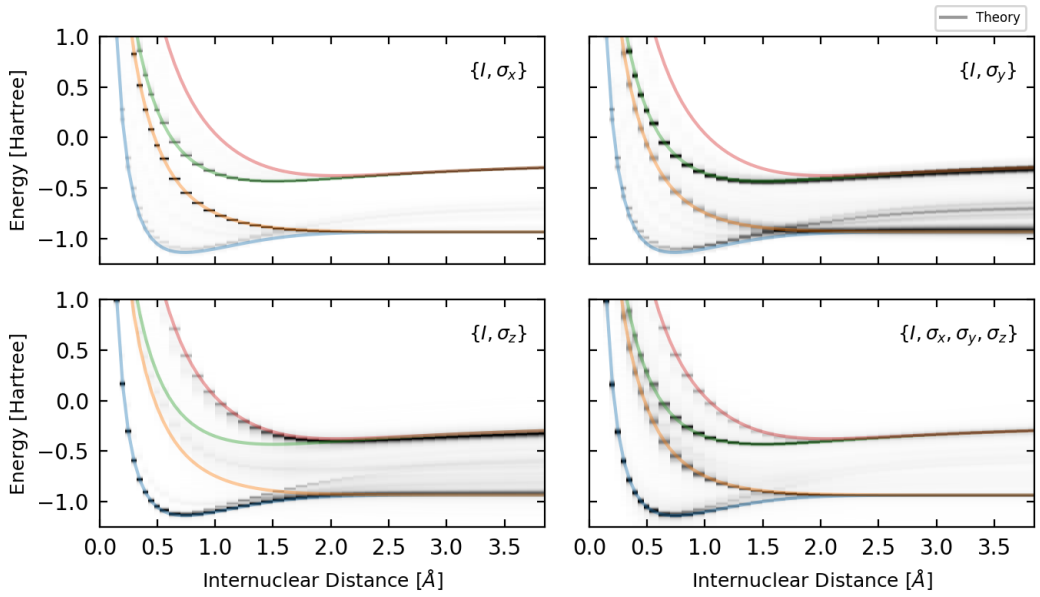

Figure 6.6: QSE protocol applied with different choices of measurement operators. Using only the identity and σ_y, σ_x, or σ_z results in errors in the calculated excited energies while using a full linear response expansion successfully resolves the entire spectrum.

QSE in the presence of errors

Having seen experimentally the performance of the quantum subspace expansion, we now pause to discuss theoretically some aspects of its performance in the presence of incoherent errors. The QSE works by resolving the action of an operator H within a subspace defined

by a set of operator $\{O_i\}$, such as the single fermion excitation operators S_1 or k^{th} order Pauli operators P_k defined earlier in the chapter. This is done by measuring the matrix elements coupling the states generated by these operators $H_{ij} = \langle\psi_0| O_i^\dagger H O_j |\psi_0\rangle$ as well as the corresponding identity operator in this space, also known as the overlap matrix, $S_{ij} = \langle\psi_0| O_i^\dagger O_j |\psi_0\rangle$. The action within this subspace is then used to provide increasingly accurate approximations (as a function of the subspace size) by solving the generalized eigenvalue problem $HC = SCE$ with the matrices H and S for the eigenvectors C and diagonal matrix of eigenvalues E.

Defining the density matrix for the pure state $|\psi_0\rangle$ as $\rho_0 = |\psi_0\rangle\langle\psi_0|$, it is easy to see these matrix elements are equivalent are equivalent to $H_{ij} = Tr[O_i^\dagger H O_j \rho_0]$ and $S_{ij} = Tr[O_i^\dagger O_j \rho_0]$. This formulation naturally generalizes to mixed states ρ with rank > 1, which are the case in essentially any real system with incoherent errors, and gives a clear prescription for the measurement of the matrix elements. However, in this notation it is less clear how the measurement correspond to action within a subspace and what this means in the case for mixed states ρ with rank > 1. To clarify these situations, we may alternatively use the vectorization of the density matrix to re-express these matrix elements.

We denote the row-major vectorization of a matrix ρ as $|\rho\rangle\rangle$. In this notation, we have that

$$\begin{aligned} H_{ij} &= Tr[O_i^\dagger H O_j \rho] && (6.10)\\ &= \langle\langle O_i | H O_j \rho\rangle\rangle && (6.11)\\ &= \langle\langle O_i | H \otimes \rho^T | O_j\rangle\rangle && (6.12)\\ S_{ij} &= \langle\langle O_i | I \otimes \rho^T | O_j\rangle\rangle. && (6.13) \end{aligned}$$

This construction clarifies a number of the mathematical properties, including the hermiticity of the matrices and their dimensionality. In the case of a pure state, the operator ρ^T has a single non-zero eigenvalue, and the maximum non-trivial dimension of the space, which is determined by the trace of the identity operator S using normalized operators $\{O_i\}$, is that of the Hamiltonian.

It is important to consider in more detail when the rank of ρ is > 1. In these cases, the dimension of the space is potentially greater than the dimension of the original Hamiltonian. The easiest way to see this is to consider the case of the maximally mixed state $\rho = \frac{1}{d} I$, where d is the dimension. In this case, the dimension determined by the identity is the square of that of the original Hamiltonian, which this construction makes clear is the maximal dimension of this problem. Moreover, by properties of the standard tensor product, it is easy to verify that the eigenvalues of $H \otimes I$ are the eigenvalues of H, but $d-$fold degenerate. We note that the factor of $1/d$ is treated by its appearance in the metric matrix S in the generalized eigenvalue problem.

Thus, if one measures a linearly independent, complete set of operators $\{O_i\}$ on the totally mixed state, the resulting eigenvalues will be the spectrum of H with $d-$fold degeneracies. These additional states represent the different possible expansions from components $|\psi_i\rangle\langle\psi_i|$ with $\rho = \sum_i |\psi_i\rangle\langle\psi_i|$ that allowed one to prepare the eigenstates using $\{O_i\}$.

Consider, however, if the resolution of the operator ρ is incomplete with the given measurements $\{O_i\}$, then one may have difficulty distinguishing the eigenstate approximations generated from different pure states. This leads to the so-called "spurious states" observed experimentally in this work, which are extra predicted eigenvalues that do not coincide with the eigenvalues of H.

To clarify these effects, consider the following Hamiltonian

$$H = \sigma_z^1 + \sigma_z^2 + \sigma_x^1 \sigma_x^2 \tag{6.14}$$

which has a ground state given by $\rho_0 = \alpha |00\rangle + \beta |11\rangle$. In the case of ρ_0, it is clear that the maximum dimension of this problem is 4 with any set of measurement.

Now considering the mixed state generated by a Pauli-X channel that occurs with probability $p \neq 0, 1$, $\rho = (1-p)\rho_0 + p\sigma_x^1 \rho_0 \sigma_x^1$. In this case, the operator ρ has as non-trivial eigenvalues p and $(1-p)$. As an example we choose $p = \frac{1}{2}$ such that it has a degenerate non-trivial spectrum of $\frac{1}{2}$ and $\frac{1}{2}$. In the case one measures a complete set of operators $\{O_i\}$, one then finds the eigenvalues of H with a degeneracy of 2 in each case. If we consider only the error in the estimate of the ground state energy, one finds that the operator set $\{I, \sigma_z^1 \sigma_z^2\}$ is sufficient to correct it exactly (if applied to the state resulting via acting with the error channel on the ideal ground state, i.e. without minimization on this value). The exact condition for the set of operators that correct errors in the ground state for a given H and error channel and their relation to traditional theories of quantum error correction is an open problem, currently the subject of ongoing research. We conjecture here based on numerical observations that conditions are related to the ability to construct operators within Span($\{O_i\}$) that both commute with H but not with the error channel E.

To study the case of spurious states, suppose one measures a set of operators with dimension greater than the dimension of the Hamiltonian but not sufficient to resolve ρ. In this case, one such set is $\{I, \sigma_x^1, \sigma_y^1, \sigma_x^2, \sigma_z^2, \sigma_x^1 \sigma_x^2, \sigma_x^1 \sigma_z^2, \sigma_y^1 \sigma_x^2, \sigma_y^1 \sigma_z^2\}$. If one measures the Hamiltonian and overlap on state ρ with this basis, one sees examples of the observed behaviors.

First, the non-trivial dimension of the problem is 7, which would be an experimental signature that the measured state is not a pure state but also not the totally mixed state. Second, the eigenspectrum contains the exact spectrum of H, but is not degenerate. Rather it contains 3 erroneous eigenvalues that correspond to the spurious states we define above. Thus the total spectrum is formed from a combination of an exact expansion from one state and a poor expansion from another. If one continues to add operators, the spurious values disappear, replaced by degeneracies in the spectrum on the exact values. It is interesting to note that if one chooses operators capable of correcting these errors, a smaller set such as $\{I, \sigma_x^1, \sigma_z^1, \sigma_z^2, \sigma_x^1 \sigma_z^2, \sigma_z^1 \sigma_z^2\}$ produces the exact spectrum with degeneracies only on the 2nd and 3rd eigenvalues with no spurious states.

VQE and coherent errors

The VQE is expected to have an intrinsic ability to correct for coherent gate errors (such as under or over rotations) due to the direct parameterization of the microwave pulse am-

plitudes/lengths and phases. As a signature of this ability, we plot in Fig. 6.3 the optimal parameters found by the VQE algorithm (for an internuclear distance of 1.55 $\mathring{A}$) and compare them to the parameters expected from our initial simulations. The amplitudes of the single-qubit rotations converge to nearly zero, as expected from simulations. The length of the bSWAP gate, which is finite so as to create entanglement between the two qubits, also agrees with simulation. However, the phase of the bSWAP drive differs significantly from the expected value, namely zero. To say this another way, at this internuclear separation, the theoretically-expected ground state wavefunction is a superposition of the states $|00\rangle$ and $|11\rangle$ with equal phases, yet the experimentally prepared ground state clearly exhibits a phase difference in the amplitudes of the $|00\rangle$ and $|11\rangle$ states. This discrepancy is likely due to an uncalibrated Stark shift during the bSWAP gate which is corrected for automatically by the classical minimization routine, which has no knowledge of the true bSWAP unitary transformation. Phases of the single qubit drives are not included on the figure, as the single qubit amplitudes have converged to zero, which renders the phase meaningless.

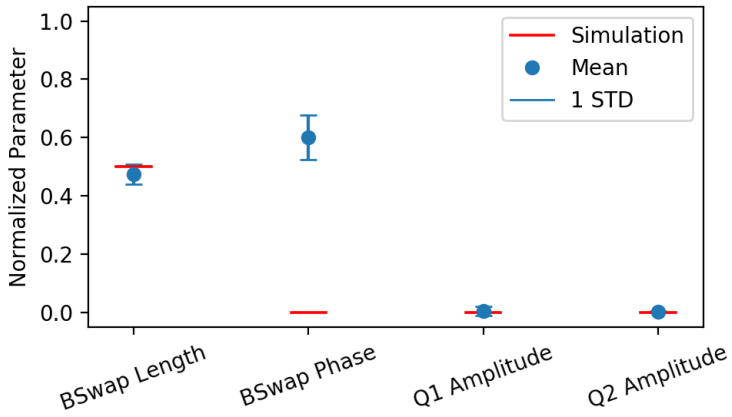

Figure 6.7: Final converged parameter values for 20 swarm particles at internuclear distance of 1.55 $\mathring{A}$ with results of a numerical simulation shown in red. Single qubit phases are not included as the amplitudes have converged to 0, rendering them arbitrary.

QSE beyond linear response

In this two-qubit example of the QSE, it is straightforward to go beyond the linear-response subspace and include additional measurement operators (see Fig. 6.8), as a demonstration that further error mitigation is possible. The dataset shown in the figure was taken in two separate runs: the first, for internuclear separations greater than 2.6 Angstroms, and the second for separations lower than that value. Technical reasons necessitated a restart of the data collection at that value. In this dataset, the bare VQE ground state error is more than an order of magnitude above the threshold for chemical accuracy. In the initial data run (for

internuclear separations greater than 2.6 Angstroms), the linear-response correction is able to bring this error down below the chemical-accuracy threshold. However, after the restart, the linear-response is no longer able to get below chemical accuracy. The likely reason for this is a drift in the gates which effected the tomographic reconstructions. But even though the linear response fails to fall below chemical accuracy, such accuracy can still be achieved over a large range of the separations by including additional operators in the QSE. In the figure, specifically, we show how the addition of the operator $\sigma_x^1\sigma_x^2$ dramatically improves the accuracy of the ground-state estimate.

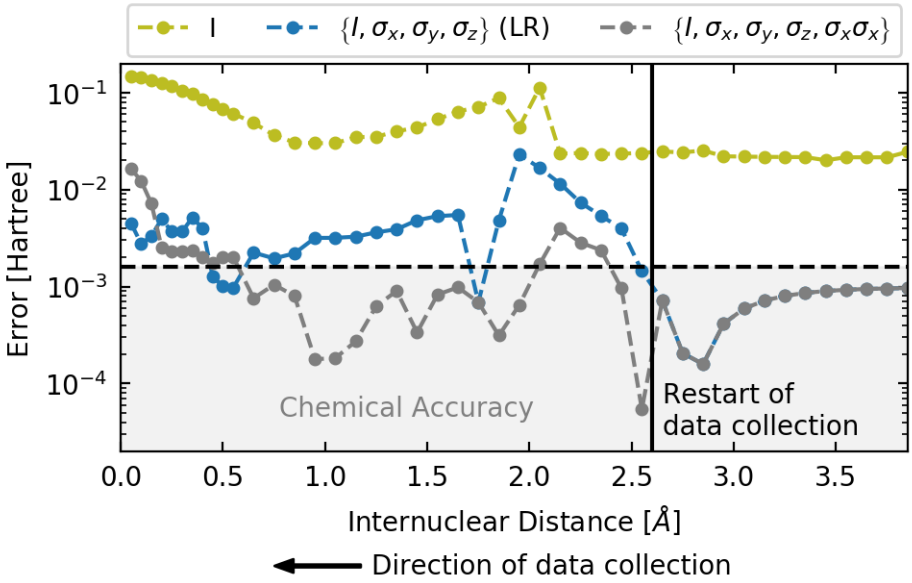

Figure 6.8: Starting from a large initial internuclear distance, the purely linear response expansion (blue) achieves chemical accuracy in the calculation of the ground state energy until a restart of the data collection run due to technical reasons (vertical black line). From this point onwards the accuracy in linear response estimate is degraded, most likely due to calibration errors in our tomographic reconstructions. Overcoming this calibration drift can be achieved by including additional two-qubit correlators such as $\sigma_x\sigma_x$ in the measurement span (gray).

6.4 Conclusion

In this chapter, we have described an extension of the variational quantum eigensolver that only uses a polynomial number of additional tomographic measurements to extract molecular excited states and mitigate incoherent errors on the ground state estimate. With the hydrogen molecule as a test case, we additionally confirm the intrinsic ability of the algorithm to correct for coherent gate errors when pulse properties are optimized directly. Used with

classical particle swarm minimization routines well suited to high-dimensional noisy environments, these techniques yield ground- and excited-state energy estimates with near-chemical accuracy. Our results highlight the potential of QSE to significantly reduce the need for more advanced error correction techniques, thereby facilitating practical applications of near-term quantum hardware.

Chapter 7

Future directions

As the reader has hopefully taken away from the past several chapters, though the challenges associated with understanding and controlling even small-scale quantum systems are immense, rapid progress is being made towards this goal. In this thesis, we have developed a few new capabilities for manipulating quantum systems, and many small extensions of these tools can be readily imagined. Most of these involve building larger systems of transmons and cavities. For example, one can build up progressively larger Bose-Hubbard chains of transmons, either with linear connectivity or expanding into two or three dimensions, and explore the preparation and stabilization of interesting many-body states. Since the attractive regime of the Bose-Hubbard phase diagram is difficult for ultracold atoms to access, this could be a good niche for superconducting systems. To aid in measuring the state of the system, one could equip each transmon in the system with its own dedicated readout resonator. Similar extensions of the topological quantum walk (say, to multiple dimensions) or the variational quantum eigensolver (to increasingly large molecules) are also possible.

As quantum hardware continues to scale up—either in extensions to the experiments described here, or towards a useful quantum computer—it will likely be extremely important to develop a precise understanding of the errors which plague these devices. Such an understanding is currently lacking in the field of superconducting qubits: for example, current state-of-the-art methods for characterizing the quality of gates in a quantum system (including randomized benchmarking and quantum process tomography) overestimate the performance of small quantum devices in executing real multi-qubit algorithms. In fact, thus far no group has demonstrated a predictive error model on a quantum processor comprising even modest numbers of qubits. As major theoretical and experimental efforts are currently aimed at determining whether noisy quantum processors with tens of qubits can run useful algorithms, this lack of predictive error models is a major impediment to progress. Validated error models would also provide guidance in choosing and designing error-correction schemes en route to fully fault-tolerant quantum computers.

Though this problem will likely prove incredibly challenging, it is also very important. A couple angles of attack to devise an error model readily suggest themselves. The first involves handling known error mechanisms. For example, in an architecture which is now common,

with static couplings between nearest-neighbor qubits, it is known that an unwanted entangling interaction occurs during idling. During gates, microwave crosstalk causes spurious dynamics on spectator qubits. As these mechanisms can be precisely characterized, the problem reduces to efficiently incorporating them into numerical or analytical models of the multi-qubit devices. A second avenue of attack is the development of techniques for measuring hitherto-inaccessible parameters of the processors Hamiltonian; an example is the coupling rate between qubits and neighboring resonators which enable entangling gates. Once measured, the knowledge of these parameters can be used to construct more accurate models of the dynamics induced by the gates themselves.

A more speculative approach, but one that might be necessary for moving beyond eight qubits, is the use of model-order reduction techniques, potentially incorporating modern developments in machine-learning. Even in the best-case scenario in which one can accurately measure the full Hamiltonian and error channels of a fifty- to one-hundred-qubit chip, numerically integrating the corresponding equations of motion will likely prove intractable for gate depths of interest. Model-order reduction techniques, developed in the past few decades, have found success in managing this complexity in fields ranging from circuit analysis to fluid dynamics. These techniques aim to determine low-dimensional models of system dynamics which are both easy to integrate and capture the relevant features. Applying these techniques to a multi-qubit chip might yield tractable, predictive error models.

Bibliography

[1] M. Dalmonte, S.I. Mirzai, P.R. Muppalla, D. Marcos, P. Zoller, G. Kirchmair, arXiv:1501.03098.

[2] Y. Aharonov, L. Davidovich, and N. Zagury. "Quantum random walks". In: *Physical Review A* 48.2 (1993), pp. 1687–1690. ISSN: 1050-2947. DOI: 10.1103/PhysRevA.48.1687.

[3] Monika Aidelsburger et al. "Measuring the Chern number of Hofstadter bands with ultracold bosonic atoms". In: *Nature Physics* 11.2 (2015), pp. 162–166.

[4] Andris Ambainis. "Quantum Walk Algorithm for Element Distinctness". In: *SIAM Journal on Computing* 37.1 (2004), pp. 210–239.

[5] János K. Asbóth and Hideaki Obuse. "Bulk-boundary correspondence for chiral symmetric quantum walks". In: *Phys. Rev. B* 88 (12 Sept. 2013), p. 121406. DOI: 10.1103/PhysRevB.88.121406. URL: https://link.aps.org/doi/10.1103/PhysRevB.88.121406.

[6] Marcos Atala et al. "Direct measurement of the Zak phase in topological Bloch bands". In: *Nature Physics* 9.12 (2013), pp. 795–800. ISSN: 1745-2473. DOI: 10.1038/nphys2790. eprint: 1212.0572. URL: http://dx.doi.org/10.1038/nphys2790.

[7] W. S. Bakr et al. "Probing the Superfluid–to–Mott Insulator Transition at the Single-Atom Level". In: *Science* 329.5991 (2010), pp. 547–550. ISSN: 0036-8075. DOI: 10.1126/science.1192368. eprint: https://science.sciencemag.org/content/329/5991/547.full.pdf. URL: https://science.sciencemag.org/content/329/5991/547.

[8] M. C. Bañuls et al. "Quantum walk with a time-dependent coin". In: *Physical Review A - Atomic, Molecular, and Optical Physics* 73.6 (2006). ISSN: 10502947. DOI: 10.1103/PhysRevA.73.062304. eprint: 0510046 (quant-ph).

[9] M. C. Bafffdfffduls et al. "Quantum walk with a time-dependent coin". In: *Phys. Rev. A* 73.6 (June 2006), p. 062304. DOI: 10.1103/PhysRevA.73.062304. URL: http://link.aps.org/doi/10.1103/PhysRevA.73.062304 (visited on 03/09/2016).

[10] J. Bourassa et al. "Josephson-junction-embedded transmission-line resonators: From Kerr medium to in-line transmon". In: *Phys. Rev. A* 86 (1 July 2012), p. 013814. DOI: 10.1103/PhysRevA.86.013814. URL: https://link.aps.org/doi/10.1103/PhysRevA.86.013814.

[11] Sergey Bravyi et al. *Tapering off qubits to simulate fermionic Hamiltonians*. 2017. eprint: arXiv:1701.08213.

[12] C. Cedzich et al. "Propagation of Quantum Walks in Electric Fields". In: *Phys. Rev. Lett.* 111.16 (Oct. 2013), p. 160601. DOI: 10.1103/PhysRevLett.111.160601. URL: http://link.aps.org/doi/10.1103/PhysRevLett.111.160601 (visited on 03/09/2016).

[13] C. Cedzich et al. "Propagation of Quantum Walks in Electric Fields". In: *Phys. Rev. Lett.* 111 (16 Oct. 2013), p. 160601. DOI: 10.1103/PhysRevLett.111.160601. URL: http://link.aps.org/doi/10.1103/PhysRevLett.111.160601.

[14] Zijun Chen et al. "Measuring and Suppressing Quantum State Leakage in a Superconducting Qubit". In: *Phys. Rev. Lett.* 116 (2 Jan. 2016), p. 020501. DOI: 10.1103/PhysRevLett.116.020501. URL: https://link.aps.org/doi/10.1103/PhysRevLett.116.020501.

[15] Andrew M. Childs. "Universal computation by quantum walk". In: *Physical Review Letters* 102.18 (2009), pp. 1–4. ISSN: 00319007. DOI: 10.1103/PhysRevLett.102.180501. eprint: 0806.1972.

[16] J. M. Chow et al. "Detecting highly entangled states with a joint qubit readout". In: *Phys. Rev. A* 81 (6 June 2010), p. 062325. DOI: 10.1103/PhysRevA.81.062325. URL: https://link.aps.org/doi/10.1103/PhysRevA.81.062325.

[17] A. A. Clerk et al. "Introduction to quantum noise, measurement, and amplification". In: *Rev. Mod. Phys.* 82 (2 Apr. 2010), pp. 1155–1208. DOI: 10.1103/RevModPhys.82.1155.

[18] Edward Farhi and Sam Gutmann. "Quantum computation and decision trees". In: *Physical Review A* 58.2 (1998), pp. 915–928. ISSN: 1050-2947.

[19] Jay Gambetta et al. "Protocols for optimal readout of qubits using a continuous quantum nondemolition measurement". In: *Phys. Rev. A* 76 (1 2007), p. 012325.

[20] Jay Gambetta et al. "Qubit-photon interactions in a cavity: Measurement-induced dephasing and number splitting". In: *Phys. Rev. A* 74 (4 Oct. 2006), p. 042318. DOI: 10.1103/PhysRevA.74.042318. URL: https://urldefense.proofpoint.com/v2/url?u=http-3A__link.aps.org_doi_10.1103_PhysRevA.74.042318&d=AwIGaQ&c=-dg2m7zWuuDZ0MUcV7Sdqw&r=9wWzktyFzfKGkAHTkVS1SGOlagLfy_I8Sm7HN1M4QZ8&m=Lecg7KtLL5dGFA_G29-0xBg9qjnyRXdFKsFfP9alxJs&s=CaUcLcLfv6YIGISvRVdMyWWa73BHW4r5aZqfTk&e=.

[21] Maximilian Genske et al. "Electric quantum walks with individual atoms". In: *Physical Review Letters* 110.19 (2013), pp. 1–5. ISSN: 00319007. DOI: 10.1103/PhysRevLett.110.190601. arXiv: 1302.2094.

[22] Markus Greiner et al. "Quantum phase transition from a superfluid to a Mott insulator in a gas of ultracold atoms". In: *Nature* 415 (Jan. 2002). Article, URL: https://doi.org/10.1038/415039a.

[23] M Zahid Hasan and Charles L Kane. "Colloquium: topological insulators". In: *Reviews of Modern Physics* 82.4 (2010), p. 3045.

[24] M. Hatridge et al. "Dispersive magnetometry with a quantum limited SQUID parametric amplifier". In: *Physical Review B* 83.13 (Apr. 2011), p. 134501. ISSN: 1098-0121. DOI: 10.1103/PhysRevB.83.134501. URL: http://link.aps.org/doi/10.1103/PhysRevB.83.134501.

[25] W. J. Hehre, R. Ditchfield, and J. A. Pople. "SelffffdfffdfffdConsistent Molecular Orbital Methods. XII. Further Extensions of GaussianfffdfffdfffdType Basis Sets for Use in Molecular Orbital Studies of Organic Molecules". In: *The Journal of Chemical Physics* 56.5 (1972), pp. 2257–2261. DOI: 10.1063/1.1677527. eprint: https://doi.org/10.1063/1.1677527. URL: https://doi.org/10.1063/1.1677527.

[26] Kurt Jacobs. *Quantum Measurement Theory and its Applications*. Cambridge University Press, 2014. DOI: 10.1017/CBO9781139179027.

[27] J. E. Johnson et al. "Heralded State Preparation in a Superconducting Qubit". In: *Phys. Rev. Lett.* 109 (5 Aug. 2012), p. 050506. DOI: 10.1103/PhysRevLett.109.050506. URL: https://link.aps.org/doi/10.1103/PhysRevLett.109.050506.

[28] Julia Kempe. "Quantum random walks: an introductory overview". In: *Contemporary Physics* 44.4 (2003), pp. 307–327.

[29] Gerhard Kirchmair et al. "Observation of quantum state collapse and revival due to the single-photon Kerr effect". In: *Nature* 495.7440 (2013), pp. 205–209.

[30] Alexei Kitaev. "Periodic table for topological insulators and superconductors". In: *arXiv preprint arXiv:0901.2686* (2009).

[31] Takuya Kitagawa et al. "Exploring topological phases with quantum walks". In: *Phys. Rev. A* 82.3 (Sept. 2010), p. 033429. DOI: 10.1103/PhysRevA.82.033429. URL: http://link.aps.org/doi/10.1103/PhysRevA.82.033429 (visited on 03/07/2016).

[32] Takuya Kitagawa et al. "Observation of topologically protected bound states in photonic quantum walks". In: *Nature communications* 3 (2012), p. 882.

[33] Jens Koch et al. "Charge-insensitive qubit design derived from the Cooper pair box". In: *Phys. Rev. A* 76 (4 Oct. 2007), p. 042319. DOI: 10.1103/PhysRevA.76.042319. URL: https://link.aps.org/doi/10.1103/PhysRevA.76.042319.

[34] Jens Koch et al. "Charge-insensitive qubit design derived from the Cooper pair box". In: *Physical Review A - Atomic, Molecular, and Optical Physics* 76.4 (2007), pp. 1–19. ISSN: 10502947. DOI: 10.1103/PhysRevA.76.042319.

[35] C. Macklin et al. "A near–quantum-limited Josephson traveling-wave parametric amplifier". In: *Science* 350.6258 (2015), pp. 307–310. ISSN: 0036-8075. DOI: 10.1126/science.aaa8525. eprint: https://science.sciencemag.org/content/350/6258/307.full.pdf. URL: https://science.sciencemag.org/content/350/6258/307.

[36] J. Majer et al. "Coupling superconducting qubits via a cavity bus". In: *Nature* 449.7161 (Sept. 2007), pp. 443–447.

[37] Vladimir E. Manucharyan et al. "Fluxonium: Single Cooper-Pair Circuit Free of Charge Offsets". In: *Science* 326.5949 (2009), pp. 113–116. ISSN: 0036-8075. DOI: 10.1126/science.1175552. eprint: https://science.sciencemag.org/content/326/5949/113.full.pdf. URL: https://science.sciencemag.org/content/326/5949/113.

[38] Robert Matjeschk et al. "Quantum Walks with Nonorthogonal Position States". In: *Physical review letters* 109.24 (2012), p. 240503.

[39] Jarrod R. McClean et al. "Hybrid quantum-classical hierarchy for mitigation of decoherence and determination of excited states". In: *Phys. Rev. A* 95 (4 Apr. 2017), p. 042308. DOI: 10.1103/PhysRevA.95.042308. URL: https://link.aps.org/doi/10.1103/PhysRevA.95.042308.

[40] Joel E Moore. "The birth of topological insulators". In: *Nature* 464.7286 (2010), pp. 194–198.

[41] Joel E. Moore, Ying Ran, and Xiao-Gang Wen. "Topological surface states in three-dimensional magnetic insulators". In: *Phys. Rev. Lett.* 101.October (2008), pp. 1–4. ISSN: 00319007. DOI: 10.1103/PhysRevLett.101.186805. eprint: 0804.4527.

[42] F. Motzoi et al. "Simple Pulses for Elimination of Leakage in Weakly Nonlinear Qubits". In: *Phys. Rev. Lett.* 103 (11 Sept. 2009), p. 110501. DOI: 10.1103/PhysRevLett.103.110501. URL: https://link.aps.org/doi/10.1103/PhysRevLett.103.110501.

[43] Simon E. Nigg et al. "Black-Box Superconducting Circuit Quantization". In: *Phys. Rev. Lett.* 108 (24 June 2012), p. 240502. DOI: 10.1103/PhysRevLett.108.240502. URL: https://link.aps.org/doi/10.1103/PhysRevLett.108.240502.

[44] Kevin O'Brien et al. "Resonant Phase Matching of Josephson Junction Traveling Wave Parametric Amplifiers". In: *Phys. Rev. Lett.* 113 (15 Oct. 2014), p. 157001. DOI: 10.1103/PhysRevLett.113.157001. URL: https://link.aps.org/doi/10.1103/PhysRevLett.113.157001.

[45] P. J. J. O'Malley et al. "Scalable Quantum Simulation of Molecular Energies". In: *Phys. Rev. X* 6 (3 July 2016), p. 031007. DOI: 10.1103/PhysRevX.6.031007. URL: https://link.aps.org/doi/10.1103/PhysRevX.6.031007.

[46] J.-L. Orgiazzi et al. "Flux qubits in a planar circuit quantum electrodynamics architecture: Quantum control and decoherence". In: *Phys. Rev. B* 93 (10 Mar. 2016), p. 104518. DOI: 10.1103/PhysRevB.93.104518. URL: https://link.aps.org/doi/10.1103/PhysRevB.93.104518.

[47] Hanhee Paik et al. "Observation of High Coherence in Josephson Junction Qubits Measured in a Three-Dimensional Circuit QED Architecture". In: *Physical Review Letters* 107.24 (Dec. 2011), p. 240501. ISSN: 0031-9007. DOI: 10.1103/PhysRevLett.107.240501. URL: http://link.aps.org/doi/10.1103/PhysRevLett.107.240501.

[48] K.E. Parsopoulos and M.N. Vrahatis. "Recent approaches to global optimization problems through Particle Swarm Optimization". In: *Natural Computing* 1.2 (June 2002), pp. 235–306. ISSN: 1572-9796. DOI: 10.1023/A:1016568309421. URL: https://doi.org/10.1023/A:1016568309421.

[49] Michael J. Peterer et al. "Coherence and Decay of Higher Energy Levels of a Superconducting Transmon Qubit". In: *Phys. Rev. Lett.* 114 (1 Jan. 2015), p. 010501. DOI: 10.1103/PhysRevLett.114.010501. URL: https://urldefense.proofpoint.com/v2/url?u=http-3A__link.aps.org_doi_10.1103_PhysRevLett.114.010501&d=AwIGaQ&c=-dg2m7zWuuDZ0MUcV7Sdqw&r=9wWzktyFzfKGkAHTkVS1SGOlagLfy_I8Sm7HN1M4QZ8&m=Lecg7KtLL5dGFA_G29-0xBg9qjnyRXdFKsFfP9alxJs&s=M5UchmzSYeyViyxpd7j4LwtjSa2jp2HIF0ce=.

[50] S. Poletto et al. "Entanglement of Two Superconducting Qubits in a Waveguide Cavity via Monochromatic Two-Photon Excitation". In: *Phys. Rev. Lett.* 109 (24 Dec. 2012), p. 240505. DOI: 10.1103/PhysRevLett.109.240505. URL: https://link.aps.org/doi/10.1103/PhysRevLett.109.240505.

[51] P. M. Preiss et al. "Strongly correlated quantum walks in optical lattices". In: *Science* 347.6227 (2015), pp. 1229–1233. ISSN: 0036-8075. DOI: 10.1126/science.1260364. eprint: 1409.3100. URL: http://www.sciencemag.org/content/347/6227/1229.abstract.

[52] JM Raimond and S Haroche. "Exploring the Quantum". In: *Oxford University Press* 82.1 (2006), p. 86. ISSN: 00029505. DOI: 10.1119/1.4827830. URL: http://link.aip.org/link/AJPIAS/v82/i1/p86/s1%7B%5C&%7DAgg=doi%20http://scitation.aip.org/content/aapt/journal/ajp/82/1/10.1119/1.4827830%20http://tocs.ulb.tu-darmstadt.de/180865897.pdf.

[53] Pedram Roushan et al. "Observation of topological transitions in interacting quantum circuits". In: *Nature* 515.7526 (2014), pp. 241–244.

[54] Andreas P Schnyder et al. "Classification of topological insulators and superconductors in three spatial dimensions". In: *Physical Review B* 78.19 (2008), p. 195125.

[55] A. Schreiber et al. "A 2D Quantum Walk Simulation of Two-Particle Dynamics". In: *Science* 336.2012 (2012), pp. 55–58. ISSN: 0036-8075.

[56] D. I. Schuster et al. "Resolving photon number states in a superconducting circuit". In: *Nature* 445.7127 (Feb. 2007), pp. 515–518. ISSN: 0028-0836. DOI: 10.1038/nature05461. URL: http://dx.doi.org/10.1038/nature05461.

[57] D. H. Slichter. "Quantum Jumps and Measurement Backaction in a Superconducting Qubit". In: 2011.

[58] M. Stern et al. "Flux Qubits with Long Coherence Times for Hybrid Quantum Circuits". In: *Phys. Rev. Lett.* 113 (12 Sept. 2014), p. 123601. DOI: 10.1103/PhysRevLett.113.123601. URL: https://link.aps.org/doi/10.1103/PhysRevLett.113.123601.

[59] B. C. Travaglione and G. J. Milburn. "Implementing the quantum random walk". In: *Phys. Rev. A* 65 (3 Feb. 2002), p. 032310. DOI: 10.1103/PhysRevA.65.032310. URL: https://link.aps.org/doi/10.1103/PhysRevA.65.032310.

[60] Oliver Viehmann, Jan von Delft, and Florian Marquardt. "Observing the Nonequilibrium Dynamics of the Quantum Transverse-Field Ising Chain in Circuit QED". In: *Phys. Rev. Lett.* 110 (3 Jan. 2013), p. 030601. DOI: 10.1103/PhysRevLett.110.030601. URL: https://urldefense.proofpoint.com/v2/url?u=http-3A__link.aps.org_doi_10.1103_PhysRevLett.110.030601&d=AwIGaQ&c=-dg2m7zWuuDZ0MUcV7Sdqw&r=9wWzktyFzfKGkAHTkVS1SGOlagLfy_I8Sm7HN1M4QZ8&m=Lecg7KtLL5dGFA_G29-0xBg9qjnyRXdFKsFfP9alxJs&s=qG_SiTLNKRTtdJzKPKikGkU--1V_NFm1ptMY2HgoX1A&e=.

[61] Brian Vlastakis et al. "Deterministically Encoding Quantum Information Using 100-Photon Schrfffdfffddinger Cat States". en. In: *Science* 342.6158 (Nov. 2013), pp. 607–610. ISSN: 0036-8075, 1095-9203. DOI: 10.1126/science.1243289. URL: http://science.sciencemag.org/content/342/6158/607 (visited on 03/09/2016).

[62] Brian Vlastakis et al. "Deterministically encoding quantum information using 100-photon Schrödinger cat states." In: *Science (New York, N.Y.)* 342.6158 (Nov. 2013), pp. 607–10. ISSN: 1095-9203. DOI: 10.1126/science.1243289. URL: http://www.ncbi.nlm.nih.gov/pubmed/24072821.

[63] A. Wallraff et al. "Strong coupling of a single photon to a superconducting qubit using circuit quantum electrodynamics". In: *Nature* 431.7005 (2004), pp. 162–167. ISSN: 1476-4687. DOI: 10.1038/nature02851. URL: https://doi.org/10.1038/nature02851.

[64] Peng Xue et al. "Quantum walks on circles in phase space via superconducting circuit quantum electrodynamics". In: *Phys. Rev. A* 78 (4 Oct. 2008), p. 042334. DOI: 10.1103/PhysRevA.78.042334. URL: http://link.aps.org/doi/10.1103/PhysRevA.78.042334.

[65] Peng Xue et al. "Quantum walks on circles in phase space via superconducting circuit quantum electrodynamics". In: *Physical Review A* 78.4 (2008), p. 042334.

[66] Fei Yan et al. "The flux qubit revisited to enhance coherence and reproducibility". In: *Nature Communications* 7 (Nov. 2016). Article, URL: https://doi.org/10.1038/ncomms12964.

[67] J. Zak. "Berrys phase for energy bands in solids". In: *Physical Review Letters* 62.23 (1989), pp. 2747–2750. ISSN: 00319007. DOI: 10.1103/PhysRevLett.62.2747. URL: http://dx.doi.org/10.1103/PhysRevLett.62.2747.